Alma Mater Studiorum – Università di Bologna

Dottorato di Ricerca in Ingegneria
Elettronica, Informatica e delle Telecomunicazioni
Ciclo XXIII

SSD: ING-INF/01

MODELING, DESIGN AND EXPERIMENTAL CHARACTERIZATION OF MICRO-ELECTRO-MECHANICAL SYSTEMS FOR GAS-CHROMATOGRAPHIC APPLICATIONS

Presentata da: **ENRICO COZZANI**

Coordinatore Dottorato

Chiar.ma Prof.ssa PAOLA MELLO

Relatore

Chiar.mo Prof. GUIDO MASETTI

Esame finale anno 2011

A Maria e Luciano

CONTENTS

CHAPTER 1

INTRODUCTION

1.1 – MOTIVATIONS.

Chromatography is a powerful and commonly used analytical technique, based on the principle of the separation of sample components due to their different distribution between two phases, one stationary (a solid, or a liquid supported on a solid) and the other mobile (also called carrier).

Depending on the typology of the mobile phase, we can distinguish between liquid-chromatography (LC) and gas-chromatography (GC): on the latter technique we will focus our attention in this work.

Undoubtedly, one of the great advantages of gas-chromatographic technique stands in its versatility: this methodology, in fact, can be applied to the solution of many problems in various fields, e.g.

- *Drugs and Pharmaceuticals*: GC is used in the quality control of products and also in the analysis of new products and the monitoring of metabolites in biological systems [1].
- *Clinical Chemistry*: GC is adaptable to such samples as breath, blood, urine and other biological fluids [2].
- *Foods*: The determination of antioxidants and food preservatives is an active part of gas chromatographic field, and the sample types are almost limitless: wines, fish, cheeses, oils, food aromas and so on [3].
- *Environmental Studies*: Nowadays, a rapidly increasing interest towards air quality monitoring in general and pollutants analysis in particular can be observed, especially for its consequences on human healthcare and safety. It is

well known, in fact, that the presence of certain compounds mixed with the air that we breathe, even if at very small concentrations (parts per billion or lower), may have extremely dangerous implications on our health and cause chronic respiratory diseases like asthma, emphysema, bronchitis and even cancer. Air samples can be very complex mixtures, and GC is easily adapted to the separation and analysis of such mixtures [4, 5].

For all these reasons, the knowledge and the control of techniques able to provide both quantitative and qualitative analysis are of great relevance: in particular, the focus of this thesis will be addressed to the field of environmental studies and specifically to the development of miniaturized systems for air quality monitoring.

1.2 – PECULIARITIES OF A GC SYSTEM.

Fig. 1.1 shows the schematic of a GC system for environmental monitoring, whose core components are [6]:

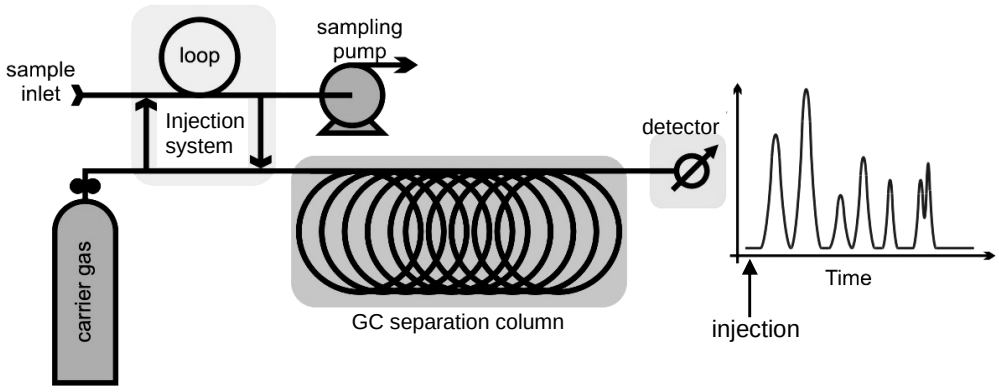

Fig. 1.1 – Schematic representation of a GC system

- the **injection system** which supplies the sample to
- the **GC separation column**, which temporally and spatially separates the single compounds of the mixture (during its transport through the column by the flow of a carrier gas) on the basis of their affinity with the stationary phase distributed all along the column length, finally reaching

- the **detector**, which acquires the signals provided by the separated components at the column outlet.

The result of the analysis is a chromatogram, i.e. a series of peaks separated in time (as shown in the previous figure).
The amount of time elapsed from the injection of the sample to the recording of the peak maximum of the component is defined as the retention time (x-axis of the chromatogram).
Obviously, the lower the retention time, the lower the affinity of the component with the stationary phase: for this reason, by evaluating the position of the peak maximum on the abscissa, the specific compound can be identified (qualitative analysis).
The physical quantity on the y-axis of the chromatogram depends on the operation's principle of the detector employed in the GC system: by properly evaluating the output signal (generally the height or the area of the peak) we can measure the amount of the component and have a correlation with its concentration (quantitative analysis).
The main features that a GC system must satisfy can be summarized in the following list:

- *Resolution*. Referred to the GC column, it represents the capability to separate and distinguish molecules that are physically and chemically similar.
- *Sensitivity*. Referred to the detector, it represents the capability to measure extremely low amounts of solute (typically parts per billion of solute).
- *Analysis time*. The separation and the detection of the components in a sample should not take a very long time (tens of minutes or less).
- *Selectivity.* The capability to detect the analytes of interest (often at very low concentrations) despite the presence of interfering elements (often at high concentrations) in the sample mixture.

Common laboratory GC systems allow to perform off-line analysis of specific sample mixtures eluted in a stationary phase (carrier gas) taken from an apposite cylinder (as shown in Fig. 1), and to obtain excellent results from the point of view of resolution, sensitivity and selectivity.

Unfortunately, these systems present a certain number of drawbacks that can not be circumvented, especially when the interest shifts from off-line to on-line analysis.
On-site analysis, in fact, is becoming increasingly important, especially in the area of environmental monitoring, since it reduces the risk of contamination, sample loss, and sample decomposition during transport.
To be effective, an on-site analytical instrument should be small, lightweight and low-maintenance while, on the contrary, common GC systems are bulky, expensive and able to perform analyses with high flexibility and low throughput of only few points per hour; moreover, in-field analysis by means of conventional GC-systems is obstructed also from the bulk caused by the gas carrier cylinder and by the calibration cylinder.

1.3 – TOWARDS A MICROFABRICATED GC SYSTEM.

As already mentioned, current GC systems are still low in performances for in- field use where complex mixtures analysis and fast responses are required.
On the contrary, the use of Micro-Electro-Mechanical-Systems (MEMS) technology for GC-based micro-systems promises smaller sizes, lower power consumptions, faster analyses, lower costs and greatly increased portability for in-field use.
Moreover, the overall functionality of GC systems is likely to improve when sensors, valves, pumps, columns and other components are replaced with their lower-cost, lower-volume, lower-power micro-fabricated counterparts.
In the last two decades, the development and the exploitation of silicon micromachining techniques and micrometric level fabrication processes became an important feature in the achievement of micro-systems to be employed in GC systems with reduced dimensions [7, 8, 9].
In the following pictures, examples of an injector (Fig. 2-a), a separation column (Fig. 2-b) and a detector (namely a Thermal Conductivity Detector, Fig. 2-c) obtained through silicon micromachining techniques are shown:

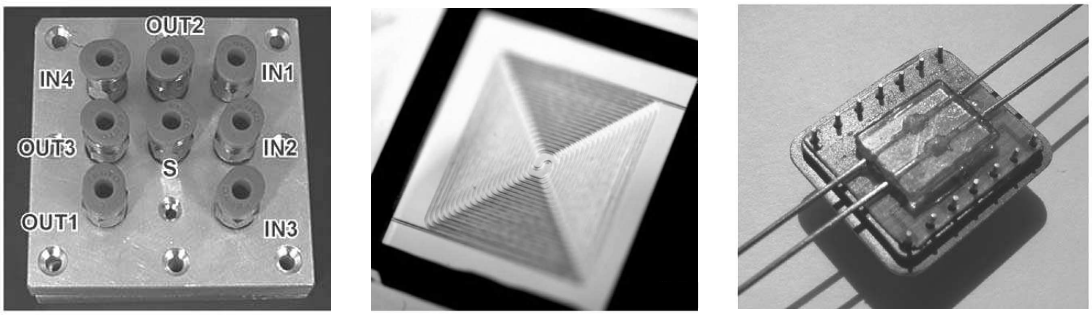

(a) *(b)* *(c)*

Fig. 1.2 – Examples of micro-fabricated components of a GC system: injection system [7] (a), separation column [10] (b) and thermal conductivity detector [7] (c).

1.4 – RESEARCH ACTIVITY AT IMM-BOLOGNA SECTION

Since several years, the Institute for Microelectronics and Microsystems (IMM) - Section of Bologna is involved in an intense research activity focused on the development of micro-systems for air quality monitoring [11, 12].

In particular, a great interest is addressed towards the analysis of Volatile Organic Compounds (VOC), like for example benzene, because of their strong toxicity even at extremely low concentrations (as a matter of fact, risk threshold for benzene is in the order of parts per billion).

The final target of this activity is the fabrication and the assembly of the three components (injection system, separation column and detector) aimed at obtaining a totally micro-fabricated GC-system.

In this scenario, the knowledge and the mastery of Micro-Electro-Mechanical-Systems (MEMS) fabrication techniques can be exploited and provide a great contribution for the design of innovative micro-systems to be employed in the micro-GC module.

In the subsequent chapters of this thesis, design procedures, electro-thermal-fluidic simulations and experimental characterizations of micro-electro-mechanical-systems (namely different typologies of GC micro-columns and micro-detectors) suited for gas-chromatographic applications will be presented, together with the principal steps of the technological processes employed for devices fabrication.

REFERENCES

[1] Grametbauer P., Kartusek S., Hausuer O.: "Diagnosis of aerobic gram negative bacteria by the detection of volatile metabolites using gas-chromatography", *Ceskoslov. Epidemiol. Microbiol. Immunol.*, volume 37, pp. 216-223 (1988).

[2] Phillips M.: "Method for the collection and assay of volatile organic compounds in breath", *Anal. Biochem.*, volume 247, pp. 272-278 (1997).

[3] Saka M.: "Application of gas chromatograph with selected detector for pesticide residue analysis in food", *Journal of Pesticide Science*, volume 35, issue 4, pp. 580 – 586 (2010).

[4] Wang Z.D., Fingas M.: **"**Fate and identification of spilled oils and petroleum products in the environment by GC-MS and GC-FID", *Energy Sources*, volume 25, issue 6, pp. 491 – 508 (2003).

[5] Wu B.Z., Feng T.Z., Sree U., Chiu K.H., Lo J.G.: **"**Sampling and analysis of volatile organics emitted from wastewater treatment plant and drain system of an industrial science park", *Analytica Chimica Acta*, volume 576, issue 1, pp. 100 – 111 (2006).

[6] Grob R.L., Barry E.F.: "Modern practice of Gas Chromatography", *Published by John Wiley & Sons*, 4th edition (2004).

[7] Dziuban J.A., Mroz J., Szczygielska M. et al.: "Portable gas chromatograph with integrated components", *Sensors & Actuators A (physical)*, volume 115, issues 2-3, pp. 318 – 330 (2004).

[8] Radadia A.D., Morgan R.D., Masel R.I., Shannon M.A.: "Partially buried microcolumns for micro gas analyzers", *Analytical Chemistry*, volume 81, issue 9, pp. 3471 – 3477 (2009).

[9] Kaanta B.C., Chen H., Zhang X.: "A monolithically fabricated gas chromatography separation column with an integrated high sensitivity thermal conductivity

detector", *Journal of Micromechanics and Microengeneering*, volume 20, issue 5, pp. 1 – 6 (2010).

[10] Agah M., Wise K.D.: "Low-Mass PECVD Oxynitride Gas Chromatographic Columns", *Journal of Microelectromechanical Systems*, volume 16, issue 4, pp. 853 – 860 (2007).

[11] Cardinali G.C., Dori L., Fiorini M. et al.: "A smart sensor system for carbon monoxide detection", *Analog Integrated Circuits and Signal Processing*, volume 14, issue 3, pp. 275 – 296 (1997).

[12] Nicoletti S., Dori L., Cardinali G.C., Parisini A.: "Gas sensors for air quality monitoring: realisation and characterisation of undoped and noble metal-doped SnO_2 thin sensing films deposited by the pulse laser ablation", *Sensors & Actuators B (Chemical)*, volume 60, issues 2-3, pp.90 – 96 (1999).

CHAPTER 2

PORTABLE GAS-CHROMATOGRAPHIC MODULE FOR BTEX ANALYSIS

2.1 – MOTIVATIONS AND INTRODUCTION

As already mentioned in the introduction, capillary air quality monitoring and environmental pollutants analysis has become mandatory in many locations, to ensure healthy living conditions, and in this scenario a great interest is addressed to the analysis of aromatic Volatile Organic Compounds (VOC), i.e. chemical compounds which can significantly affect environment and human health because of their potential toxicity even at low concentrations (parts per billion or less).

For quantifying environmental pollutants, gas chromatographic (GC) techniques are widely employed and currently used.

Since several years, the Institute for Microelectronics and Microsystems (IMM) – Section of Bologna is involved in a rapidly expanding research sector, whose activities are mainly focused on the design, fabrication and characterization of multi-sensorial systems based on silicon devices and able to perform analysis of complex gaseous mixtures for applications like air quality monitoring and agro-food quality assessment.

As far as it concerns the former topic, the goal of the research activity carried out at the IMM (and within which my doctorate activity was developed) consisted in the fabrication of a miniaturized innovative GC system, based on silicon micromachining technology, aiming at the detection of ppb or sub-ppb level aromatic VOCs, specifically Benzene, Toluene, Ethyl-benzene and Xylene (BTEX) eluted in air.

In Fig. 2.1, a schematic representation of the mini-GC system architecture is presented (micro-fabricated parts are highlighted in bold):

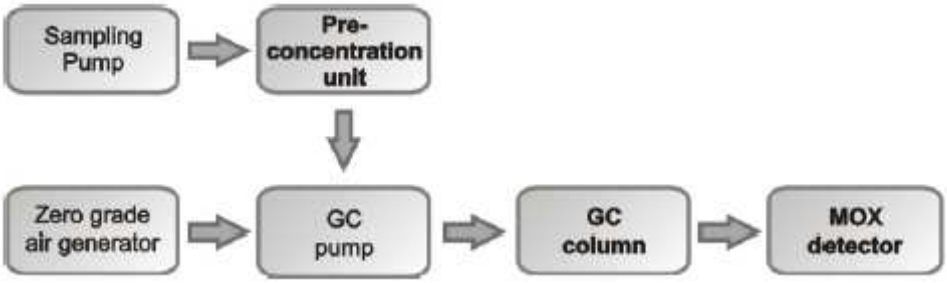

Fig. 2.1 – Schematic representation of the system architecture.

As already mentioned in the introduction, three functional blocks compose a GC-system: i) injection system, ii) separation column and iii) detector.

The micro-GC developed at IMM, however, is characterized by a series of innovative features, presented in the following list:

- The system does not require a carrier gas cylinder, since the used stationary phase is filtered air, generated on-board by means of an activated carbon filter (zero grade air generator in Fig. 2.1). This fact make the system portable, easy to deploy and suitable for in-field use.
- The pre-concentration unit consists of a micro-machined silicon cartridge containing an innovative supramolecular phase (described in the following section) [1].
- A GC separation column (presented in section 2.3) and a Metal OXide semiconductor (MOX) sensor (described in section 2.4) have been successfully combined in a GC-system which uses filtered air as carrier gas: it was possible because the stationary phase distributed along the column is not damaged by oxygen, while MOX sensitivity to VOCs is considerably increased by the presence of oxygen molecules.

The basic operational sequence of the GC-system is as follows:

a) Initially, the module operates in sampling mode, i.e. the *sampling pump* provides a constant flow of outdoor air (sample) through the pre-

concentration column, while at the same time the *GC pump* cleans the separation column by means of filtered air (carrier gas).

b) When the sampling pump has taken a given volume of outdoor air, the pre-concentration column is connected to the GC pump and heated: the adsorbed aromatic VOC are thus released and consequently injected into the separation column.

c) After the injection, the flow is returned in sampling mode while the MOX sensor placed downstream of the column acquires the signals of the separated components as they exit the column outlet.

   After the acquisition of the complete chromatogram, the detector is switched off and the system returns to sample a new volume of air for the next acquisition.

In the subsequent sections, the functional micro-fabricated blocks of the GC module will be described, focusing on the design methodologies, technological processes, simulations and experimental results.

2.2 – PRE-CONCENTRATION UNIT.

The aim of a pre-concentration device is to collect volatile and semi-volatile compounds from large-volume vapour sample and inject the compounds into the gas chromatographic column as narrow vapour plugs.

Typical pre-concentrator configurations consist of a trap metal tube [3,4] that is cooled by a flow of cold gas (down to – 50 to – 100°C) during sample collection, and successively heated in order to release the sample through a rapid thermal desorption mechanism.

The micro-fabricated pre-concentration column developed at IMM, instead, consists of a micro-machined silicon cartridge (1.4 x 2.5 cm^2, see Fig. 2.2a), filled with a innovative phase (a mesh of quinoxaline-bridged cavitand, see Fig. 2.2b) which replaces the previously described metal tube in the purge and trap mechanism, integrated with a platinum heater and a temperature sensor

The function of the column, in fact, is the absorption of the VOCs present in outdoor air when the system is in sampling mode, and their subsequent release due to a rapid thermal desorption during the injection phase, when the cartridge is connected to the separation column via the GC pump.

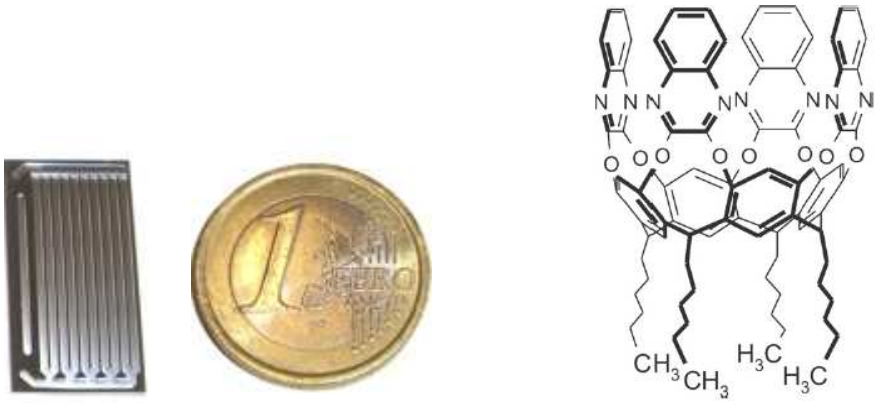

(a) *(b)*

Fig. 2.2 – Silicon micro-machined pre-concentration column compared with 1 euro coin (a), molecular structure of the quinoxaline-bridged cavitand [1] (b).

2.2.1 – Device design and technological process.

The micro-machined pre-concentration devices are made by 8 parallel channels with a variable length from 16mm to 20mm and a cross section area of 1mm x 0.8mm = 0.8mm^2

This choice was done on the basis of two considerations: i) the pre-concentration column is not used to separate compounds, so the channel length can be relatively small (with respect to separation column), and ii) 8 parallel channels ensure that the pre-concentrator can be filled with a sufficient amount of cavitands, while a cross section area of 0.8mm^2 allows a simple cavitands introduction.

The process flow for the fabrication of the column is depicted in Fig. 2.3 (a – f) and consists of the following steps:

a) on the surfaces of a 4 inches – double polished silicon wafer (thickness = 1mm),

b) a 5.5µm-thick Low Thermal Oxide (LTO) layer is deposited,
c) and patterned on the front side, acting as mask layer for the subsequent
d) Deep Reactive Ion Etching (D-RIE) silicon process aimed at defining 800µm-deep channels to be filled with cavitands.
e) On the back side of the wafer, a 240nm-thick platinum film is deposited and lift-off patterned, for the fabrication of the integrated heater and temperature sensor (to control the rapid thermal desorption).
f) Finally, channels inlet and outlet are obtained on a pyrex wafer through laser cutting process and the two wafers (Silicon + Pyrex) are fixed together via anodic bonding process, to enclose the column channels.

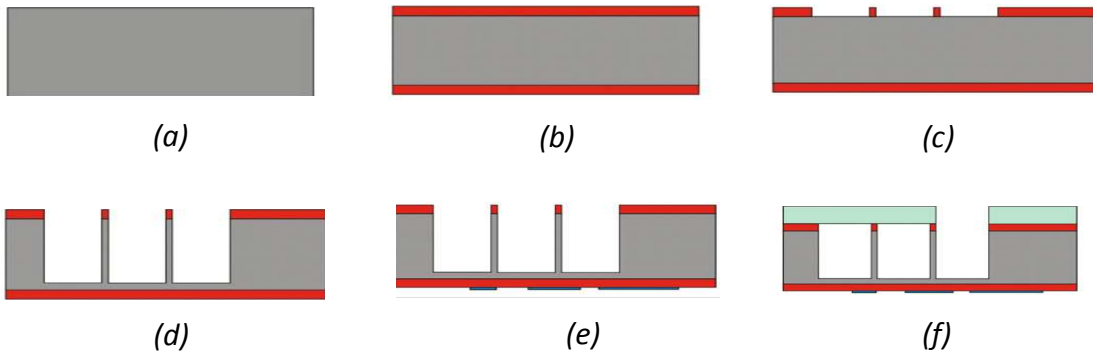

Fig. 2.3 – Technological process for column fabrication.

The technological flow, hence, relies only on two lithographic masks, one for channels fabrication and one for platinum heater and temperature sensor definition.

Mask layouts, designed by using CADENCE© software, are shown in Fig. 2.4: as it can be noticed, the fabricated silicon wafers contain 10 cartridges, plus defined test structures. As previously mentioned, the micro-machined pre-concentration devices are made by 8 parallel channels with a variable length from 16mm to 20mm (depending on the chip typology) and a single cross section area of 0.8mm^2, while platinum heater and temperature sensor were designed keeping as constraints their resistance values at 0°C, respectively 15Ω and 105Ω.

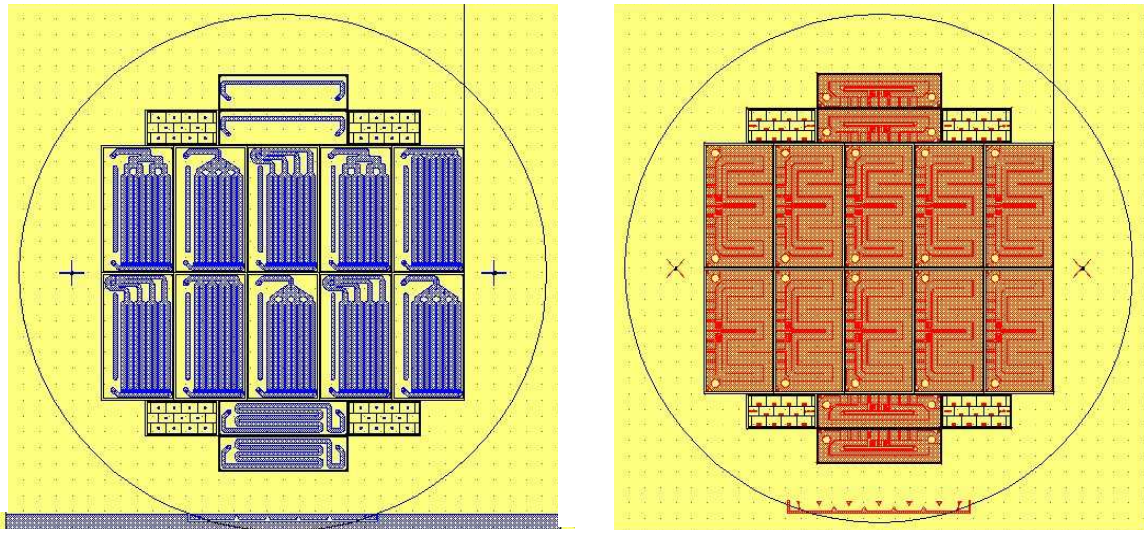

Fig. 2.4 – Mask layouts: channels (left) and platinum metallizations (right).

Different channels mask layouts, together with heater and temperature sensor, are depicted in the following figure:

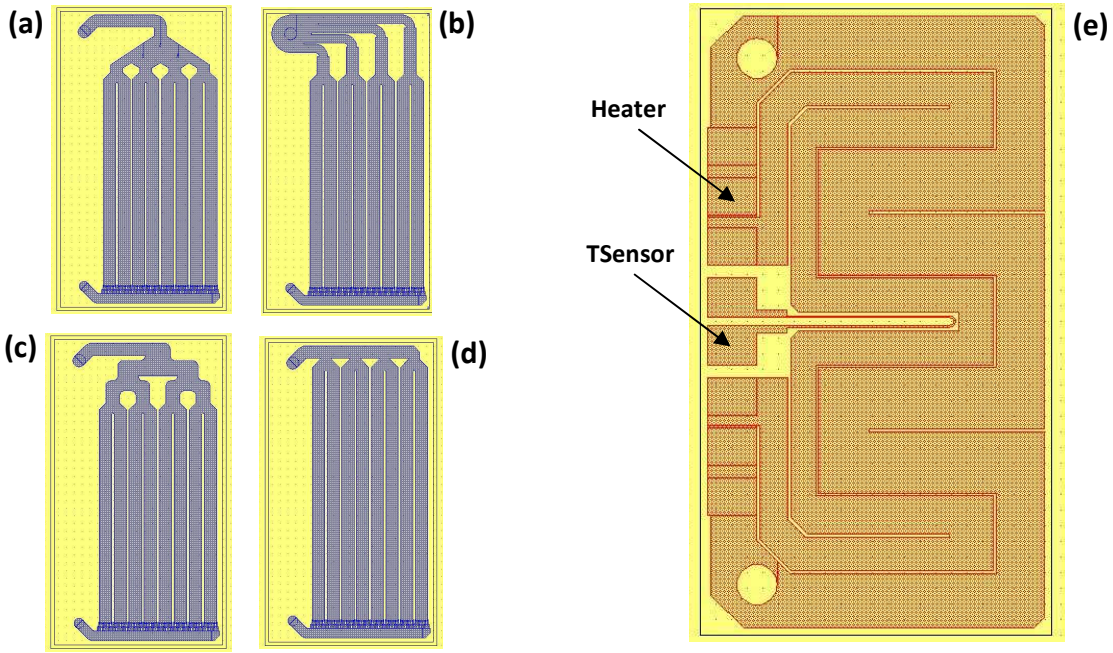

Fig. 2.5 – Example of channels layouts (a – d) and platinum heater and TSensor (e): pictures not in scale.

the choice of designing four different mask layouts for the pre-concentration channels derives from the necessity to carry out the channels configuration that ensures the filling with cavitands as uniform as possible.

By this purpose, various tests were performed on the different structures and the one reported in Fig. 2.5-b resulted the most promising, due to the uniformity of fluidic impedance provided by the four different inlet paths.

As far as heater layout is concerned, it was designed so that it covers the whole chip region (i.e. the channels region), to have a temperature distribution over the chip surface as uniform as possible

2.2.2 – Experimental characterization.

A thorough experimental campaign was performed on the fabricated wafers (by using an appropriate wafer-level parametric characterization system), to investigate the distribution of heater and temperature sensor resistance values in the various chips.

To do that, resistance values at RT = 25°C were derived, together with the Temperature Coefficient of Resistivity (TCR) of platinum thin film (since it is expected to differ from the value reported in literature for bulk platinum, i.e. 0.0038 1/K), in order to evaluate resistances @ 0°C via the formula:

$$R(0°C) = \frac{R(25°C)}{1 + TCR \cdot 25} \qquad (1)$$

In particular, precise value of TCR (**0.00278 [1/K]** $\pm$ $3 \cdot 10^{-5}$) was obtained by using specific Kelvin resistor test structures replicated in every chip within the wafer (the methodology will be fully described in chapter 4).

Experimental results @ 0°C are reported in the following table:

	TARGET	AVERAGE VALUE	ERROR
HEATER RESISTANCE (Ω)	**15**	**14.9**	**± 0.05Ω**
TSENSOR RESISTANCE(Ω)	**105**	**105.7**	**± 0.1Ω**

Tab. 1 – Experimental values and temperature sensor resistances @ 0°C.

Due to a lack of uniformity of platinum deposition over the wafers surface, resistance values of heaters and temperature sensors are not constant for every chip, but varies from a minimum of 14Ω (chips placed in central positions) to a maximum of 16Ω (chips placed in peripheral positions) for the heater and from a minimum of 103.5Ω (central chips) to a maximum of 107.5Ω (peripheral chips) for temperature sensors.

After the wafer level electrical characterization, the devices were separated by using a dicing saw, to be individually characterized with an appropriate experimental set-up to evaluate their thermal transients, since the sample desorption takes place by heating the pre-concentration unit up to temperatures around 200°C.

The single chip was hence mounted on a specifically designed Printed Circuit Board (PCB) module (as depicted in Fig. 2.6), connecting the heater pads to a 2400 Keithley multimeter by means of two electrical wires (red and black), and the temperature sensor pads to a 2410 Keithley multimeter by means of the blue wires.

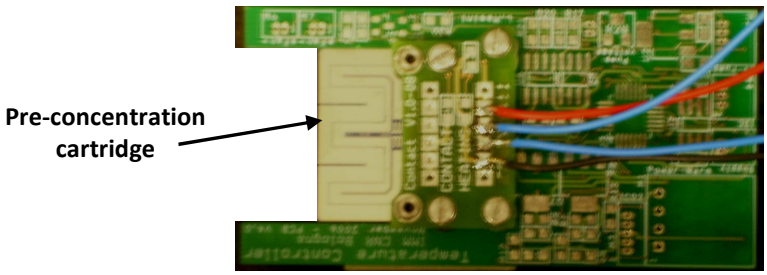

Fig. 2.6 – Pre-concentration chip mounted on a electronic board.

The temperature sensor was constantly biased with a 5mA electrical current, while the heater was biased with a constant voltage of 12V (the same voltage provided by the control electronics that drives the GC-system); the temperature value was achieved by measuring with a constant time step (1 sec) the resistance of the temperature sensor and applying the well known formula:

$$T(K) = \frac{1}{TCR} \cdot \left(\frac{R_{TS}}{R_{TS}(273.15K)} - 1 \right) \quad (2)$$

being R_{TS} the temperature sensor resistance and TCR = 0.00278 (1/K), as previously mentioned.

A measurement cycle of 300 seconds was considered, and the result is reported in the following figure: as can be disclosed, the pre-concentration chip reaches 200°C after 45 seconds and successively settles to a steady value of 235°C.

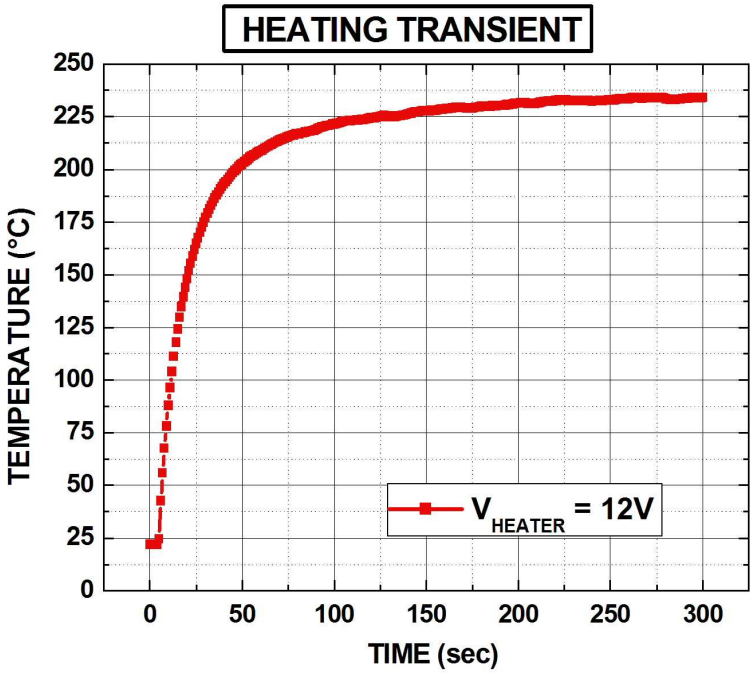

Fig. 2.7 – Heating transient of the pre-concentration unit.

2.2.3 – Cavitands efficiency evaluation.

After performing the electrical and thermal characterization, the single chips can be finally filled with cavitands and employed in the mini-GC system.
Filling technique is as follows:

- first, cavitands were crystallized from acetone, and the resulting crystalline powder was passed through 35–60 mesh sieves, collecting particles of 420 ÷ 730μm in diameter (to obtain a material with sufficient homogeneity),
- subsequently, mesh was provided at the column inlet while applying vacuum on the column outlet: to prevent the cavitands from being pushed out of the column by the gas flow, a micro-machined silicon filter was implemented in the channels outlet side, as shown in detail in the following picture:

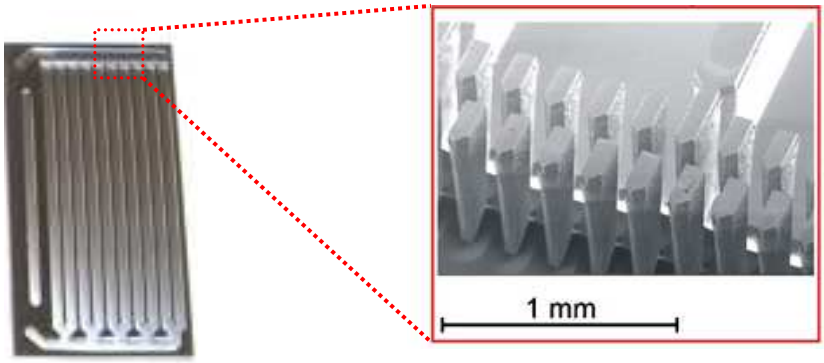

Fig. 2.8 – Pre-concentration channels together with micro-machined filter (inset).

To evaluate pre-concentration column performances, an experimental set-up was prepared, aimed at testing the absorption efficiency of cavitands towards volatile organic compounds: in particular, 20 ppb of benzene were injected for 15 minutes in a pre-concentration cartridge, whose outlet was connected to a detector, and by comparing two different responses of the latter, (at first in case of an empty cartridge and subsequently in case of a cartridge filled with 54 mg of a QxCav mesh), the high absorption efficiency of the considered cavitands clearly appeared, as shown in the following picture:

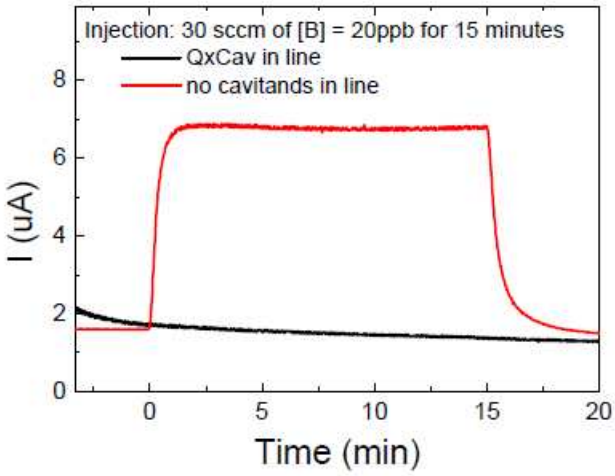

Fig. 2.9 – Measurement of cavitands absorption efficiency: no QxCav in line (red line) vs. QxCav in line (black line).

2.3 – GC SEPARATION COLUMN.

Gas chromatographic separation column can be considered as a key item in a gas chromatograph, since it specifically allows to perform a qualitative analysis (in addition to a quantitative one) of the sample mixture, by temporally separating the single compounds.

Chromatography, in fact, deals with separation of components of a mixture by a series of equilibrium operations that result in separation of the entities as a result of their partitioning, as already mentioned, between two different phases, one stationary with a large surface and the other moving (also called carrier) in contact with the first.

A brief description of separation mechanism has been given in introductory chapter (section 1.2), without providing a precise description of the effective mechanisms by which sample components separation is achieved.

Going into detail, the separation technique that offers the greatest advantages, and which is used in the shortly introduced columns, is the so called *elution development* [5].

As far as it concerns its working principle, suppose for the sake of simplicity that sample mixture is formed by only two components, A and B: elution technique is based on the assumption that components A and B travel through the column at rates determined by their retention on the stationary phase, so that if the differences in sorption are sufficient and the column is long enough, a complete separation of A and B can be obtained .

A possible disadvantage of this technique is the very long time interval required to remove a highly adsorbed component but, as will be successively described, this can be overcome by properly increasing column temperature during separation process.

On the other hand, a great advantage of elution is that, with respect to other separation mechanisms such as *frontal technique* or *displacement development*, at the end of a separation, no sample trace remains in the column, thus the latter does not have to be regenerated before it can be used again.

In the following figure, a simplified example of chromatogram obtained through elution technique is presented (mixture formed by three components A, B and C) [5]:

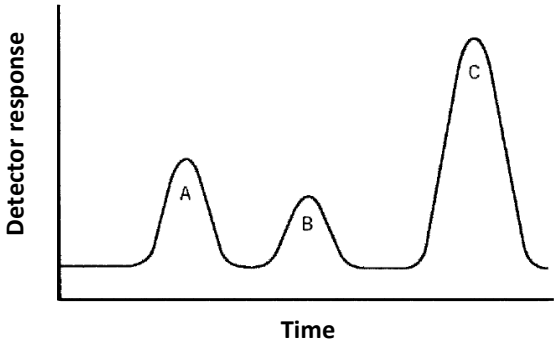

Fig. 2.10 – Example of chromatogram achieved by elution. Order of retention: C > B > A.

Two different prototypes of micro-machined silicon packed columns were designed and fabricated to be employed in the mini-GC system (based on the same technological process previously described for the pre-concentration columns) and in next two sections their peculiar features will be presented:

2.3.1 – 50cm-long packed column.

The first prototype consisted in a 50cm-long double spiral shaped separation column, obtained through silicon micromachining (see Fig. 2.11): the square section of the etched channels has a cross-section area of 0.64 mm^2 (channel width = channel depth = 0.8mm).

The surface of the 4-inches silicon wafer containing the columns is encapsulated with a pyrex wafer, while on the opposite surface an integrated platinum resistor and a temperature sensor were deposited, to allow precise thermal modulations of the GC column temperature.

Fig. 2.11 – 50cm-long separation column compared with 1 euro coin.

The latter parameter, in fact, has a great influence on column selectivity and on its capability to correctly resolve peaks, and for this reason the faculty of performing

programmed-temperature chromatographic cycles (changing systematically the temperature of the column during a part or the whole of the separation) may assess the analysis and improve peaks separation.

Moreover, by opportunely heating the separation column, the time spent by specific compounds to pass through the column can be decreased, and consequently the analysis cycle can be accelerated.

In Fig. 2.12, mask layouts of the double spiral-shaped column and of the 240 nm-thick platinum metallizations for heater and temperature sensor are presented (chip dimensions = 2.5 x 2.5 cm^2): in particular, platinum heater consists of 13 parallel tracks, whose design was optimized in such way that each track is characterized by equal Joule dissipated power density.

Target values at 0°C for resistances were the same reported for the pre-concentrators (15Ω for heater and 105Ω for temperature sensor).

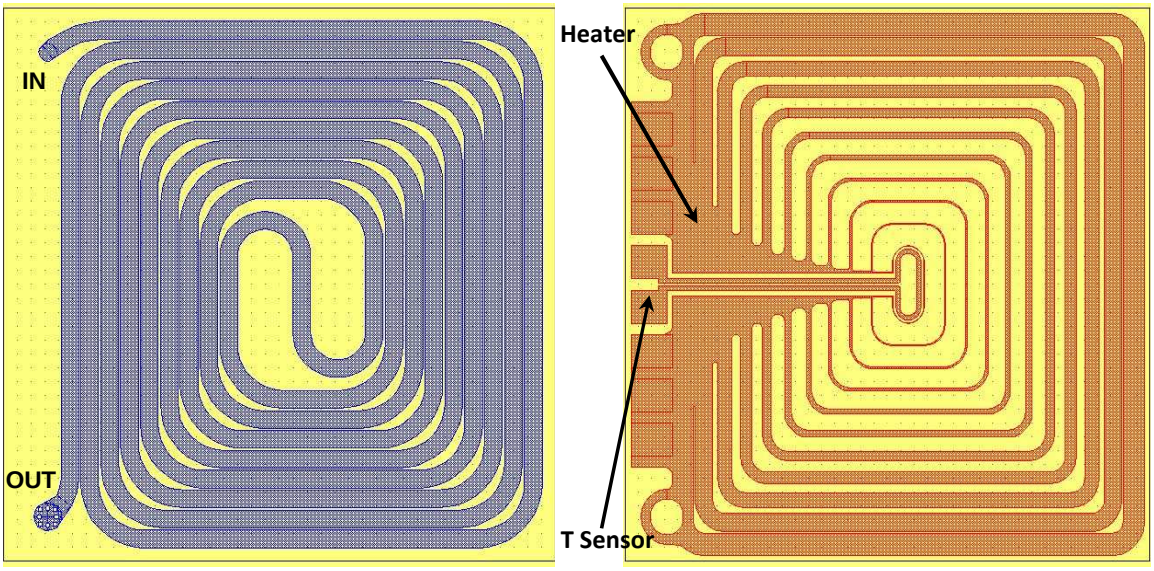

Fig. 2.12 – Separation column: mask layout for channels (blue) and for platinum Heater and Temperature Sensor (red).

An experimental campaign analogous to the one previously described for pre-concentrators was performed on the fabricated wafers, to investigate the distribution of heater and temperature sensor resistance values in the various chips, and results at 0°C are reported in the following table:

	TARGET	AVERAGE VALUE	ERROR
HEATER RESISTANCE (Ω)	15	14.4	± 0.05Ω
T SENSOR RESISTANCE (Ω)	105	104	± 0.1Ω

Tab. 2 – Experimental values of Heater and Temperature Sensor resistances at 0°C.

Device heating transient was evaluated by using the same set-up employed for the pre-concentrator and the result is reported in the following figure:

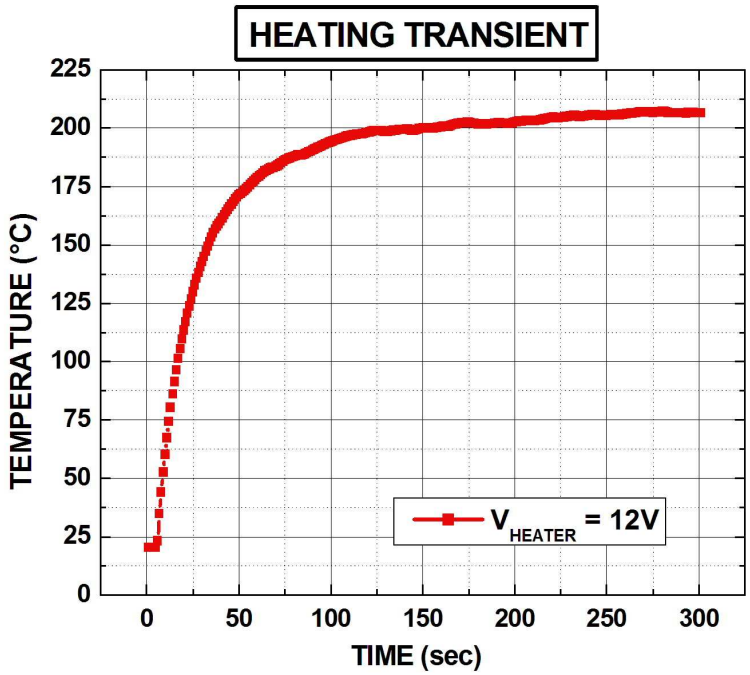

Fig. 2.13 – Heating transient of the separation column chip (2.5x2.5 cm^2).

The separation column chip settles to a steady value of 206°C, about 30°C less than the pre-concentrators at the same operating conditions: this is due to the higher heat exchange through the larger device surface.

2.3.2 – 100cm-long packed column.

The second prototype consisted in a 100cm-long double spiral shaped separation column, obtained through silicon micromachining (chip dimensions = 2.5 x 4.5 cm^2, see Fig. 2.14): etched channels square section has the same cross-section area of the 50cm-long column.

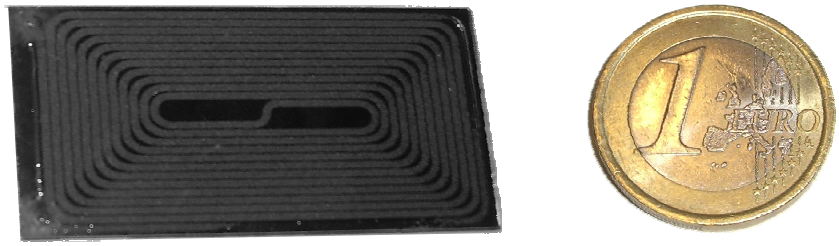

Fig. 2.14 – 100cm-long separation column compared with 1 euro coin.

The principal factor that discriminates the good quality of a separation column is its resolution (i.e. the capability to separate and distinguish similar molecules), and one of the possible methodologies to improve the latter (and consequently the overall column performances) consists in increasing the column length.

This is the motivation of the second typology of GC column, whose mask layouts are depicted in Fig. 2.15:

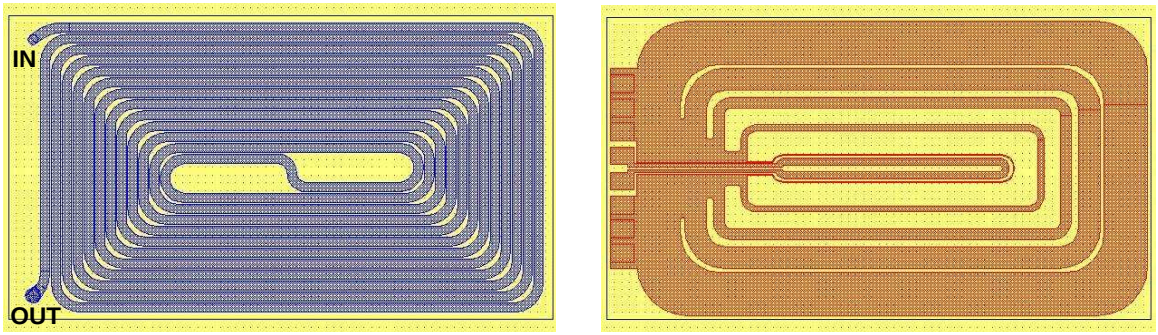

Fig. 2.15 – Separation column layout (left), platinum Heater and T Sensor (right)

Technological process and platinum heater and temperature sensor resistance values are the same of the 50cm-long column, while in the following picture the heating transient of the structure is reported: as it can be noticed, the 100cm-long separation column chip settles to a steady value of 175°C, about 60°C less than the pre-concentrators and 30°C less than the 50cm-long column at the same operating conditions: still, this is due to the higher heat exchange through the larger device surface.

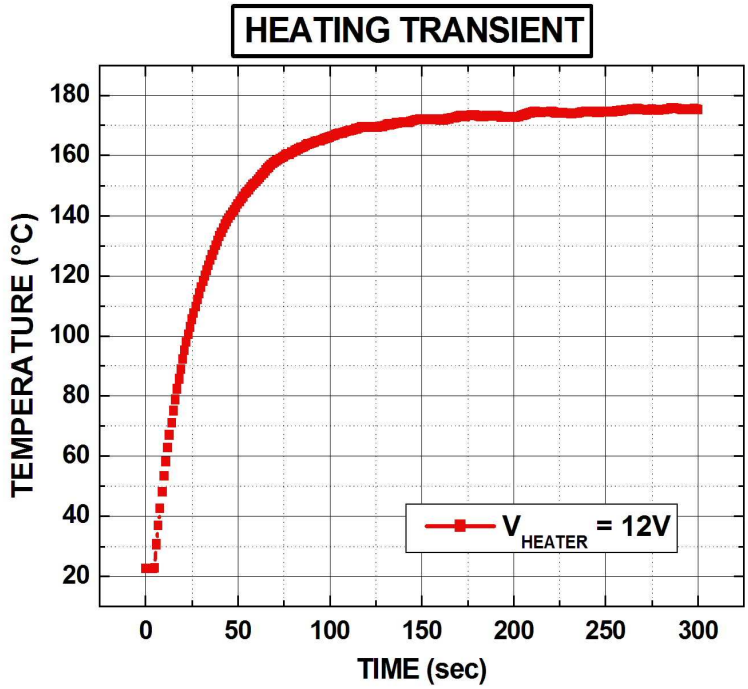

Fig. 2.16 – Heating transient separation column chip (2.5x4.5 cm^2).

The 4-inches wafer where the micro-columns are fabricated on is formed by 5 devices (specifically, three 50cm-long and two 100cm-long), disposed as illustrated in Fig. 2.17:

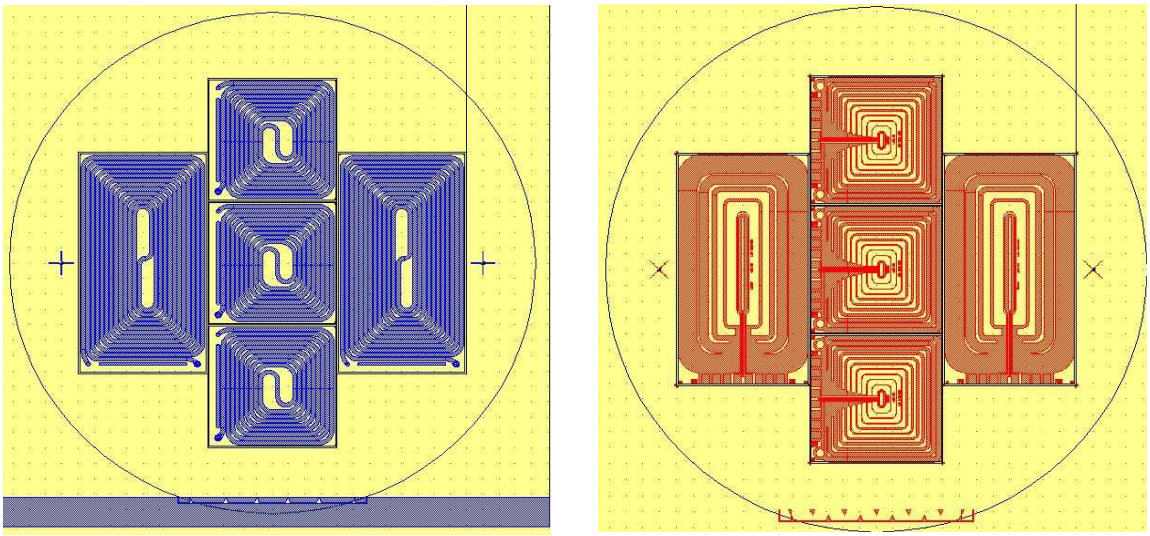

Fig. 2.17 – Mask layouts: channels (left) and platinum metallizations (right).

After performing the electrical and thermal characterization, the single chips can be filled with the stationary phase and employed in the mini-GC system.

In particular, since the channels packing procedure consists of providing small amounts of stationary phase (Carbograph 2 + 0.2% Carbowax™ with 80 – 100 mesh) at the column inlet while applying vacuum at the column outlet, as in the case of the pre-concentrator the outlet side of the separation column (both for 50cm-long and for 100cm-long) features a micro-machined filter, to prevent the stationary phase from exiting the column under vacuum processing (see next figure for details):

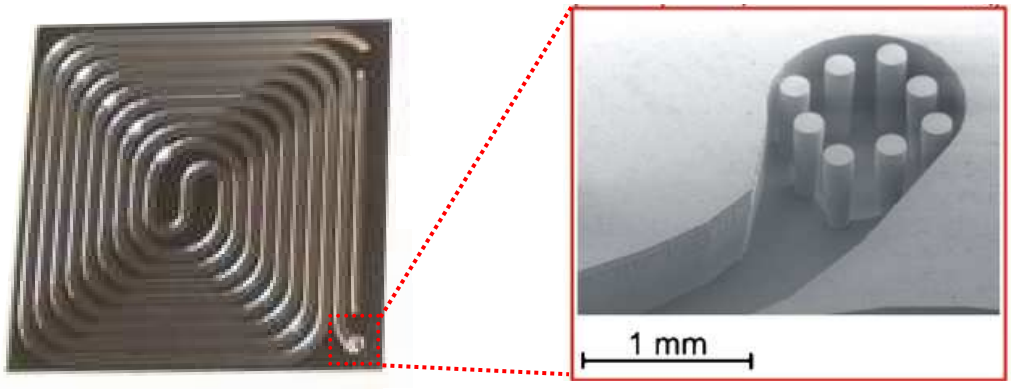

Fig. 2.18 – Separation column channels together with micro-machined filter (inset).

2.4 – METAL OXIDE (MOX) DETECTOR.

The last block of the developed mini-GC is the detector, i.e. the sensitive element that, interacting with the compounds of the sample mixture exiting the separation column, reveals and quantifies their individual amount (hopefully with the best sensitivities and the proper response times).

In literature, a huge variety of detection systems for GC is proposed, e.g. Thermal Conductivity Detector (TCD), Flame Ionization Detector (FID), Photo Ionization Detector (PID) [6 - 8], and one must select from time to time the appropriate typology for the particular application.

Since the target of this research activity, as mentioned at the beginning of this chapter, deals with the analysis of aromatic VOCs, the detector must have an extremely high sensitivity (limit of detection in the order of ppb or even sub-ppb) and selectivity towards these specific compounds.

In addition, as already mentioned in the introductory chapter, since the target is the development of a completely micro-fabricated GC-system, constraints related to small

sizes and low power consumption must be taken into account, to fulfil the requirement of extremely low dead volumes.

The solution adopted to satisfy all the mentioned requirements was to design and fabricate a silicon micro-machined chemo-resistive sensor, based on a Low-Power consumption hotplate supporting a thin sensitive film (nano-metric thickness) of a Metal OXide (MOX) material (ZnO_2 and SnO_2 are typically the most used), whose detection capability emerges when the thin film, , exposed to specific compounds, is heated up to working temperatures of 250 ÷ 450°C [9, 10].

At such temperatures, in fact, physico-chemical interaction mechanisms of oxidation-reduction take place and cause variations in film properties: in particular, changes result in its electrical conductance, thus by connecting the film with two electrodes and monitoring the variations of the electrical current flowing through them, the presence and concentration of compounds, e.g. VOCs, can be easily disclosed and measured.

As far as the mini-GC system is concerned, MOX sensor employed into the module was designed and realized at IMM-Bologna Section at the end of 90's [11, 12] and consists of SnO_2 nano-metric film deposited over a silicon micro-machined substrate implemented with platinum heater, temperature sensor and two electrodes for contacting thin sensitive element.

Wafer-level process employed for sensors fabrication allowed to carry out, on the surface of a 4 in. wafer, 106 gas sensor arrays, each comprising four completely independent detectors (as shown in the following figure):

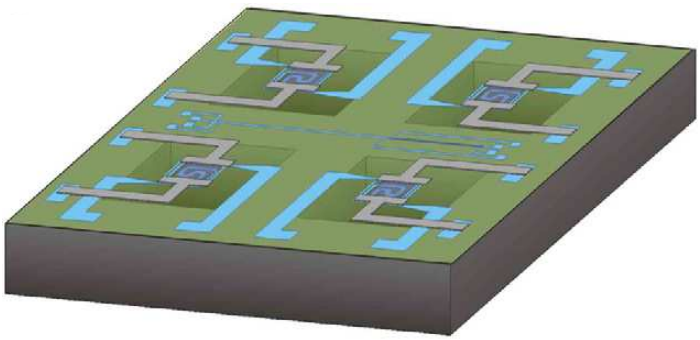

Fig. 2.19 – Picture of the single chip containing MOX sensors array [12].

Silicon chip size is 5 x 5mm^2 with an active area (for each of the four sensors) of 1 x 1mm^2, consisting of a 200nm-thick Si_3N_4 supporting membrane released through a silicon backside D-RIE etch (using a 40 wt% KOH solution at 80°C), covered with a TiN adhesion layer for double spiral-shaped platinum resistor (see Fig. 2.21-a) acting as heater (metallizations thickness = 240nm) .

On the top of the resistor, a passivation layer is deposited (to provide electrical insulation between the platinum heater and the sensing layer), and over its surface the two T-shaped platinum electrodes for contacting thin film are defined (see Fig. 2.21-a).

A schematic representation of the whole structure is depicted in the following figure:

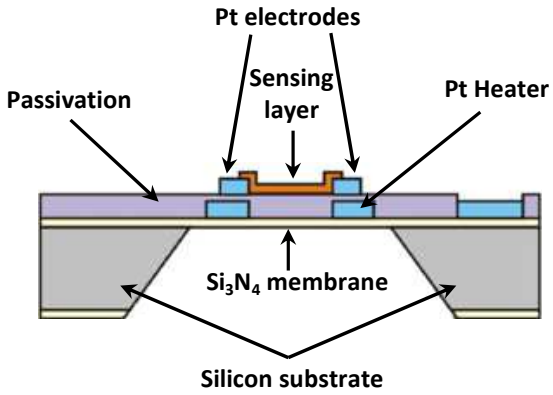

Fig. 2.20 – Sensor device structure (cross section).

SnO_2 thin film deposition over the hotplate surface has been carried out by sputtering through a Modified Rheotaxial Growth and Thermal Oxidation (M-RGTO) technique [13] (overall sensing layer thickness ranges from 60 to 150nm) and an extremely thin Au film (nominal thickness = 5nm) was deposited over its surface, to act as a catalyst and consequently increase SnO_2 film selectivity.

A precise description of the deposition process is given in chapter 3 (section 3.1.3).

Prior to devices functional characterization, power consumption was investigated, focusing the attention on the evaluation of heater power needed to reach typical MOX sensor work temperatures (~400°C).

To do that, specific test structures were designed and fabricated in a few number of chips: in such structures, the two platinum contacting electrodes are replaced by a

meander-shaped temperature sensor (see mask layouts in Fig. 2.21-b), through which the device temperature as a function of heating power can be exactly measured.

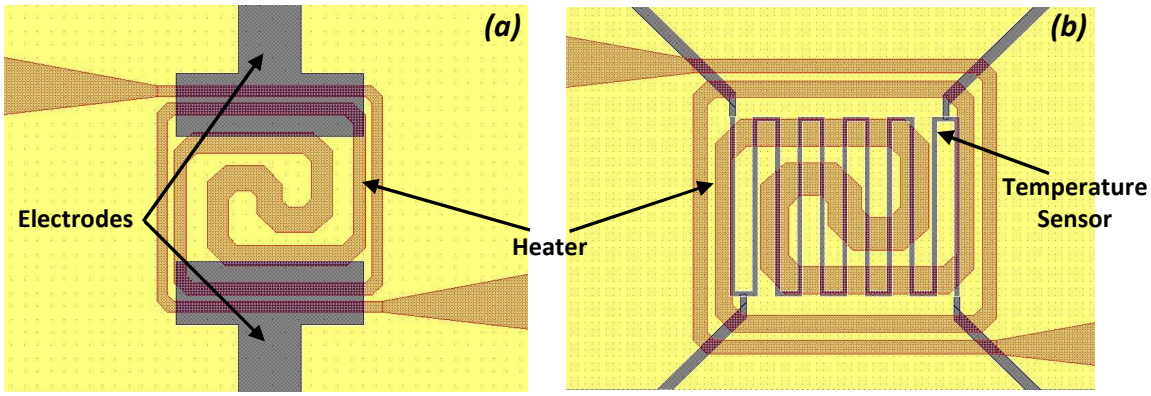

Fig. 2.21 –Mask layouts of Pt Heater (red), Electrodes (blue, (a)) and Temperature Sensor (blue, (b)).

Measurements were performed by means of a wafer-level parametric characterization system, on the basis of the following principle: a linear current sweep I_H (0.1 mA up to 20.1 mA, maintaining a constant step of 0.5 mA) has been applied to the heater and, by evaluating the corresponding electric potential V_H on the heater pads, a series of heating power values $P_H = I_H \cdot V_H$ has been obtained.

At the same time, in order to disclose the relationship between heating power and the temperature of device central region, a four-wires measurement was performed on the temperature sensor, deriving its values of resistance R_{TS} (one for every current step on the heater) and obtaining the corresponding values of temperature (Kelvin degrees) from the relation expressed in eq. (2), where TCR is the platinum temperature coefficient of resistivity, which was found to be fairly constant in the [298 K ÷ 598 K] temperature range and equal to 0.0031 [1/K] ± $2 \cdot 10^{-5}$.

Using the TCR determined above, the variation of the temperature of the central part of the hotplate as a function of the applied heater power was measured, and a typical "Temperature vs. Heater Power" curve is presented in the following figure: as it can be noticed, a power consumption value of 78mW was experimentally measured in correspondence of the typical working temperature of 400°C.

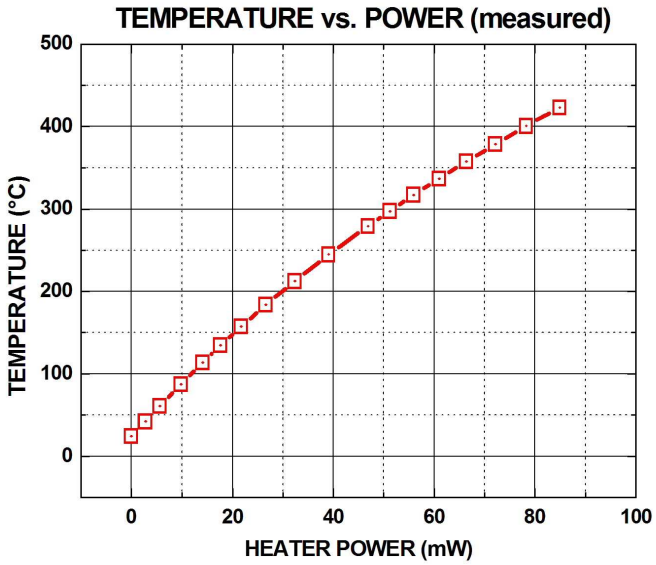

Fig. 2.22 – Device "Temperature vs. Heating Power" measured curve.

2.5 – GC-SYSTEM ASSEMBLY.

Figure 2.23 shows the complete schematic representation of the mini GC-system architecture, including control electronics and fluidic interconnections:

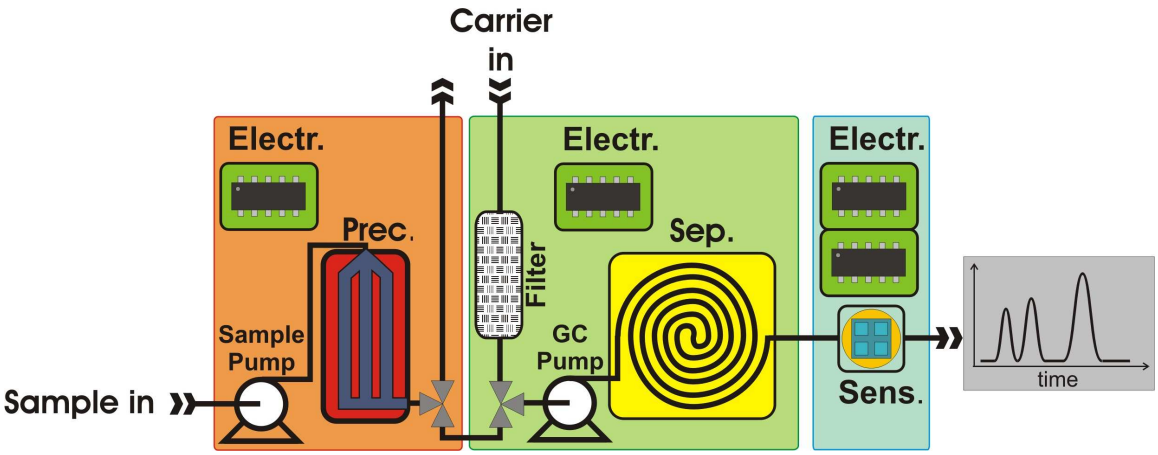

Fig. 2.23 – Complete schematic representation of the mini-GC system.

The following figure shows the complete packaged mini-GC system (pre-concentration and separation columns are visible, while the detector is hidden by the master controller PCB): packaging includes some automatically controlled fans to allow rapid cooling of the micro-columns after high temperature cycles.

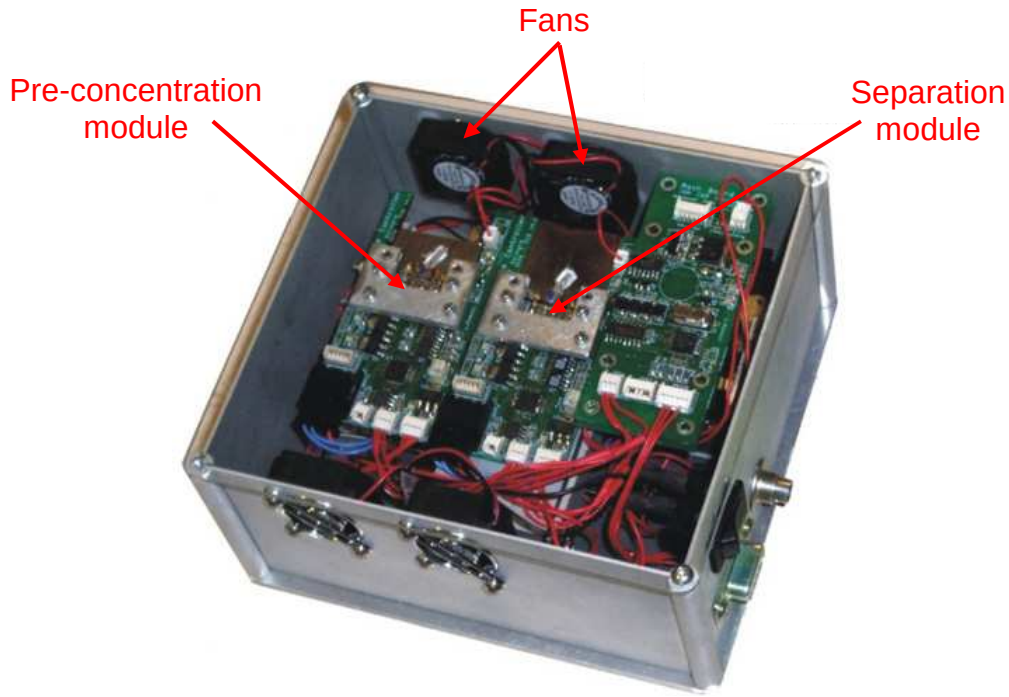

Fig. 2.24 – Picture of the complete packaged module.

The pneumatic interconnection circuit is provided by three modular stainless steel blocks, one for each GC function: pre-concentration, separation and detector.

As an example, the separation block is shown in Fig. 2.25, where the fluidic interconnections between the micro-machined columns and the stainless steel block using Viton® O-rings can be disclosed.

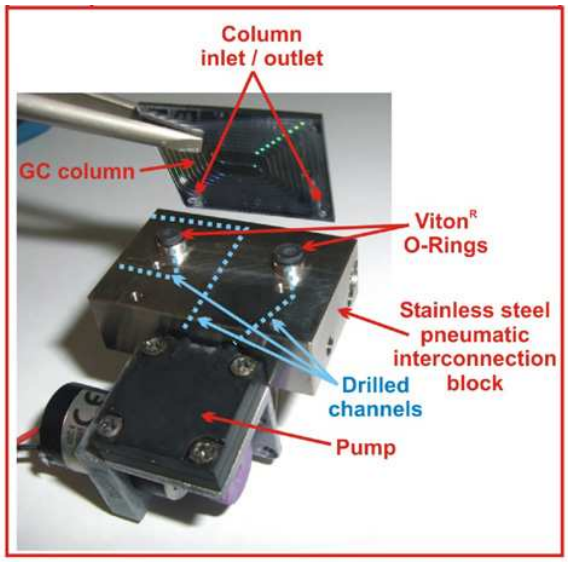

Fig. 2.25 – Pneumatic interconnections for the micro-column module.

Flows are forced through the pneumatic circuit by two commercial mini-pumps: the "sampling pump" provides a constant flow of approximately 50 sccm of the analyzed sample through the pre-concentration column (which retains the aromatic volatiles), while the second pump (indicated with "GC pump" in the schematic of Fig. 2.23), provides the flow of purified air (carrier gas) through the separation column.

Since the latter is characterized by a higher impedance with respect to the pre-concentration column, approximately 15 sccm of carrier gas flow through the separation column.

Each micro-component of the system is mounted on a specific electronic module board: the micro-columns control electronics, together with the mini-pump and the mini-valve mounted on the respective stainless steel block, handle the temperature of the micro-machined columns, while the sensor array control board handles the heating and readout of the MOX sensors array, the communication with the other electronic boards (via an I^2C bus) and the serial interface towards an external PC, which handles the system control and data storage.

The disassembled modules are presented in the following pictures:

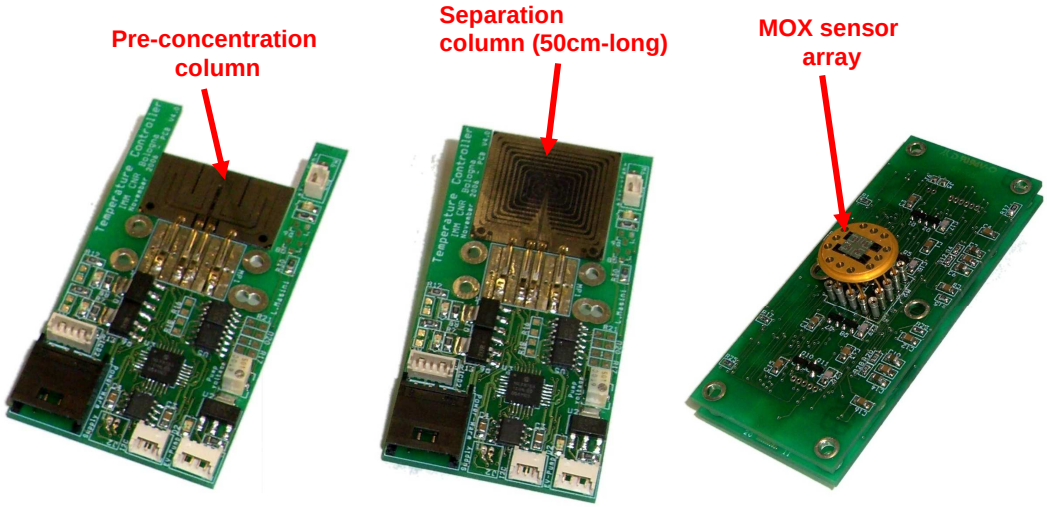

Fig. 2.26 – Single micro-components with their specific control electronics.

2.6 – EXPERIMENTAL RESULTS.

In this section, few examples of experimental analysis of sample mixtures (typically VOCs compounds eluted in synthetic air), performed in laboratory by means of the previously

described packaged mini GC-system, will be reported together with the most relevant results.

2.6.1 – Packed columns performances.

In order to investigate 50cm-long packed columns performance, the packaged mini-GC system was tested in laboratory and exposed to a synthetic mixture of aromatics compounds (benzene, toluene, ethyl-benzene and xylene), eluted in synthetic air at given concentrations and provided by a gas distribution system at a constant flow of 500sccm to a sampling chamber at atmospheric pressure.
As far as the operating conditions are concerned, the system was programmed to:

- Initially sample the test mixture at a constant flow of 200sccm from the 500sccm flow from the sampling chamber into the pre-concentration unit for 55 minutes (the exceeding flow entering the sampling chamber from the gas distribution system is flushed to vent).
- Subsequently heat the pre-concentration column to the desorption temperature of 100°C for 2 minutes.
- Switch a valve to connect the outlet of the purge and trap cartridge to the inlet of the GC pump, which drives the released VOCs through the 50cm-long separation packed column.
- Finally acquire the chromatogram by means of the MOX detector (encapsulated in a mini chamber similar to the one described in Fig. 3.14), as the gases are released by the separation column.

During the chromatogram acquisition, the purge and trap column is cooled down and starts the next pre-concentration cycle, since the chromatogram acquisition and the pre-concentration can be performed in parallel.
In Fig. 2.27, a set of five measurement cycles is reported, with four different analyte concentrations in the range between 0.1 ppb and 5.0 ppb, together with a reference chromatogram relative to humidified air only:

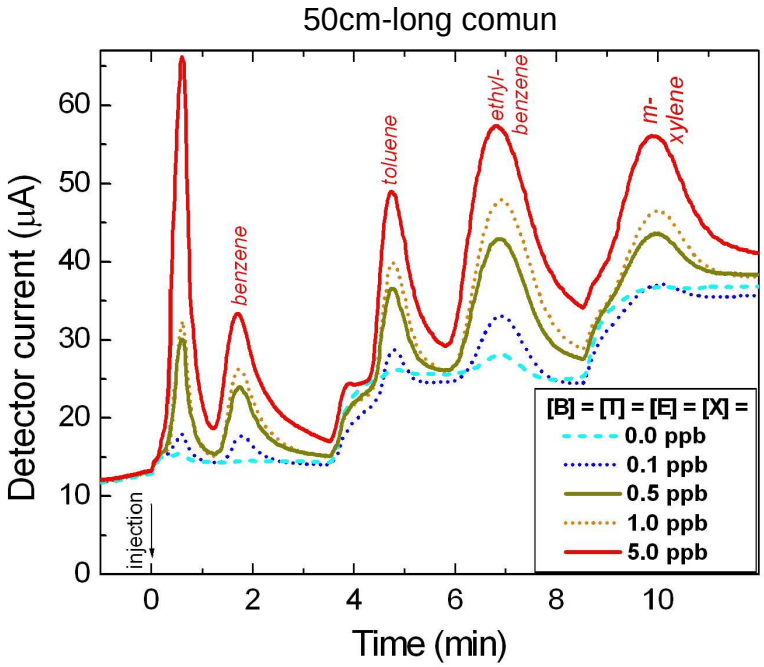

Fig. 2.27 – Laboratory chromatogram of a VOCs mixture at different concentrations: 50cm-long GC separation column used.

The measurements were not performed in any increasing or decreasing order of VOC concentrations, but in a random sequence, to investigate and exclude the effects of any systematic errors due to measurement analyte residues.

Plots clearly show that:

- after a first injection peak at T < 1 min, the four peaks relative to benzene, toluene, ethylbenzene and m-xylene are released at T = 2, 5, 7 and 10 min respectively: peaks are well separated one from another, and the increases of the baseline at T = 4 min and T = 8.5 min are relative to the increase of the GC separation column temperature to allow a faster release of the heavier analytes (programmed temperature ramp for toluene and xylene).
- Peak area increases with the analyte concentration and for all of the concentrations, including the lowest 0.1 ppb injection, peaks are clearly visible.
- Sensitivity ensured by the employed MOX sensor and selectivity ensured by the 50cm-long packed separation column are more than sufficient for monitoring applications of outdoor aromatic volatiles in the typical low ppb range.

- Analysis cycles of approximately 12 minutes can be obtained: retention time of the last eluted element (xylene) is in fact 10 minutes.

A similar experiment was performed to make a comparison between 50cm-long and 100cm-long packed separation columns: in particular, the packaged mini-GC system was exposed to a synthetic mixture of benzene and toluene at equal concentrations (1.5ppb) eluted in synthetic air.

A 18sccm flow was injected for 30 seconds in the system and driven through the 50cm-long column, initially set to a temperature of 37°C and subsequently heated up to reach a temperature of 80°C, in order to obtain a more rapid release of the toluene compound.

The corresponding chromatogram is presented in the following figure:

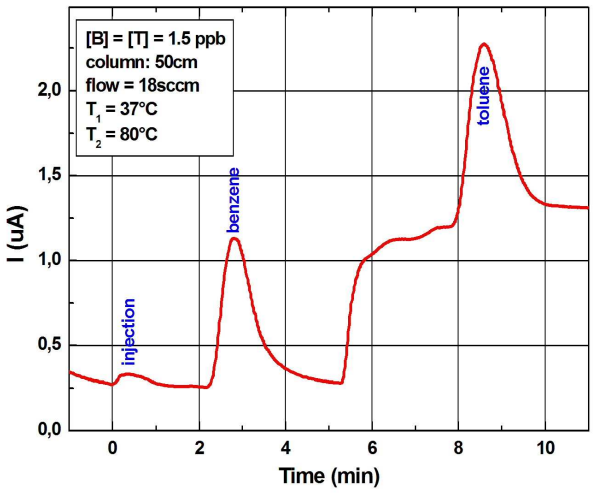

Fig. 2.28 – Laboratory chromatogram of a 1.5ppb benzene-toluene mixture eluted in air: 50cm-long GC separation column used.

Successively, the 50cm-long separation column was replaced by the 100cm-long packed column and an analogous mixture was injected in the system for 30 seconds at a volumetric flow rate of 8sccm (lower than the previous, due to the higher fluidic impedance of the new column) and driven through the 100cm-long column, initially set to a temperature of 70°C and subsequently heated to reach a temperature of 125°C (higher than the temperature values of the previous column, to obtain comparable retention times of the sample compounds).

The corresponding chromatogram is presented in the following figure:

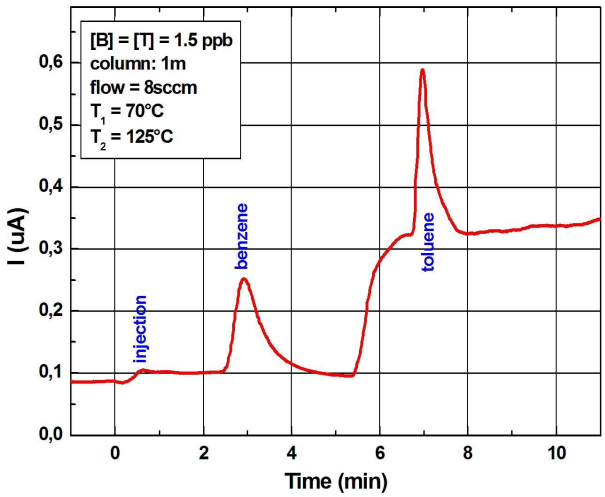

Fig. 2.29 – Laboratory chromatogram of a 1.5ppb benzene-toluene mixture eluted in air: 100cm-long GC separation column used.

From a comparative analysis of the chromatograms reported in the two previous figures, the higher separation capability of the 100cm-long column emerges, not so much for benzene peak (they have the same duration), rather for the toluene peak, given its reduced time length emerging from the chromatogram reported in Fig. 2.29 with respect to the one shown in Fig. 2.28.

2.6.2 – In-field measurements.

After long-term laboratory use, the system was preliminarily compared in-field versus the GC system most widely used in Italy, the GC855 by *Syntech Spectras* [14].

This comparison was conducted inside a monitoring station in Bologna, Italy, in collaboration with ARPA Bologna.

The trend of hourly values of benzene for the two devices is shown in the following figure: three days of continuous operations have been considered for the two instruments.

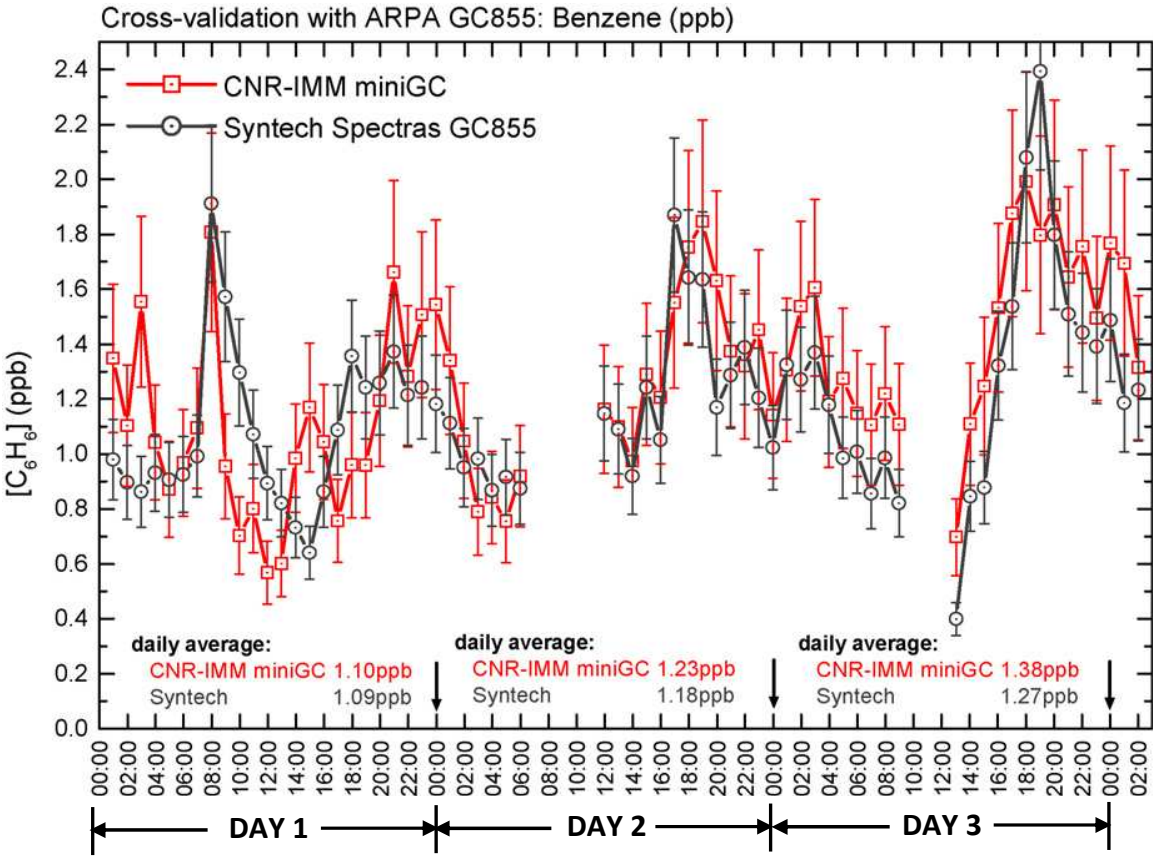

Fig. 2.30 – Cross-validation of the innovative mini-GC versus a reference GC855 by Syntech Spectras.

A very good match (especially considering the very low concentrations measured and the difference in system architectures) of the benzene measurements by the two devices can be disclosed.

As far as operating principles are concerned, the mini-GC system sampled air for 55min each hour, while the reference GC855 acquired one chromatogram every 15min and reported the average value of four measurements; furthermore, the two devices differ in detector and injection methodology.

Nevertheless, as previously mentioned, there is a very good match between the trend of the measurements: the daily average values, in fact, show a maximum deviation of 8% on the last day and as low as 1% on the first day (as reported also in the previous figure).

Finally, while comparing the performance of the mini-GC with the reference instrumentation GC855, it is important to highlight the difference in ease of use and deployment of the systems: the GC855, in fact, requires external cylinders with inert

carrier gas, temperature controlled cabins for installation, a periodic maintenance by specifically trained personnel at weekly intervals, all of these issues resulting in high operation costs.

On the contrary, the mini-GC prototype is a stand-alone analyzer which does not require external cylinders and implements automatic temperature control of all critical hardware.

REFERENCES

[1] Soncini P., Bonsignore S., Dalcanale E., Ugozzoli F.: "Cavitands as versatile molecular receptors", *Journal of Organic Chemistry*, volume 57, issue 17, pp. 4608 – 4612 (1992).

[2] Dalcanale E., Hartmann J.: "Selective detection of organic compounds by means of cavitand Coated QCM transducers", *Sensors & Actuators B (Chemical),* volume 24, issues 1-3, pp. 39 – 42 (1995).

[3] Akard M., Sacks R.D.: **"**High-speed GC air monitoring using cryointegration for sample collection", *Journal of Chromatographic Science*, volume 32, issue 14, pp. 499 – 505 (1994).

[4] Leonard C., Liu H.F., Brewer S., Sacks R.D.: "High-speed gas extraction of volatile and semivolatile organic compounds from aqueous samples", *Analytical Chemistry*, volume 70, issue 16, pp. 3498 – 3504 (1998).

[5] Grob R.L., Barry E.F.: "Modern practice of Gas Chromatography", 4th edition, *Published by John Wiley & Sons*, chapter 2, pp. 28 – 30 (2004).

[6] Cruz D., Changa J.P., Showalter S.K., Gelbard F., Manginell R.P., Blain M.G.: "Microfabricated thermal conductivity detector for the micro-ChemLab™", *Sensors & Actuators B (Chemical),* volume 121, issues 2, pp. 414 – 422 (2007).

[7] Zhang S., Zhao T.B., Xu X. et al: "Determination of BTEX compounds in Solid-Liquid mixing paint using the combination of Solid Phase Extraction, Thermal Desorption and GC-FID", *Chromatographia*, volume 71, issues 11 - 12, pp. 1131 – 1135 (2010).

[8] Cavalcante M.R., de Andrade M.V.F., Marins R.V., Oliveira L.D.M.: "Development of a headspace-gas chromatography (HS-GC-PID-FID) method for the determination of VOCs in environmental aqueous matrices: Optimization, verification and elimination of matrix effect and VOC distribution on the

Fortaleza Coast, Brazil", *Micromechanical Journal*, volume 96, issue 2, pp. 337 – 343 (2010).

[9] Lee D.S., Jung J.K., Lim J.W., Huh J.S., Lee D.D.: "Recognition of volatile organic compounds using SnO_2 sensors array and pattern recognition analysis", *Sensors & Actuators B (Chemical)*, volume 77, issues 1-2, pp. 228 – 236 (2001).

[10] Wolfrum E.J., Meglen R.M., Peterson D., Sluiter J.: "Metal oxide sensor arrays for the detection, differentiation, and quantification of volatile organic compounds at sub-parts-per-million concentration levels", *Sensors & Actuators B (Chemical)*, volume 115, issue 1, pp. 322 – 329 (2006).

[11] Nicoletti S., Zampolli S., Elmi I., Dori L., Severi M.: "Use of different sensing materials and deposition techniques for thin-film sensors to increase sensitivity and selectivity", *IEEE Sensors Journal*, volume 3, issue 4, pp. 454 – 459 (2003).

[12] Elmi I., Zampolli S., Cardinali G.C.: "Optimization of a wafer-level process for the fabrication of highly reproducible thin-film MOX sensors", *Sensors & Actuators B (Chemical)*, volume 131, issue 2, pp. 548 – 555 (2008).

[13] Sberveglieri G., Faglia G., Groppelli S., Nelli P., Camanzi A.: "A new technique for growing large surface area SnO_2 thin film (RGTO technique)", *Semiconductor Science and Technology*, volume 5, issue 12, pp. 1231–1233 (1990).

[14] See *http://www.synspec.nl/* for details on Syntech Spectras GC855 and GC955.

CHAPTER 3

MICRO-DEVICES FOR FAST GASCHROMATOGRAPHY

3.1 – MOTIVATIONS AND CONCEPTS OF FAST-GC.

It is generally agreed that GC is one of the most widely used methods for the analysis and characterization of mixtures of volatile and semi-volatile organic compounds, and in this scenario, due to an increasing demand for higher sample throughput and lower analysis times, a great attention is focusing on the development of high-speed GC (or FAST-GC) systems.

The capability of decreasing analysis times without losing in peaks resolution, in fact, is the goal of every chromatographer, and can be achieved by properly designing the three blocks of a GC system.

In particular, the major attention must be addressed to the separation column, with the target of defining the best trade-off between its geometrical dimensions (length and inner diameter) and the features of the carrier gas flowing through it (first of all volumetric flow rate).

To do that, it is important to consider that analysis time is strictly connected to the retention times of the various compounds of the sample mixture to be analyzed, and in particular to the retention time of the last component eluted from the column t_{RL}:

$$t_{RL} = \frac{L}{u} \cdot (k+1) \qquad (3)$$

being *u* the average carrier-gas velocity, *L* the column length and *k* the retention factor for the last compound ($k = A \cdot e^{B/T_C}$, with A and B empirical constants while T_C is the column temperature).

Considering the previous formula, it seems evident that the analysis time can be significantly reduced if the column length used for an analysis is decreased and if the carrier-gas velocity is increased.

On the other hand, the use of excessively short columns and high flow-rates results in significant losses in column resolving power, since the effects of extra-column sources of peaks band broadening are amplified and the peak capacity (i.e. the number of perfectly spaced peaks that will fit in a chromatogram with a specified resolution) is reduced.

This amplifies the importance of using conditions that provide the maximum possible column efficiency, and by this purpose the choice of decreasing the inner diameter of the columns is the most promising.

The efficiency of GC columns, in fact, is expressed by the height-equivalent-to-a-theoretical-plate (H), defined as the required length of a column in which a solute molecule equilibrates between the stationary and mobile phases, while the total resolving power of a column depends on the total number of theoretical plates (N), calculated as:

$$N = \frac{L}{H} \qquad (4)$$

being L the column length.

Since the value of H is directly proportional to the inner diameter of the column (d_C), a reduction of the latter will cause the increasing of N and consequently the improvement of column resolving power.

For these reasons, MEMS-fabricated GC capillary columns based on very low inner diameter (≤ 100µm) must be preferred with respect to packed columns, since they cover wider applications and operating conditions ranges, and deliver a greater potential for speed of analysis (the only limitation of small-diameter columns is that the carrier gas volumetric flow-rate can be very low).

To summarize the previously stated concepts, in the following table the main features of conventional GC are compared with those of fast GC:

	CONVENTIONAL GC	FAST GC
COLUMN LENGTH	[10 ÷ 60] m	[2 ÷ 10] m
COLUMN DIAMETER	[150 ÷ 1000] μm	[50 ÷ 100] μm
VOLUMETRIC FLOW	[1 ÷ 6] cm^3/min	[0.1 ÷ 0.5] cm^3/min
ANALYSIS CYCLE	[10 ÷ 30] min	[1 ÷ 5] min

Tab. 4: Conventional GC vs. Fast GC.

In the subsequent sections of this chapter, two different typologies of micro-fabricated 2m-long silicon capillary column and two different typologies of micro-fabricated extremely-low-volume detectors (namely a Ultra-Low-Power (ULP)-MOX sensor and a Thermal Conductivity Detector (TCD)) suited for fast-GC applications will be presented.

3.2 – MICRO-FABRICATED SILICON CAPILLARY COLUMN.

Capillary columns generally offer a number of advantages over the packed column, including vastly improved separation capabilities with higher resolution, reduced time of analysis, smaller sample size requirements, and often higher sensitivities [1].

By this purpose, 2m-long capillary columns obtained through silicon micromachining techniques were designed and fabricated, to be employed in a miniaturized fast-GC system.

In particular, two different typologies of micro-columns were realized, on the basis of different geometrical features of channels cross-section.

Going into detail, in the first configuration the channels forming the double spiral-shaped micro-column present a *circular* cross-section with an inner diameter of 100μm, while in a second typology, the channels present a *rectangular* cross-section, whose area is 30 (width) x 300 (depth) μm^2: the latter dimensions, chosen on the basis of a theoretical study [2], ensure a sort of equivalence between 100μm-diameter circular columns and rectangular columns.

In Fig. 3.1, mask layouts of the different capillary column chips are presented: notice that, since the rectangular section is extremely unbalanced in depth-direction with respect to width, two rectangular capillary columns can be defined on a single $2x2cm^2$ chip (red and blue layouts in Fig. 3.1-a, b), while on the contrary , the geometrical

dimensions of circular cross-section allow to obtain only one circular column on a single 2x2cm^2 chip (blue layout in Fig. 3.1-d,e).

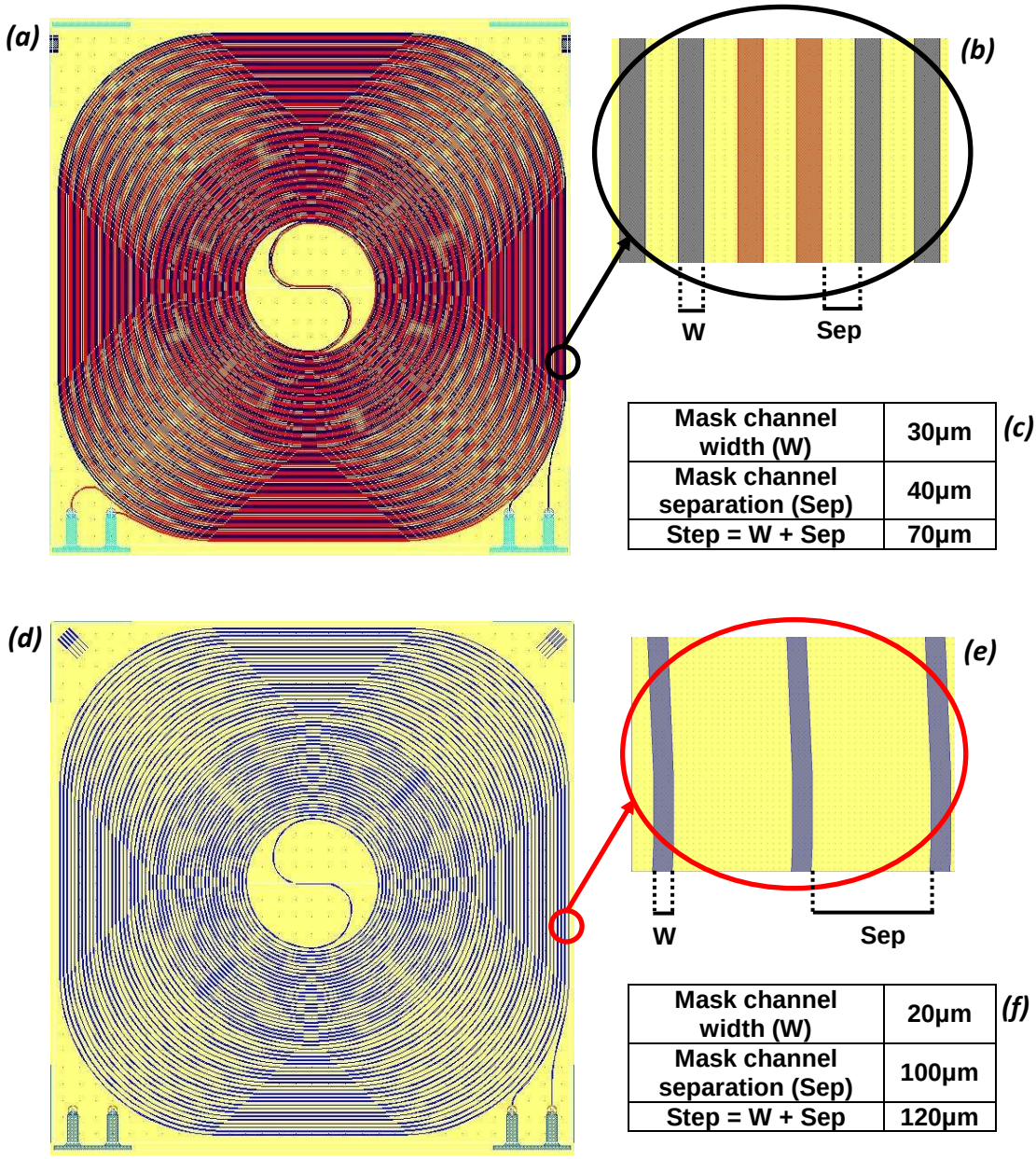

Fig. 3.1 – Mask layout of the capillary columns: rectangular column chip (a), detail of the channels (b) and geometrical dimensions (c); circular column chip (d), detail of the channels (e) and geometrical dimensions (f).

The designed capillary columns are respectively four times and two times longer than the 2.5x2.5 cm^2 and the 2.5x4.5 cm^2 packed columns presented in chapter 2, and

moreover twelve 2x2 cm^2 capillary columns chips can be contained on a 4-inches wafer (instead of the only five packed columns), as illustrated in Fig. 3.2:

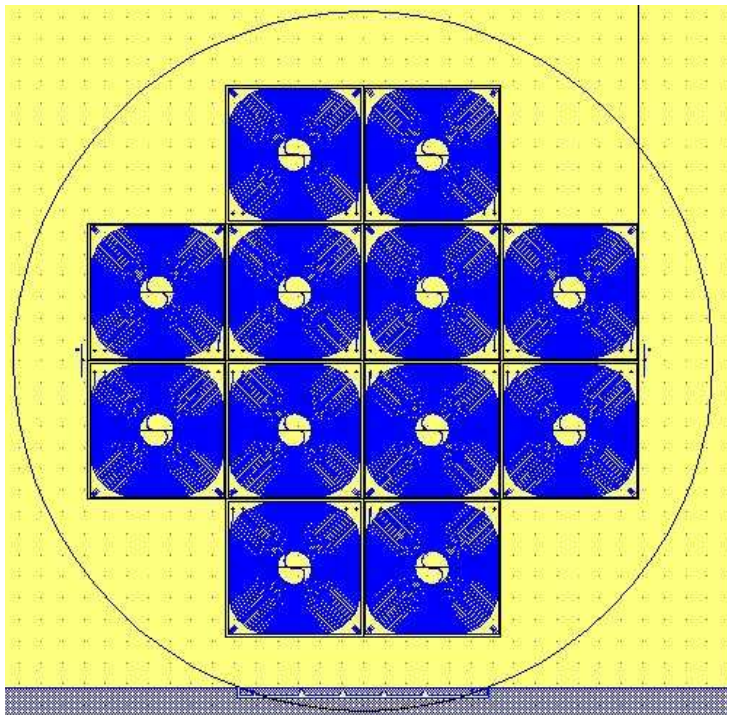

Fig. 3.2 – Capillary columns chips placement over the wafer surface (mask layout).

The technological process employed for the fabrication of the capillary column is quite similar to the one described in chapter 2 for the packed columns, except for the following steps:

a) With the aim of obtaining channels with a circular cross-section (on the contrary of the rectangular section of the packed micro-columns), the silicon D-RIE etch is performed in two subsequent steps, specifically a first anisotropic etch followed by a second isotropic etch that allows the definition of the circular structures.
b) The heating element and the temperature sensors are defined on a third silicon wafer (not on the wafer surface opposite to the channels surface), whose chips are fixed with the column chips through a conductive paste.
c) The silicon wafer containing the channels is enclosed with a second silicon wafer (on the contrary of the Pyrex wafer used for the packed micro-columns) fixed

together via fusion bonding procedure, to ensure excellent adhesion and fluidic retaining between the two wafers.

The covering wafer is micro-machined to define the inlet/outlet holes where two fused silica capillaries (the interconnections of the capillary column chip with the other blocks of the system) are introduced and sealed to silicon wafer with an appropriate glue (Pyrolin® Polymide Coating).

In particular, to favour Polymide adhesion to silicon, wafer surface was micro-machined in correspondence of in/out holes, aimed at defining circular concentric structures characterized by a high degree of roughness, obtained through D-RIE etching (etch average depth = 60µm).

Optical micrograph of the circular structures, and a picture of fused silica capillaries introduced into inlet/outlet holes and sealed with Polymide are presented in the following figure:

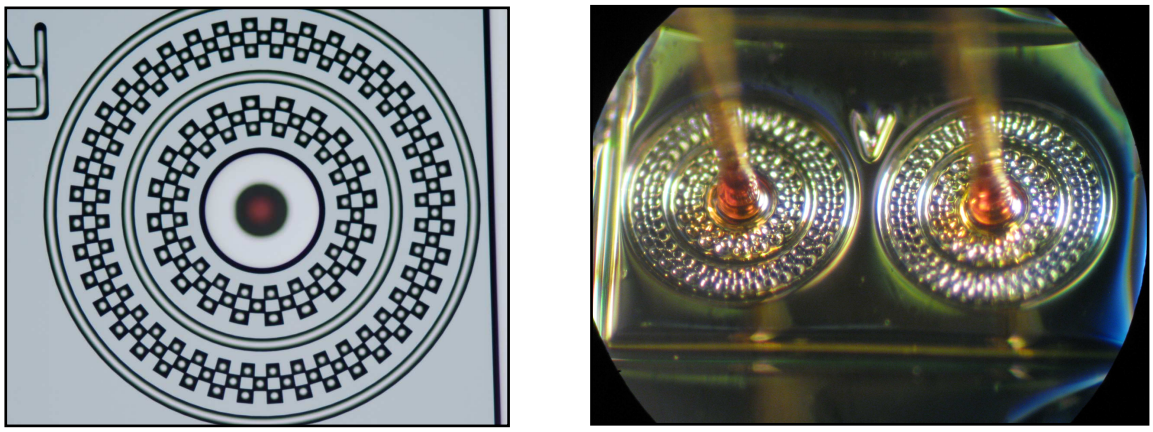

(a) *(b)*

Fig. 3.3 – Optical micrograph of the micro-machined circular geometries (a), picture of the fused silica capillaries introduced into in/out holes and sealed with Polymide (b).

while in the next figure, a picture of the whole 2x2 cm^2 chip with the fused silica in/out capillaries is presented : capillaries with outer diameter of 170µm and inner diameter of 100µm were chosen so that they can enter holes for a depth (~400µm) more than twice their diameter, increasing the mechanical robustness of the interconnection.

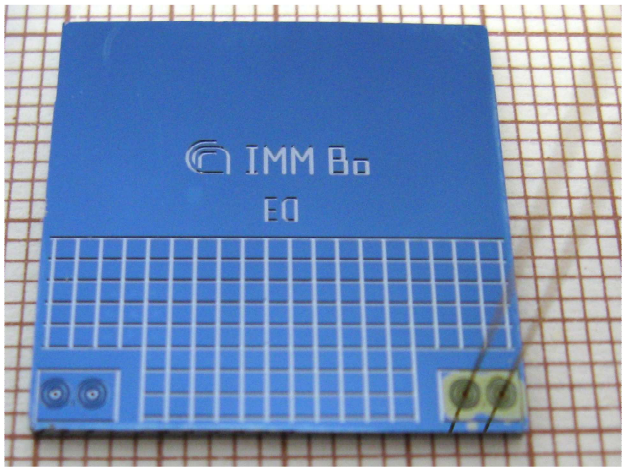

Fig. 3.4 – Picture of the column chip with fused silica capillaries.

Since the covering wafer is made of silicon, which is an opaque material (on the contrary of the transparent pyrex used for packed columns), here the column channels are not visible.

3.3 – MICRO-FABRICATED ULP-MOX SENSOR FOR FAST-GC.

In the previous chapter, the three functional blocks forming the mini-GC system developed at IMM-Bologna have been fully described, and as far as the detection block is concerned, the micro-fabricated Low-Power-Consumption Metal OXide (MOX) sensor was presented.

As far as dimensions and costs are concerned, 5 x 5mm^2 chips consisting of an array of four MOX sensors have been realized, and 106 chips were defined over a 4 in. wafer surface.

Moreover, the graph reported in Fig. 2.22 showed the correlation between device temperature and heating power, and a value of 78 mW in correspondence of the typical MOX sensor working temperature of 400°C was experimentally measured.

Aiming at decreasing costs, power consumption, but most of all dimensions (to reduce, as a consequence, dead volumes) even further, an innovative version of MOX sensor was designed and fabricated, and subsequently both electrically and functionally characterized.

Going into detail:

i) the developed Ultra-Low-Power (ULP) consumption hotplates are based on a very small circular heated area placed in the middle of a thin and narrow bridge suspended on a quite large silicon groove. This structure, obtained by releasing through a front-side silicon micromachining process a previously patterned very thin dielectric membrane, ensures an excellent thermal insulation by minimizing conductive heat transfer. The membrane consists of a stress-compensated structural stack formed by three overlapped nanometric layers, namely: thermal SiO_2, Si_3N_4 and low thermal SiO_2. The resistive heating elements and the electrodes to contact the sensitive MOX film are made by the same platinum layer and are designed to shape a circular symmetry heated area.

ii) the sensitive element is a nano-structured SnO_2 thin film, deposited over the hotplate surface using a Modified Rheotaxial Growth and Thermal Oxidation (M-RGTO) technique.

The use of a hot-plate of circular geometry allows to easily obtain a good temperature uniformity through the heated area, while the choice of platinum for the metallizations ensures a satisfactory trade-off between a quite high electrical conductivity and a fairly low thermal conductivity.

3.3.1 – Technological process and design parameters.

The process flow for the hotplates fabrication was designed in order to be a simple 2-litographic mask process (the use of a third mask is optional), thus ensuring a high yield for the over 8000 sensors per 4-inch wafer.

The following list describes the main process steps required for the fabrication of a hotplate wafer, including the relevant geometrical data, such as layer thicknesses and etch depth (see Fig. 3.5):

a) on the surface of a 4 inches <100> – single polished silicon wafer (thickness = 500μm),

b) a structural stack consisting of thermally grown SiO_2 (500nm) – deposited Si_3N_4 (300nm) – low thermal deposited SiO_2 (650nm) is obtained and subsequently

c) etched, by anisotropic ion assisted process (RIE), to expose specific regions of bulk silicon (mask 1).

d) By a selective lift-off procedure, platinum metallizations deposition was performed, defining on a single layer (thickness = 240nm) both heaters and electrodes (mask 2).

e) (optional) On the top of platinum metallizations, a silicon dioxide passivation layer (thickness = 200nm) is deposited, for electrical insulation of the sensing layer from the heater, and subsequently etched in the region of the electrical pads (mask 3).

f) Finally, the exposed silicon is selectively removed using a tetra-methyl-ammonium-hydroxide (TMAH) solution, to release the suspended structures (etch depth = 150µm).

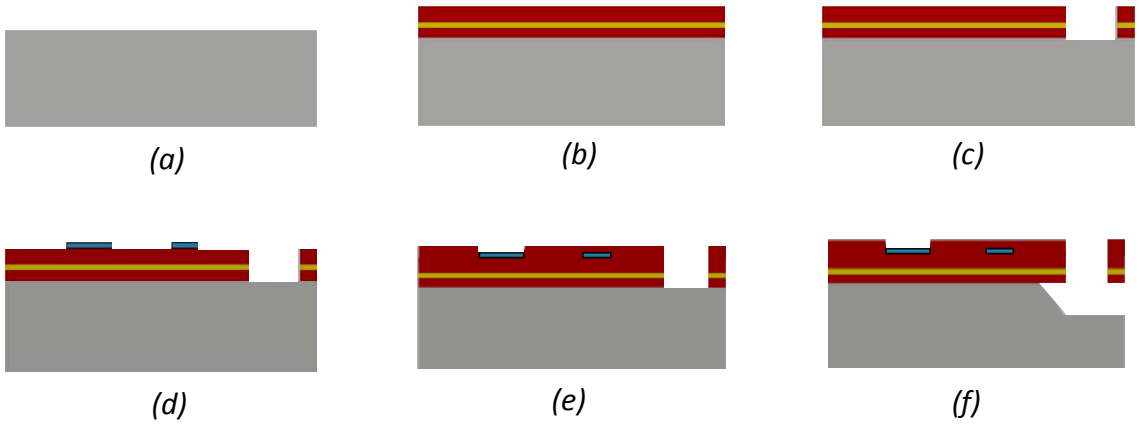

Fig. 3.5 (a - f) – Technological process for hotplate fabrication.

The next figure shows the mask layout of an array of four hotplates (yellow = dielectric stack, blue = TMAH etching regions to remove silicon underneath membranes, red = platinum metallizations, chip overall dimensions = 500 x 1500 μm^2):

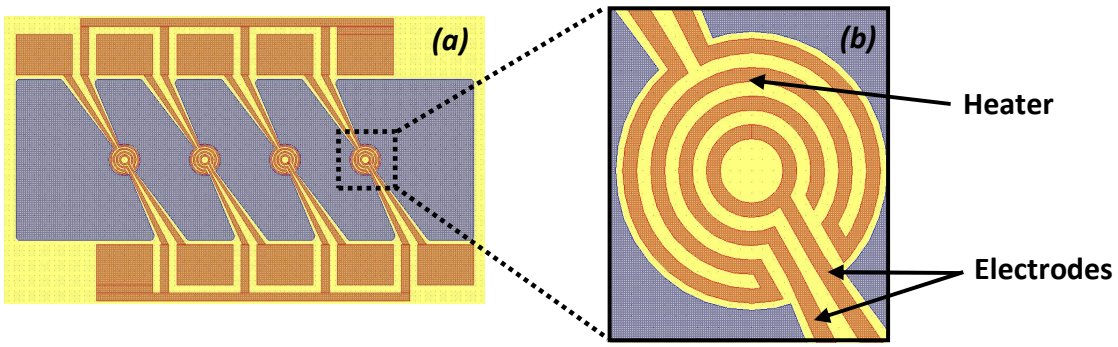

Fig. 3.6 – Mask layout of a four hotplates array (a), detail of heater and electrodes (b).

While in the following picture, SEM micrographs of the fabricated chips are presented, both in case of absence and presence of then optional passivation layer:

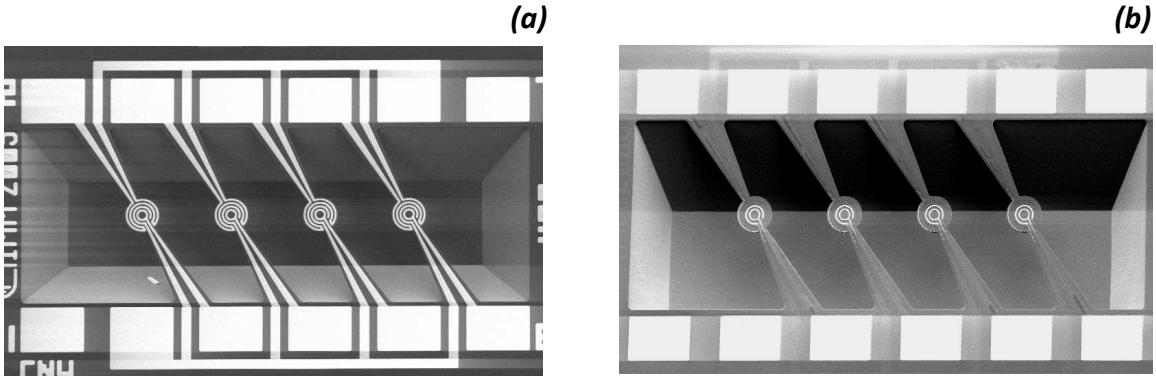

Fig. 3.7 – SEM micrographs of the micro-fabricated array: without (a) and with (b) passivation layer.

Given the great amount of disposable sensors over the wafer surface, different mask layouts were designed, in order to investigate the effects caused by variations of geometric parameters on the thermal behaviour and on the mechanical resilience of the devices.

The list of the considered parameters includes:

a) The number and the shape of the suspended dielectric arms: 2 tapered arms (NORMAL), 2 straight arms (BRIDGE), 4 tapered arms (EXTRA-ARMS).

b) The number of platinum contact electrodes: 2 (“normal” structure), 1 (“single electrode” structure), 0 (“temperature sensor”, test structure).

c) The width of the metallization tracks: 4µm vs. 6µm.

d) The size of the etch pit underneath the hotplate: 250µm vs. 400µm.

A schematic representation is given in the following figure:

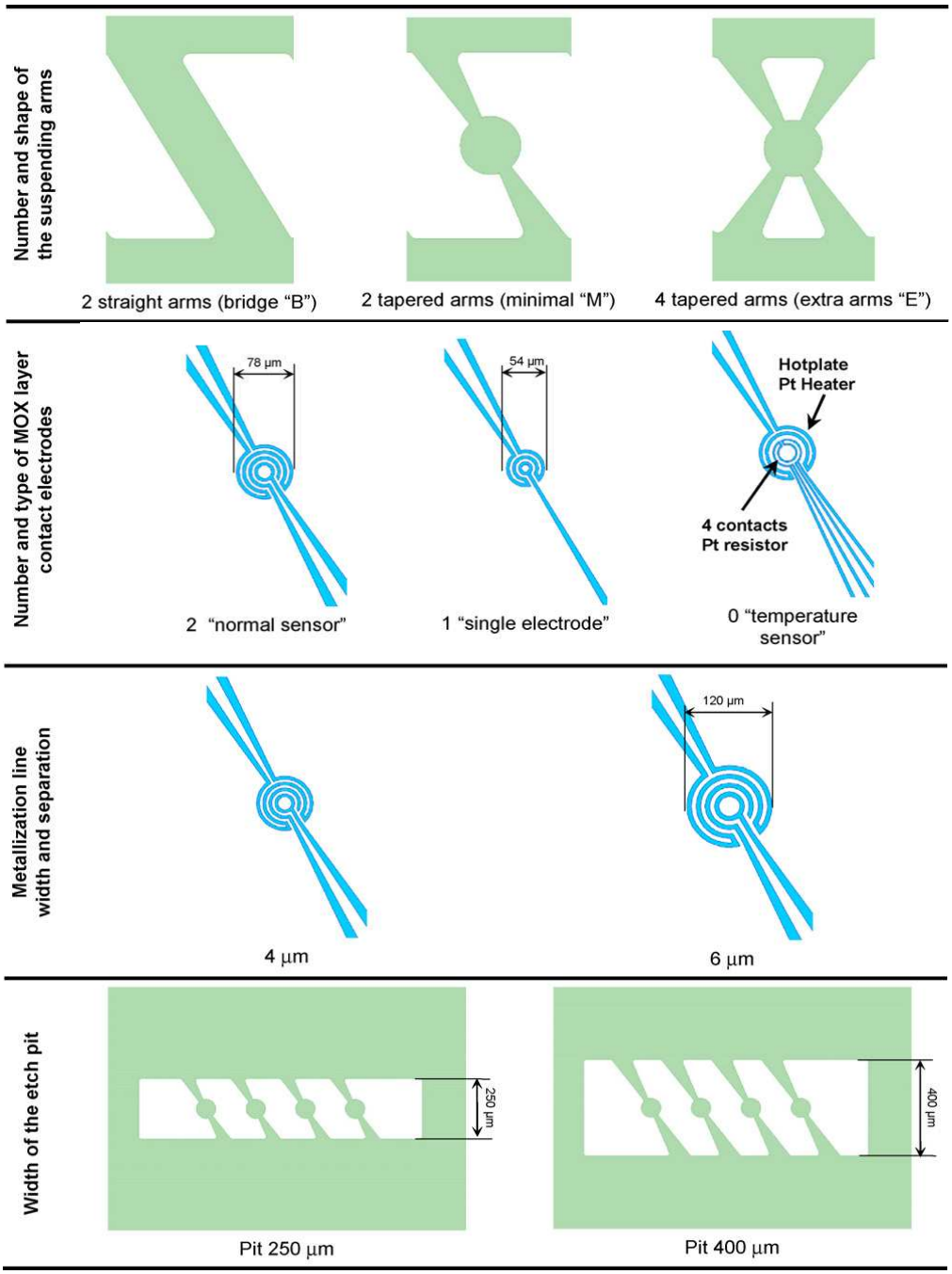

Fig. 3.8 – Different geometric parameters in hotplates design.

The configuration labelled “temperature sensor” represents a test structure where the contact electrodes were replaced by a 4-wires Kelvin resistor to directly measure the temperature over the circular active region of the hotplate as a function of electrical power consumption.

In figure 3.9, an array of two “temperature sensor” test structures is shown (arm configuration = “B”, sensor type = “0”, metallization width = 4µm, pit width = 400µm), labelling with H and T respectively the heater pads and the temperature sensor pads:

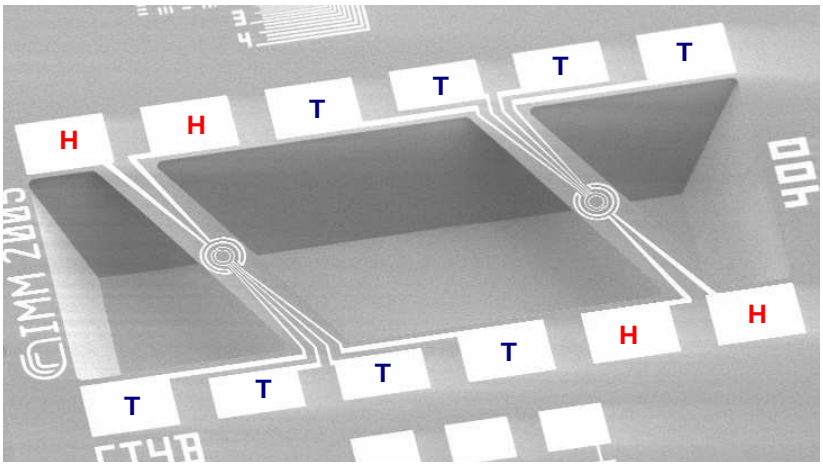

Fig. 3.9 – SEM micrograph of on array of two test structures (BRIDGE configuration).

Since, as previously mentioned, the presence of a 4-wires Kelvin resistor allows a direct measure the temperature over the circular active region of the hotplate, a precise evaluation of hotplate power consumption was experimentally achieved.

3.3.2 – Hotplates electrical characterization.

A thorough wafer-level experimental characterization of ULP hotplates was performed, starting from the precise evaluation of the Temperature Coefficient of Resistivity (TCR) of thin platinum metallizations (as already mentioned, the procedure will be discussed in chapter 4).

The adopted measurement principle is analogous to the one already described in chapter 2 (section 2.4) with the only differences that i) the linear current sweep applied

to the heater is from 0.1 mA up to 7.1 mA (still maintaining a constant step of 0.5 mA) and ii) measured TCR value was found to be 0.0031876 [1/K] ± $3 \cdot 10^{-7}$.

Temperature variation of the hotplate annular central part as a function of applied heater power was measured for devices with different configurations, in order to evaluate the effects of the different technological implementations (optional passivation) and of the different layouts.

Fig. 3.10 allows to estimate the effects of the different metallization widths W as well as the effects of the dimension of the etch pits P, while the other parameters are fixed (in particular, only the MINIMAL structure was considered).

As it can be noticed, the smaller membranes (W = 4µm) have the lowest power consumption, and the higher thermal insulation provided by the wider etch pits (P = 400µm) helps lowering the power consumption.

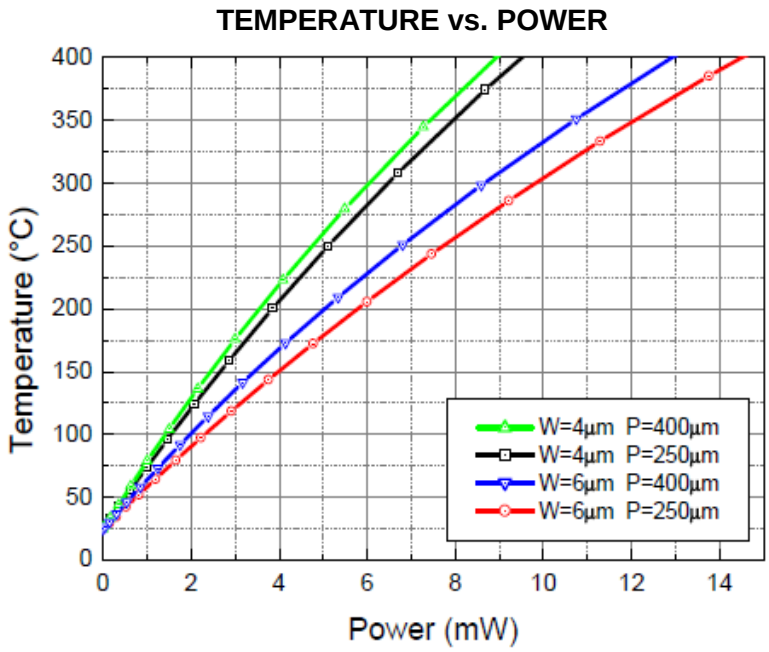

Fig. 3.10 – Plot of the hotplate temperature vs. applied power for different metallization widths W and pit widths P (No passivation layer, membrane shape = MINIMAL).

On the other hand, the effects of the membrane shape and of the metallization width W can be extracted from Fig. 3.11, while all of the other parameters are fixed.

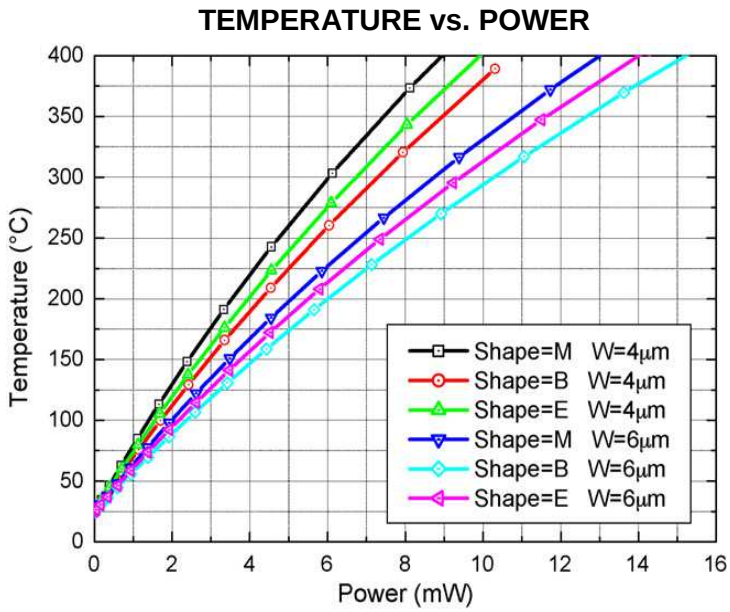

Fig. 3.11 – Plot of the hotplate temperature vs. applied power for different membrane shapes and metallizations widths W (No passivation layer, pit dimensions = 400µm).

In the previous plot, the lower power consumption of the smaller membranes is evident, but the effect of the metallization width is much more relevant.

Finally, the plot in Fig. 3.12 suggests that the effects of the presence of the passivation layer results in minimal variations of the overall power consumption:

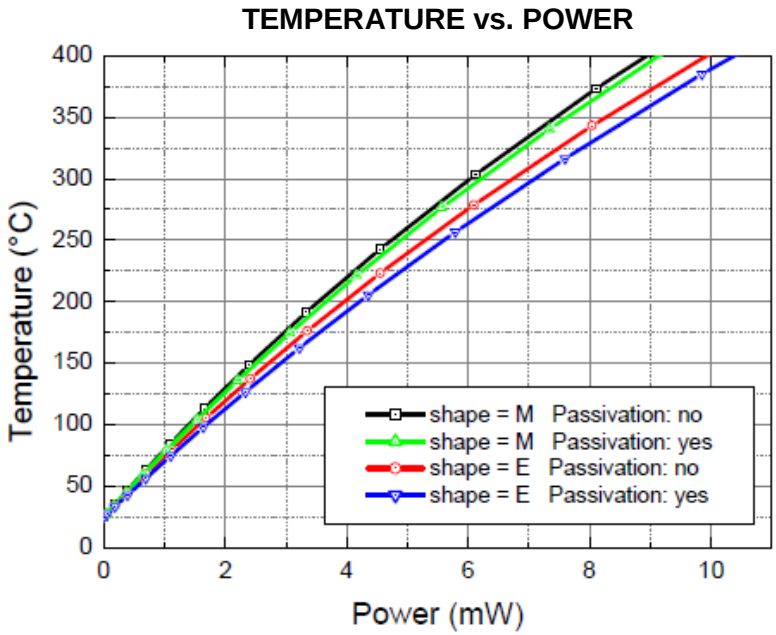

Fig. 3.12 – Plot of the hotplate temperature vs. applied power for different membrane shapes and passivation layer (W = 4µm, P = 400µm).

Results can be summarized with the following considerations:

a) The main effects on the hotplate power consumption are caused by the width of the metallizations, and hence by the overall hotplate size: this parameter is the most important one and, as expected, the smaller hotplates have a lower power consumption.
b) Another parameter which affects the overall power consumption is the width of the etch pit P: the larger the edge pit (hence the larger the distance of the hotplate from the massive silicon), the lower the power consumption.
c) The presence of a passivation layer does not critically increase the power consumption.

For these reasons, the hotplate with the lowest power consumption is the one featuring the following parameters (notice the remarkable value of only 8.9mW power consumption at the working temperature of 400°C):

PARAMETER	VALUE
Metallization width **W**	**4µm**
Etch pit dimension **P**	**400µm**
Membrane shape	**MINIMAL**
Passivation layer	**NO**
Heater Resistance @ 25℃	**134.4Ω**
Heater Resistance @ 400℃	**249.75Ω**
Heater Voltage @ 400℃	**1.49V**
Heater Current @ 400℃	**5.97mA**
HEATER POWER @ 400℃	**8.9mW**

Tab.3 – Parameters for the optimal hotplate configuration.

As far as the thermal time constant of the devices is concerned, a digital oscilloscope LeCroy 6100A was used to trace the decrease of the heater resistance (from 400°C to

room temperature) of the ULP structure reported in Fig. 3.13, by applying a small readout current of about 0.3mA.

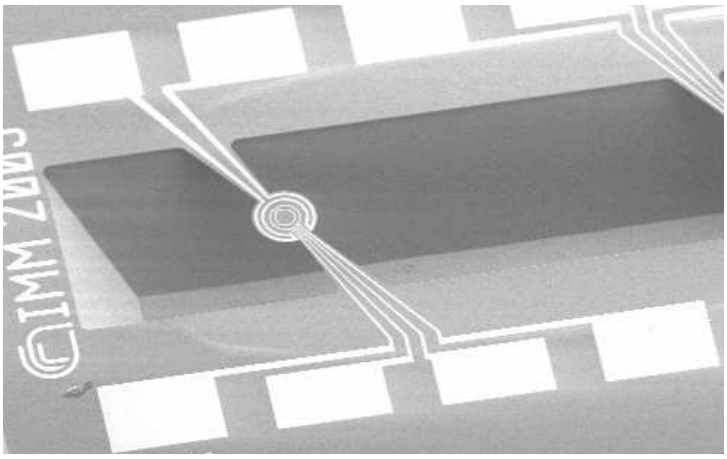

Fig. 3.13 – Measured hotplate for thermal time constant evaluation: membrane shape = M, metallizations width = 4µm, pit width = 250µm.

The decay of the heater resistance is reported in Fig. 3.14, and a very short thermal time constant of 1.5 ms resulted from the exponential fit:

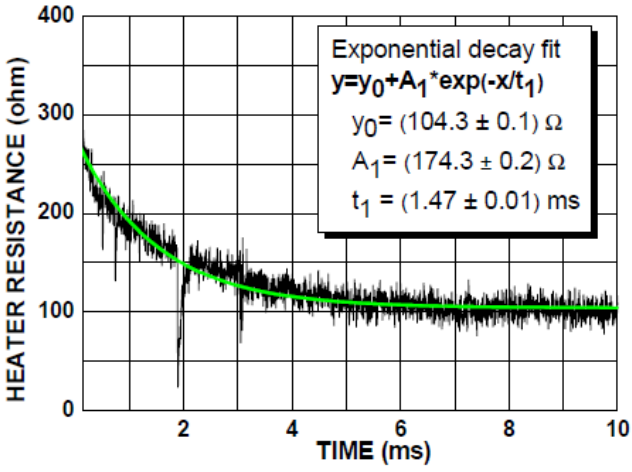

Fig. 3.14 – Heater resistance decay from 400°C to room temperature.

3.3.3 – SnO_2 sensing layer: morphology and functional characterization

As in the case of MOX sensors described in the previous chapter, sensing layer deposition has been performed by sputtering through a Modified Rheotaxial Growth and

Thermal Oxidation (M-RGTO) [3] technique, and in this case the overall sensing layer thickness at the end of the process ranges from 40 to 100nm.

The thin film morphology consists of a double layer of nano-metric SnO_2 clusters of mono-crystalline grains (shown in Fig. 3.15) with average diameters ranging from 20 to 40 nm:

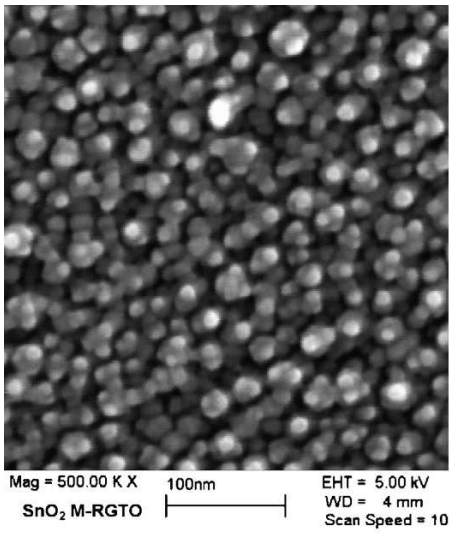

Fig. 3.15 – SEM micrograph of SnO_2 thin film nano-clusters.

these morphological characteristics, together with the small dimensional spread of the clusters, allow for the detection of gases in trace concentrations down to few ppb, with good responses even at very reduced sensing layer area as is the case of the ULP device.

On the other hand, a considerable drawback of this morphology consists in the presence of a huge number of cavities and meanders, which makes typical lithographical processes unusable for thin film patterning, since a complete removal of any photo-resist or solvent traces would result extremely difficult.

For this reason, in order to avoid sensing layer poisoning, the use of shadow masks has been chosen to define the sensing layer.

The shadow mask definition technique, as opposed to lithographic processes like lift-off or thin film etching masked by photo-resist, relies on physically masking the area where no sensing layer thin film is to be deposited by means of a shadow mask, which covers those areas and avoids the material deposition.

For this application, being the feature sizes very small and not suitable for a metallic shadow mask, an apposite silicon shadow mask micro-machined by deep reactive ion etching (D-RIE) of a 4-in. silicon wafer has been fabricated: this mask, having holes in correspondence of the hotplates etch-pits, allows to avoid sensing layer deposition on the bonding pads, as shown in the following figure for a single array of sensors:

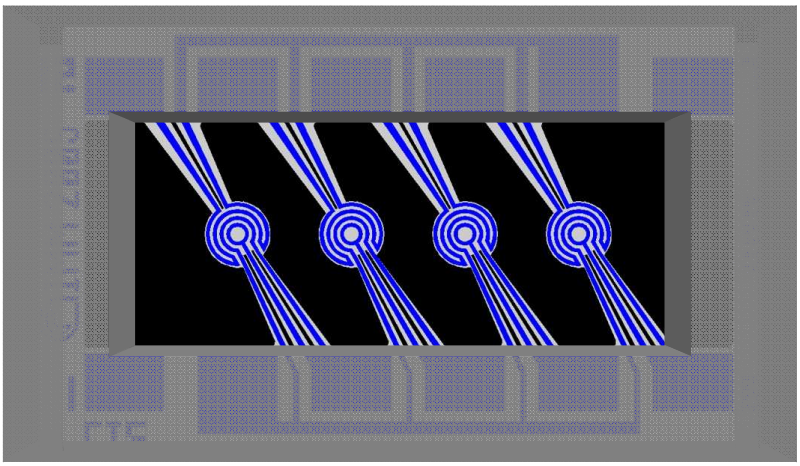

Fig. 3.16 – Silicon micro-machined shadow mask overlapped to a MOX sensor array.

The suspended structures, together with the passivation layer layout (which is mandatory in presence of the SnO_2 film) provide a self-aligning process for the sensing layer deposition on the micro-hotplate, and by means of this solution the only sensing material being read and providing the transduction signal is enclosed in the annular part of the two contact electrodes (since the whole heater and electrodes platinum arms are covered with passivation layer, as already shown in Fig. 3.7-b).

This self-aligned sensing layer has an open circular ring shape with width corresponding to the distance between the sensing electrodes (4 or 6μm, depending on the device) and circumference lengths of 120 or 270μm.

An example is reported in the following figure, showing a SEM micrograph of a ULP MOX sensor central hot spot (with passivation), where the effective thin film providing the transduction signal is highlighted in red:

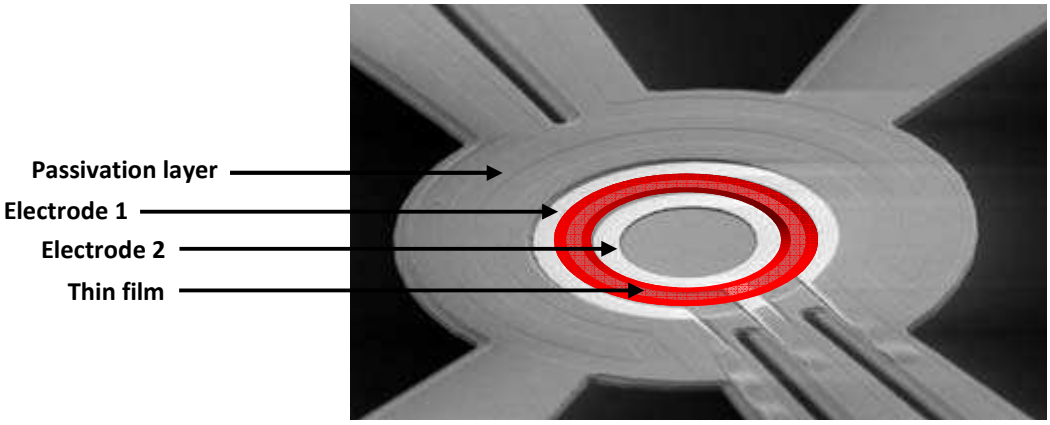

Fig. 3.17 – SEM micrograph of a passivated ULP MOX sensor: the region highlighted in red represents the effective thin film.

On the top of the SnO_2 layer, nano-metric gold particles (shown in Fig. 3.18) with a quite uniform spatial distribution act as a catalyst for the reaction of the VOCs (the average presence of gold has been evaluated to be approximately 10 wt.%).

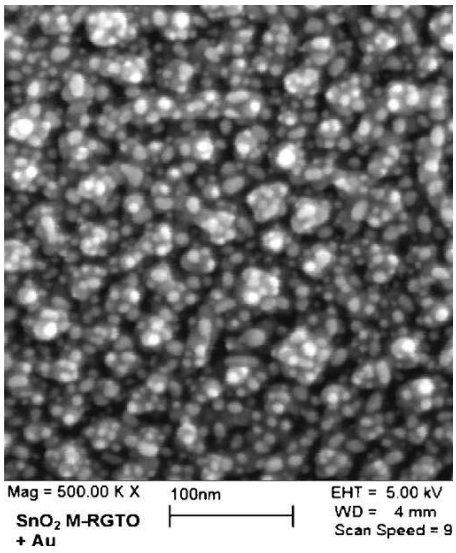

Fig. 3.18 – SEM micrograph of SnO_2 film with gold nano-particles.

The uniformity of the sensing layer deposition process has been evaluated at wafer level, acquiring the conductance of 28 identical ULP sensor sensing layers uniformly distributed on a wafer surface, when heated at a temperature of about 400°C.

Values of electrical conductance from 1 to 5µS with a mean value of (2.6±0.9)µS were achieved, measuring the samples in lab air, where local changes in the atmosphere

composition may have caused variations on the sensing film electrical conductance, which is expected to be more reproducible under controlled conditions.

3.3.4 – ULP-MOX sensor performances.

Preliminary tests were performed to investigate ULP-MOX sensor performances, and in particular to estimate its sensitivity towards VOCs.

To this purpose, some of the sensor arrays have been wire-bonded over a TO-8 case and measured in a stainless steel cylindrical test chamber (similar to the one employed in the mini-GC system for laboratory tests) having an internal volume of 0.5cm^3, according to the assembly scheme presented in the following figure:

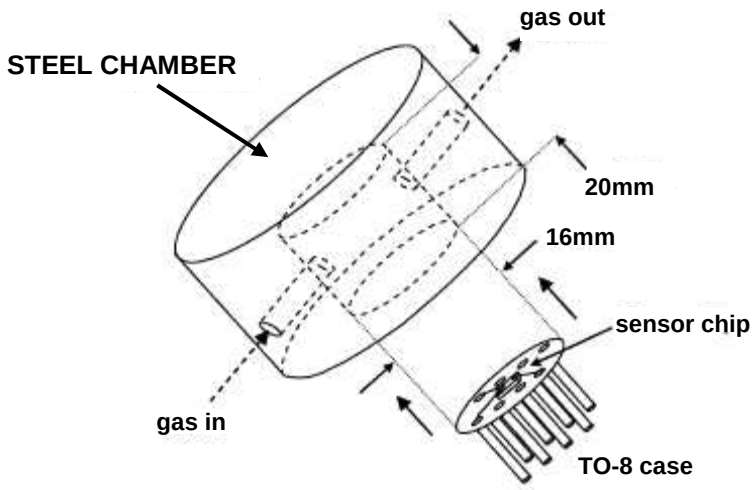

Fig. 3.19 – Chamber assembly with micro-machined sensor chip bonded on a TO8 case.

The steel chamber, whose gas inlet and outlet are small holes located along the longitudinal axis in the centre of the structure along a radial direction in the middle of the lateral surface, was connected to a gas distribution system capable to generate high precision gas concentration mixtures (by adding a predetermined quantity of target gases to a flow of synthetic air).

To estimate the sensitivity towards VOCs, sensor responses towards different concentrations of benzene (C_6H_6), one of the most harmful VOCs in outdoor and indoor polluted air, have been acquired: in particular, measurements were performed under dynamic conditions, at a constant flow of 30 sccm with relative humidity equal to 30% at

22°C, and at sensor operating temperature of 415°C (corresponding to a power consumption of 9mW).

Moreover, to investigate MOX selectivity, the responses towards other interfering gases have been measured as well: in particular, among the most important air pollution tracers, carbon monoxide (CO) has been chosen as representative interferent.

Results were plotted in the graph of Fig. 3.20, where the y-axis reports the value of the current flowing through the MOX sensing biased at 1 V.

It is interesting to point out that similar responses towards C_6H_6 and CO provided by ULP-MOX sensors are relative to 5ppb and 10ppm, respectively.

The fact that benzene and CO sensor responses are comparable, despite benzene concentrations are about 2000 times lower than the CO concentrations, is the evidence of MOX sensor high selectivity towards VOCs.

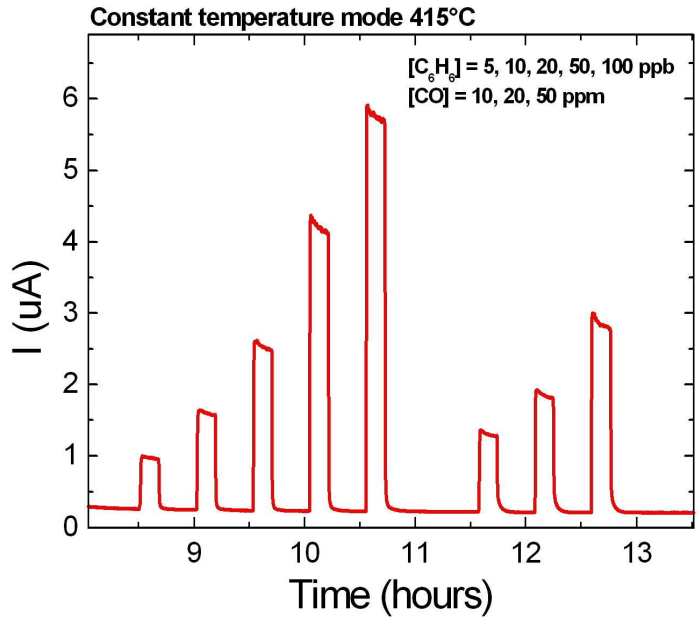

Fig. 3.20 – ULP-MOX sensors response to increasing concentrations of benzene and CO.

3.3.5 – ULP-MOX sensor encapsulation.

As reported in Table 4, fast-GC systems are based on very low inner diameter (<100 μm) capillary columns with extremely low volumetric fluxes (~ 0.5sccm).

For these reasons, detectors acquiring the GC peaks must operate in ultra-low-volume chambers to avoid peak broadening and reduce dead volumes as much as possible (as an example, commercial detectors used in portable GC-systems are designed to have internal volumes of less than 1µL).

The adopted solution to let our micro-fabricated ULP-MOX sensors satisfy this constraint consisted in their encapsulation with a mechanically micro-machined pyrex wafer implementing ultra-low-volume micro-chambers with square cross-section (section area = 250x250 μm^2, inner volume < 0.1µL), which also protect the structures during the dicing process for chips separation.

The cross section of the overall structure is presented in Fig. 3.21:

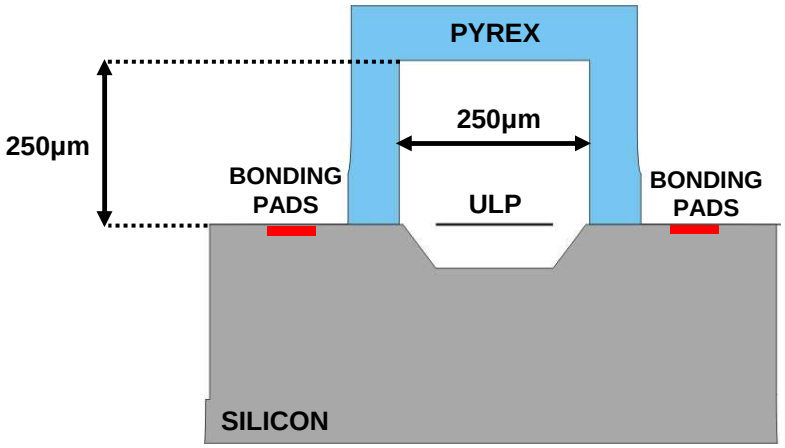

Fig. 3.21 – Cross section of the silicon chip with the integrated pyrex micro-chamber.

To investigate the behaviour of the detectors surrounded by a gas flow inside the micro-chamber, preliminary simulations (whose details are presented in chapter 4) were performed on ULP-MOX sensors, implementing the electro-thermal model with a micro-fluidic part governed by the Navier-Stokes equations:

$$\begin{cases} \dfrac{\partial u_i}{\partial x_i} = 0 & (7) \\ \rho \cdot u_j \cdot \dfrac{\partial u_i}{\partial x_j} + \dfrac{\partial p}{\partial x_i} = \mu \dfrac{\partial^2 x_i}{\partial u_i \partial u_j} & (8) \end{cases}$$

where u = fluid velocity [m/s], ρ = fluid density [Kg/m^3], p = fluid pressure [Pa] and μ = fluid dynamic viscosity [Pa·s].

The previously described technological process for ULP-MOX fabrication (section 3.3.1) must be therefore implemented with the following steps, (described also visually) where, for the sake of simplicity, a single chip was considered to represent the whole wafer:

a) a 500μm-thick pyrex wafer

b) is mechanically micro-machined with a dicing saw, to form the channel and to release the regions of the bonding pads.

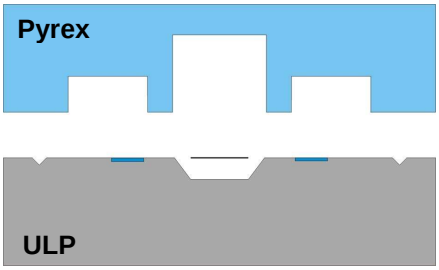

c) The micro-machined silicon and pyrex wafers are fixed together via anodic bonding procedure.

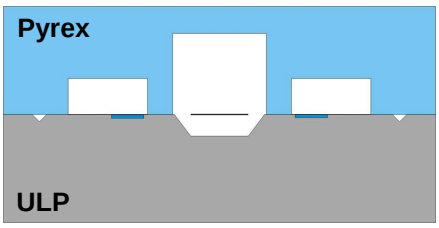

d) Through the dicing saw, pyrex wafer is micro-machined to remove the remaining glass over the bonding pads.

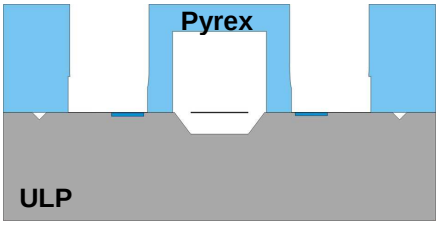

e) Subsequently, pyrex wafer micro-machining is full-finished and the chips can be finally separated.

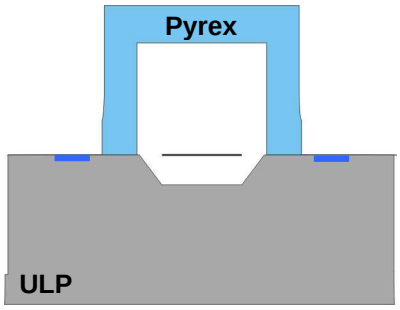

Next figure shows an example of a silicon chip containing a ULP-MOX array with the integrated pyrex micro-chamber:

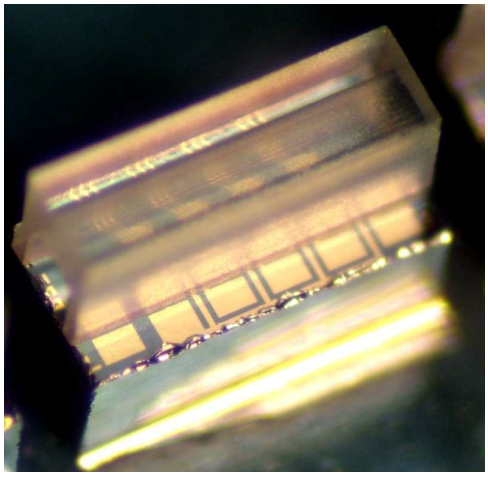

Fig. 3.22 – Picture of a ULP-MOX array with integrated pyrex micro-chambers.

The characterization of the encapsulated ULP MOX sensor used as fast-GC detector is ongoing and preliminary results will be presented in future works.

3.4 – MICRO-FABRICATED TCD FOR FAST-GC.

In chapter 2 (section 2.4) and in the previous section of this chapter, the design of a Metal OXide sensor based on a chemo-resistive working principle was described, focusing the attention on its great sensitivity and selectivity towards aromatic Volatile Organic Compounds. For this reason, MOX sensors has been considered and thoroughly employed in the development of the previously described GC systems specifically targeted to BTEX analysis.

Nevertheless, if the interest of the analysis is pointed not only to VOCs, but to a wider range of compounds, MOX sensors are not generally taken into account, since they show little or even no response to several compounds potentially of interest (eg. CO_2 and N_2).
For "general purpose" applications, Thermal Conductivity Detector (TCD) represents a more appropriate choice [4,5,6], since it is capable of responding to all the components of a gas sample: on the other hand, the price to pay for the "universality" of TCD is represented by a decrease in sensitivity and a lowering of the minimum detectable level (i.e. the concentration of solute that generates a peak signal corresponding to a Signal-to-Noise ratio of 2) with respect to MOX sensors.

3.4.1 – TCD working principle.

The TCD is identified as a physical detector, since it responds to some difference in the thermal conductivity (a physical property) of a "carrier gas" caused by the presence of the eluted components.
The most common example of TCD is represented by a wire filament heated by the electrical current flowing through it: using a wire with a temperature dependent resistance, the temperature of the wire can be measured according to the well known relation:

$$R(T) = R_0 \cdot (1 + TCR \cdot T) \qquad (5)$$

being TCR the temperature coefficient of resistance for the wire filament and R_0 the resistance at the reference temperature of 0°C.
If the filament is surrounded by a reference gas, small changes in gas thermal conductivity due to the presence of sample components (different from the reference gas) cause variations in temperature T, that can be detected by the change in wire filament resistance.
The TCD is commonly operated using helium or hydrogen as the carrier gas, since the thermal conductivity of these gases (respectively 0.142 W/m·K and 0.160 W/m·K @ 298K) is higher than that of all the typical solutes.
The previously described working principle of the TCD is clearly suitable for implementing a differential measurement scheme: the presence of the sample

component, in fact, can be better revealed by comparing the thermal conductivity of the pure carrier gas with the thermal conductivity of the mixture represented by the carrier gas in addition with the analyte.

A typical arrangement for a TCD is represented by two filaments put within a Wheatstone bridge configuration, as illustrated in the following figure:

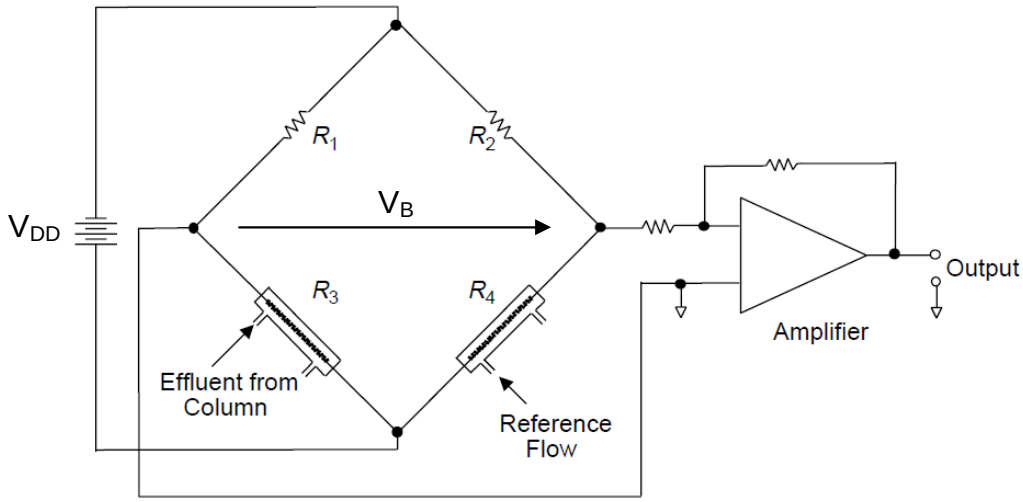

Fig. 3.23 – Wheatstone bridge circuitry for a two-flow cell TCD [2].

The pure carrier gas (reference) flow enters resistor R_4, while the flow from analytical column (carrier gas + eluted sample component) enters resistor R_3.

The four resistor are designed such that, in absence of sample eluted from the column, the Wheatstone bridge results balanced, that is:

$$R_1 \cdot R_4 = R_2 \cdot R_3 \qquad (6)$$

and, as a consequence, $V_B = 0V$.

As a substance elutes from the column and enters R_3 (together with the carrier gas), thermal conductivity of the analytical flow differs from thermal conductivity of the carrier gas that enters R_4; for this reason, temperature of R_3 differs from temperature of R_4 and , from eq. 5, $R_3 \neq R_4$.

Hence, eq. 6 is not verified and, as a consequence, a nonzero voltage measurement is obtained ($V_B \neq 0V$), revealing the presence of the sample substance.

As illustrated in the previous figure, since the detection signal V_B is expected to have a quite low value, a high-signal-to-noise-ratio instrumentation amplifier is generally placed downstream of the bridge.

Fig. 3.24 shows another configuration of the bridge circuit, which replaces resistors R_1 and R_2 with two more filament flow cells.

Cells R_1 and R_4 each contain the reference gas, while in cells R_2 and R_3 the analyte column effluent flows.

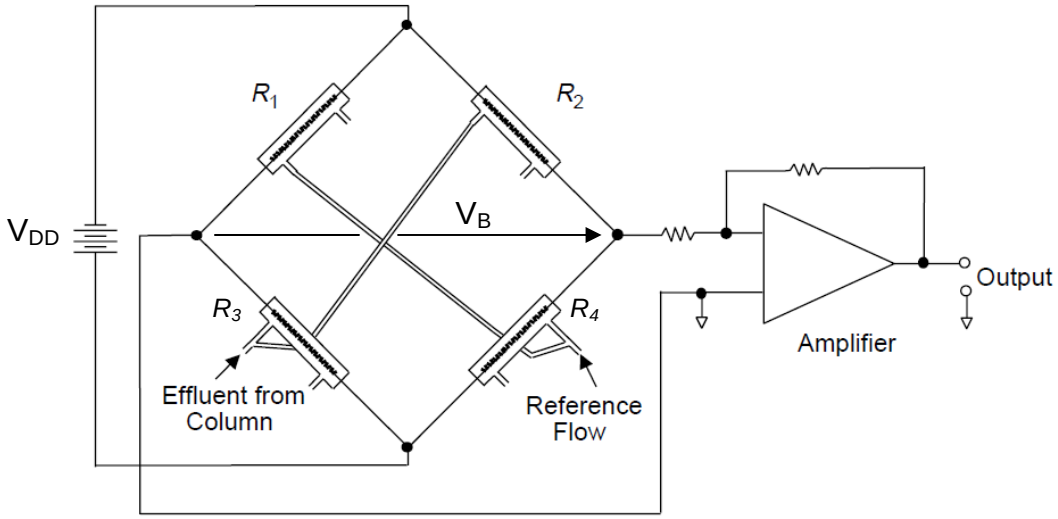

Fig. 3.24 – Wheatstone bridge circuitry for a four-flow cell TCD [2].

The working principle is the same described for the configuration of Fig. 3.23, but in this new design the response factor (or, in last analysis, the sensitivity) is increased by a factor of 2, since two filaments (not only one) are contributing to the change in signal V_B.

The latter is the design solution adopted for our micro-fabricated TCD, which is formed by four nominally equal platinum resistances defined on the surface of suspended dielectric membranes, as explained in next section.

3.4.2 – TCD technological process and design layout.

The technological process employed for the fabrication of the thermal conductivity detector follows the one described in this chapter for the ULP-MOX sensor, except for

platinum electrodes definition and for passivation layer deposition (both unnecessary, since the SnO_2 sensing thin film is not required for TCD).

Figure 3.25 shows mask layout (with geometrical dimensions) and an optical micrograph of one of the six designed configurations for the resistors forming the Wheatstone bridge (yellow = dielectric membrane, green = D-RIE etched regions underneath membrane, red = platinum heater)

Notice the holes designed over the membrane surface, they were introduced to permit an efficient removal of the underneath silicon during the fabrication using an anisotropic etching, and to promote heat exchange with the flowing gas when the device is operated.

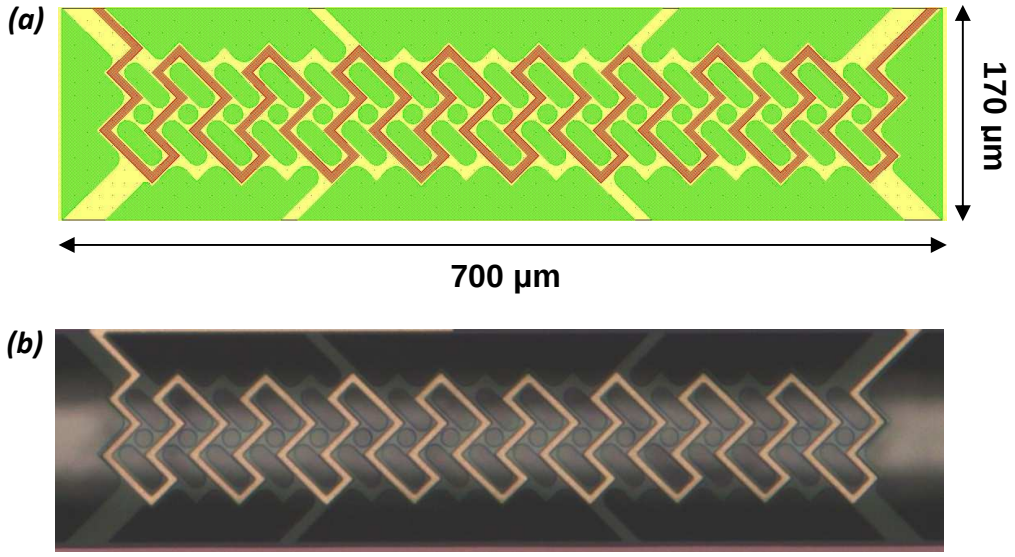

Fig. 3.25 – Example of mask layout (a) and optical micrograph (b) for the single resistor of the Wheatstone bridge.

Every chip contains the four resistors of the bridge. Its overall dimensions are 5mm x 5mm, to favorite the setup of fluidics interconnections and chip handling, since the surface effectively employed by the resistors is much smaller.

Figure 3.26 shows a chip mask layout, where reference branch (formed by structures A and B) and analytical branch (formed by structures C and D) are visible and where the pads that have to be externally bonded to form the Wheatstone bridge configuration are

identified with a corresponding number (1 = bridge negative supply, 2 = bridge negative measurement, 3 = bridge positive measurement, 4 = bridge positive supply).

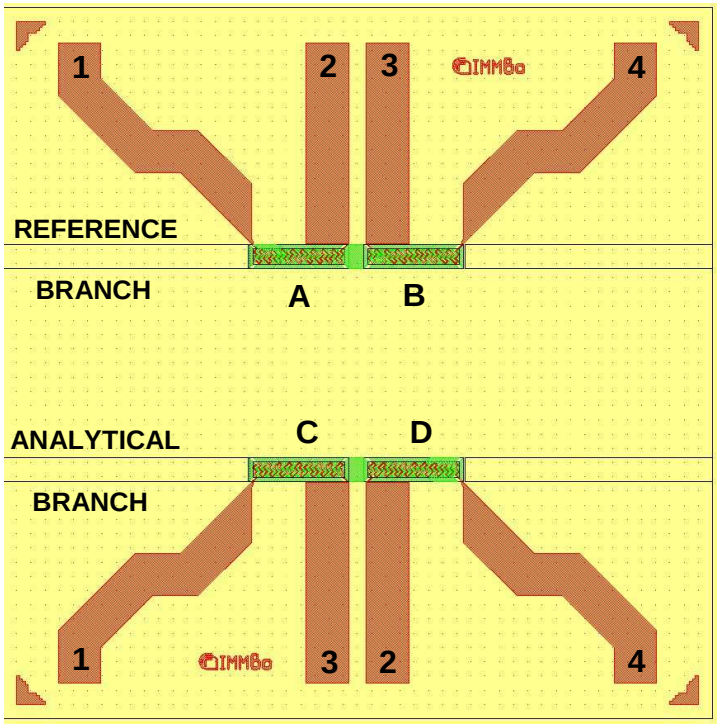

Fig. 3.26 – Mask layout of TCD chip.

In a 4-inches wafer, a quite large number (specifically, 216) of 5x5mm^2 chips can be fabricated and, for this reason, six layouts with different geometrical features of resistors were designed.

As an instance, the following figure shows an optical micrograph of a different configuration where two platinum resistors (not only one) are defined over a single suspended membrane, thus each channel is formed by only one structure

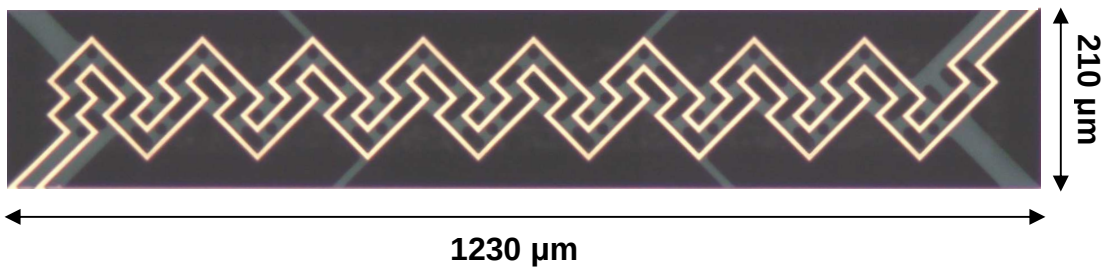

Fig. 3.27 – Optical micrograph of the double resistor over the single membrane.

In the latter configuration, resistors are very close each other, so it can be assumed that, in each branch, they are subjected to the same gas flow at the same time; on the contrary, in the configuration reported in Fig. 3.26, resistor B is subjected to the same flow of resistors A, but in two subsequent times, and the same assumption can be stated for resistors C and D.

3.4.3 – Integrated pyrex micro-chamber.

The adopted solution to let our micro-fabricated TCDs satisfy the constraints reported in Tab. 4 replies the one previously described for ULP-MOX sensor, i.e. their encapsulation with a mechanically micro-machined pyrex wafer implementing ultra-low-volume micro-chambers (inner volume of 0.1µL) that form the reference and the analytical channels
The cross section of the designed structure is presented in Fig. 3.28.

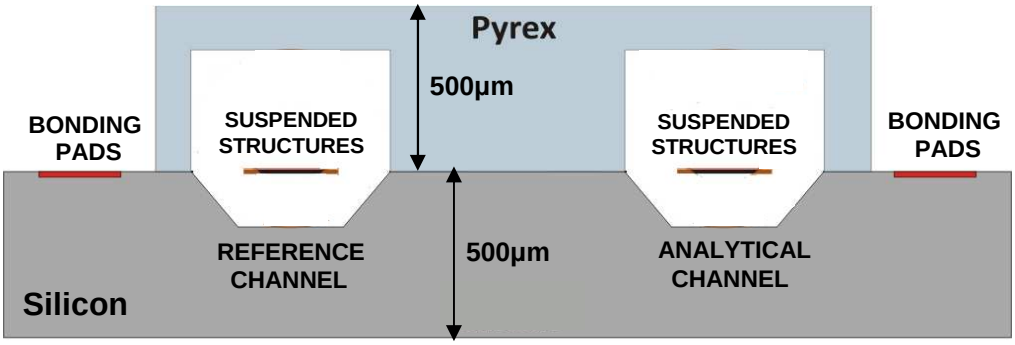

Fig. 3.28 – Cross section of the TCD chip with the integrated pyrex micro-chamber.

While next figures provide a visual schematization of micro-machining procedures adopted for reference and analytical channels fabrication and for micro-TCD encapsulation (for the sake of simplicity, two chips were considered to represent the whole wafer):

(a)

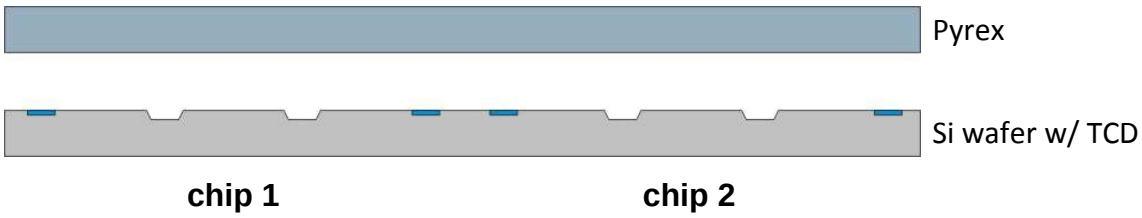

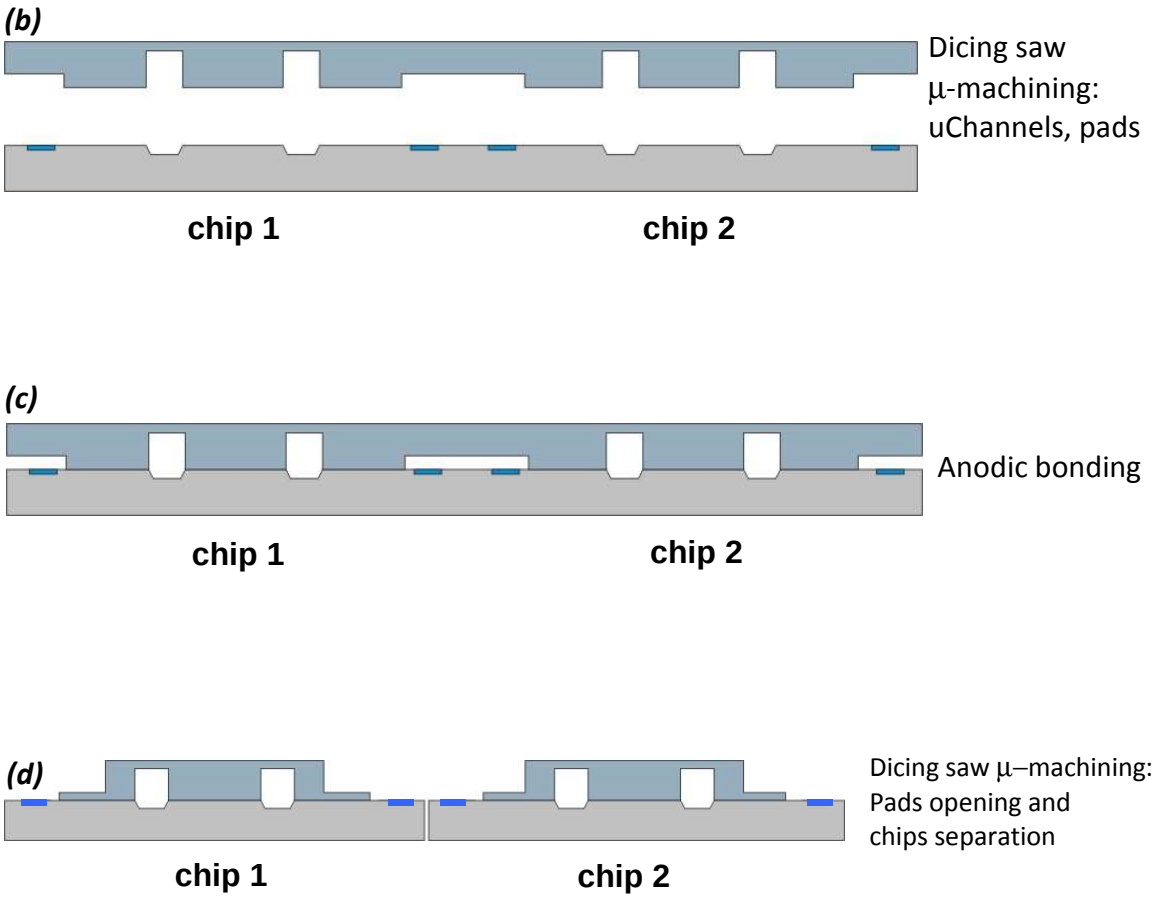

Fig. 3.29 (a-d) – Pyrex micro-chambers integration on TCD silicon wafer.

By this purpose, next figure shows: a) an example of TCD silicon chip with integrated pyrex micro-chambers, b) a detail of channels inlets where two fused silica capillaries can be inserted, to interconnect the TCD with the micro-columns, c) the TCD chip and its four fused silica capillaries (2 inlet/2 outlet) wire-bonded over a TO8 case.

The fabricated wafers showed a very good yield (~ 90%) both for pyrex micro-chambers integrity and platinum metallizations definition, also after chips separation due to dicing saw micromachining procedure.

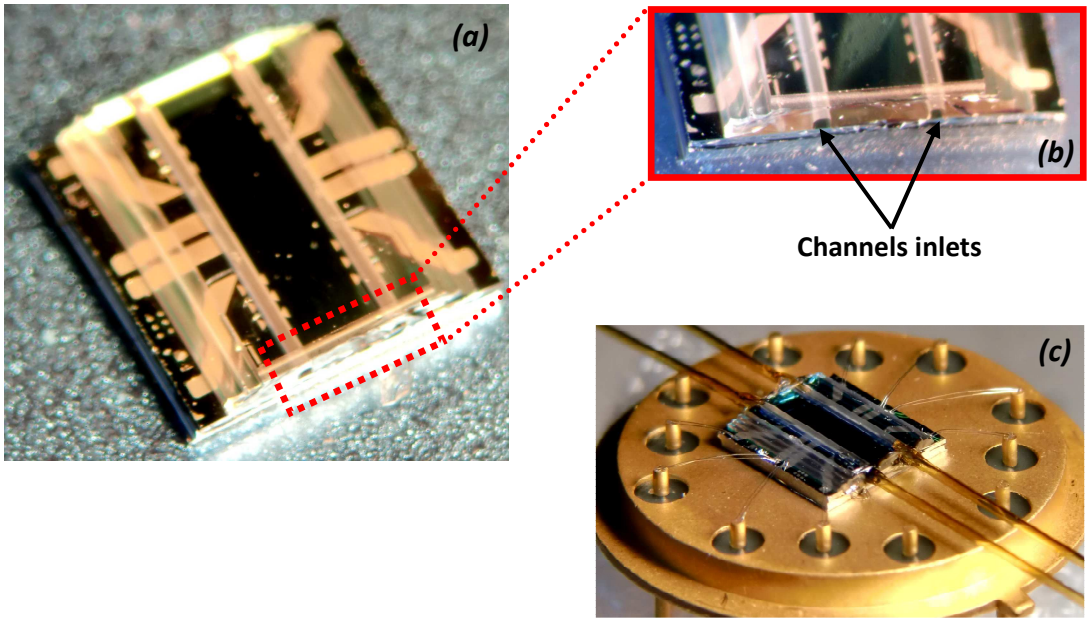

Fig. 3.30 – Picture of a TCD chip with pyrex micro-chambers (a), detail of channels inlets (b) and chip with fused silica capillaries bonded over a TO8 case (c).

3.5 – EXPERIMENTAL RESULTS.

In this section, preliminary experimental results obtained from capillary columns, ULP-MOX and TCD characterization are reported:

3.5.1 – Capillary columns characterization.

Prior to stationary phase introduction into the capillary columns, single chips were subjected to specific tests aimed at evaluating their robustness with respect to thermal and mechanical stresses.

Fluidic interconnections, in fact, are made by introducing one end of 30cm-long fused silica capillaries into column inlet and outlet and sealing them with Polymide: since the sealing procedure takes place when, at high temperatures, Polymide forms polymers, chips were placed into a oven and subjected to a curing processing (from 25 to 200°C with a temperature ramp of 5°C/min, followed by ten minutes at 200°C).

After heat treatment, to increase the whole mechanical stiffness of the structure, a bi-component glue (specifically Torr Seal) was applied to the polymide and mechanical robustness was tested through capillary bending by means of a bar (see Fig. 3.31).

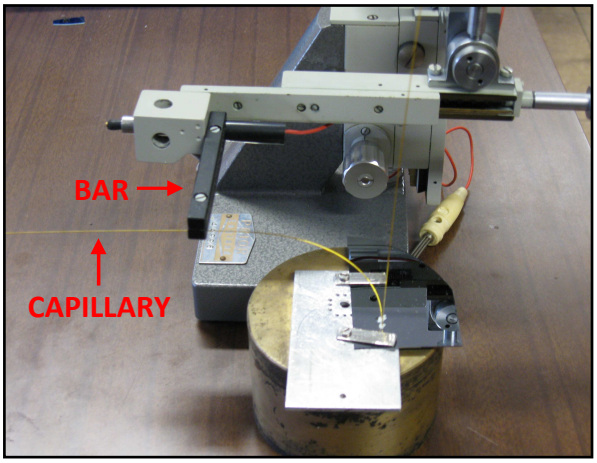

Fig. 3.31 – Experimental setup for mechanical robustness test.

Finally, chips have been subjected to test performed at room temperature for verifying column fluidic retaining.

To this purpose, column inlet capillary has been connected to a laboratory pipeline supplying nitrogen, while the micro-column has been plunged into a beaker filled with de-ionized water (see Fig. 3.32):

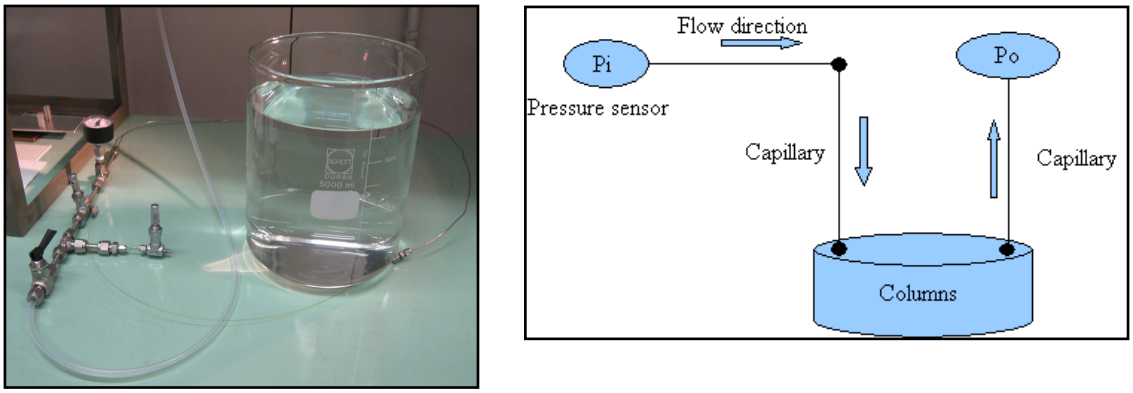

Fig. 3.32 – Experimental setup (left) and schematic representation (right) for fluidic retaining test.

By means of a pressure sensor and a relief valve, nitrogen flow entered inlet capillary at different pressure values (from ambient pressure to a maximum of 7bar, constantly keeping outlet capillary at ambient pressure), allowing to check for the presence of any bubbles in the beaker, index of column fluidic leakage.

About 70% of tested devices provided a successful response to thermal, mechanical and pressure stresses, and few of them were subsequently delivered to MEGA s.n.c. (Legnano(Mi), Italy), for stationary phase introduction and preliminary chromatographic analysis.

Phase deposition has been performed with the procedures usually adopted for fused silica capillary columns, where the phase is introduced as a thin film coating the internal walls of column channels.

Successively, preliminary chromatographic analysis were made, principally focusing on VOCs mixtures: as an instance, following figure shows a chromatogram of VOCs mixture (benzene, toluene, ethyl-benzene, xylene) obtained by means of a capillary column.

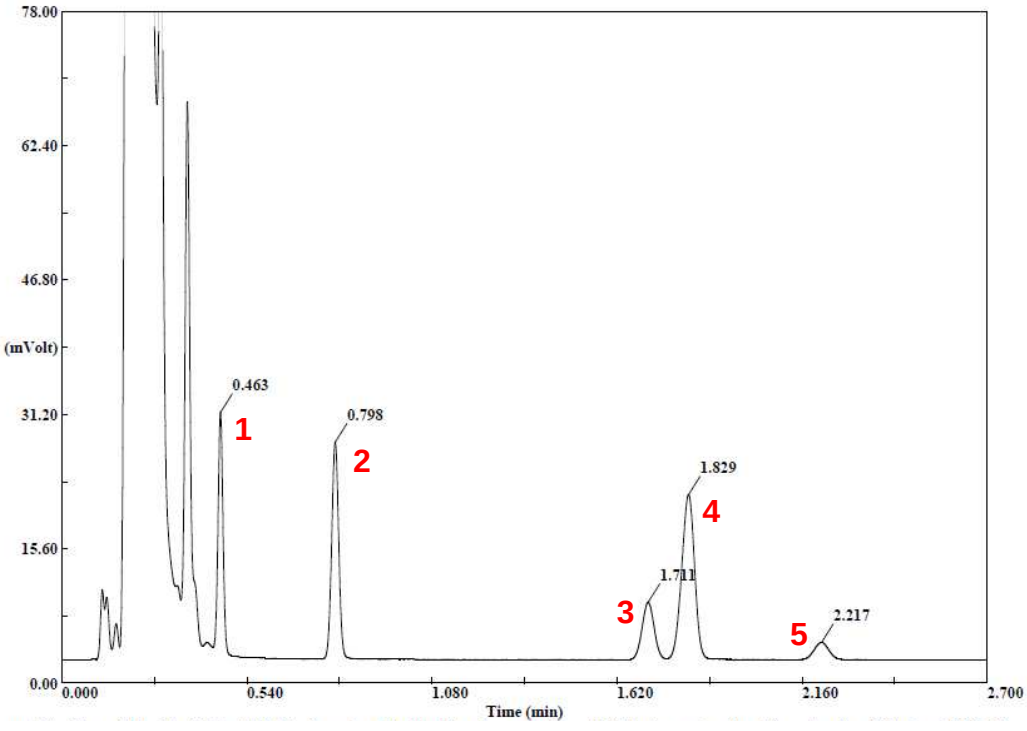

Fig. 3.33 – Chromatogram of a BTEX mixture in Helium: Benzene (1), Toluene (2), Ethyl-benzene (3) and Xylene-isomers (4,5).

Micro-column under test has been maintained at isothermal condition (50°C), using Helium as mobile phase, 5% fenyl – 95% Metyl-PolySiloxane (MPS) as stationary phase and a Flame Ionization Detector (FID) as sensitive element.
Experimental results show a very good peaks resolution and, most of all, the capability to perform the analysis cycle in a little more than two minutes.

3.5.2 – ULP-MOX sensor characterization.

Given the extremely reduced dimensions of pyrex micro-chamber cross-section, ULP-MOX (but the same goes for TCD) interconnections with separation column must be performed via fused silica capillaries (already presented in Figs. 3.3 and 3.4).
To investigate ULP-MOX sensor reaction to a specific flux entering the micro-chamber through the inlet capillary, an array of sensors with integrated pyrex chamber was subjected to nitrogen fluxes characterized by different volumetric flow rates to evaluate, at fixed working temperature, variations of power consumption due to increasing flow rates.
Experimental results are presented in the following chapter (section 4.5.2, Fig. 4.22) where they are compared with simulation results.

3.5.3 – TCD characterization.

To investigate the sensitivity of micro-fabricated TCD with respect to changes in gas carrier composition, an experimental set up was prepared in order to characterize the TCD reported in Fig. 3.26 when two different carrier gases (Nitrogen and Helium) are injected into the miniaturized chamber.
The experimental setup is presented in Fig. 3.34: one of the capillaries (fused silica tubes with inner diameter = 100μm) is the carrier gas inlet of the TCD, and is connected on one side to the TCD and on the other side to a pressure sensor, which is used to measure the local absolute pressure before the carrier gas enters the capillary.
Upstream of the pressure sensor, a relief valve is used to regulate the gas flow coming from Helium (or Nitrogen) piping system.

The other capillary is the carrier gas outlet, which can be inserted into the orifice of a vertically suspended syringe (filled with water) for volumetric flow measurements.
The small capillary diameter, blocking the ingestion of water into the capillary, acts as a one-way valve, so that the gas flowing into the syringe determines, with the plunger blocked, the release of water, giving a visual measurement which can be converted in Standard Cubic Centimeters per Minute (sccm).

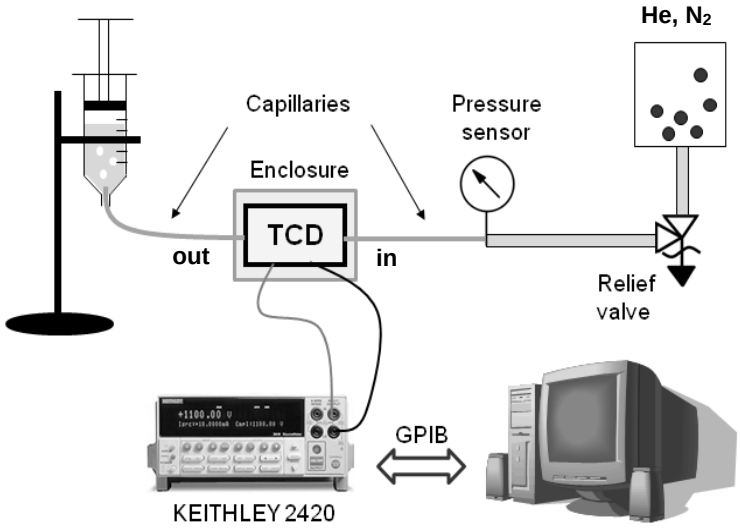

Fig. 3.34 – Experimental setup used for TCD electrical characterization.

The electrical control and measurements of the TCD are done with a Keithley 2420 source-meter, controlled in remote via GPIB: tests have been performed biasing one-by-one the four resistors forming the TCD providing a current ramp (from 400µA to 16.8mA keeping a constant step of 0.8mA for Helium, and from 200µA to 7.4mA keeping a constant step of 0.4mA for Nitrogen) and measuring the correspondent voltage drop.
Voltage-current product represents the heating power, while voltage-to-current ratio represents heater resistance, by which information on device temperature can be inferred.
A constant gas carrier volumetric flow rate of 0.5sccm (typical of fast-GC) was provided for both Helium and Nitrogen, and Heater resistance vs. Power curves are depicted in the following graph:

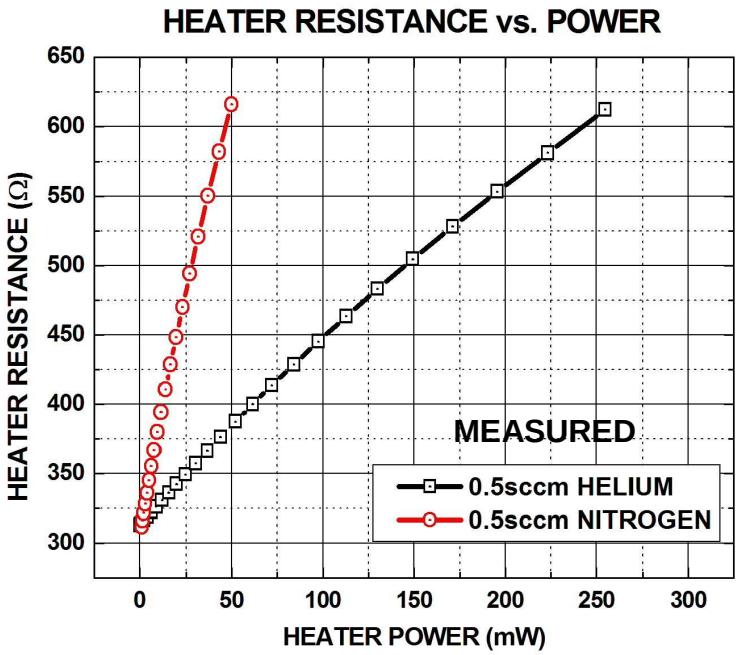

Fig. 3.35 – Measured Temperature vs. Power curves at 0.5sccm flow rates: NITROGEN (red line) and HELIUM (black line).

Since TCD resistors do not have an integrated temperature sensor, direct measurement of their temperature is not achievable: for this reason, as previously mentioned, some simplifications must be accepted in order to determine a correlation between heater resistance and resistor temperature.

By this purpose, the concept of *equivalent TCR* (TCR*) [7] is introduced: TCR* differs from temperature coefficient of resistivity of platinum (experimentally measured for TCD wafer, and its average value was found to be **0.0032 1/K**), since equivalent TCR is referred to the *entire* device, which can not be supposed to be entirely at the same temperature.

A simple model can be applied to estimate the equivalent TCR of the single resistor, using only some geometrical characteristics of the device and the measured platinum TCR, on the basis of the following procedure:

- the starting point consisted in the evaluation of the total number of resistor squares through simple electrical simulations (a value of 416 squares was found).

- Subsequently, electro-thermal simulations were performed aimed at identifying the resistor region (over the suspended membrane) where temperature can be considered fairly constant (segment BC in Fig. 3.36) and the resistor regions where temperature starts decreasing while approaching silicon bulk (segments AB and CD in Fig. 3.36).

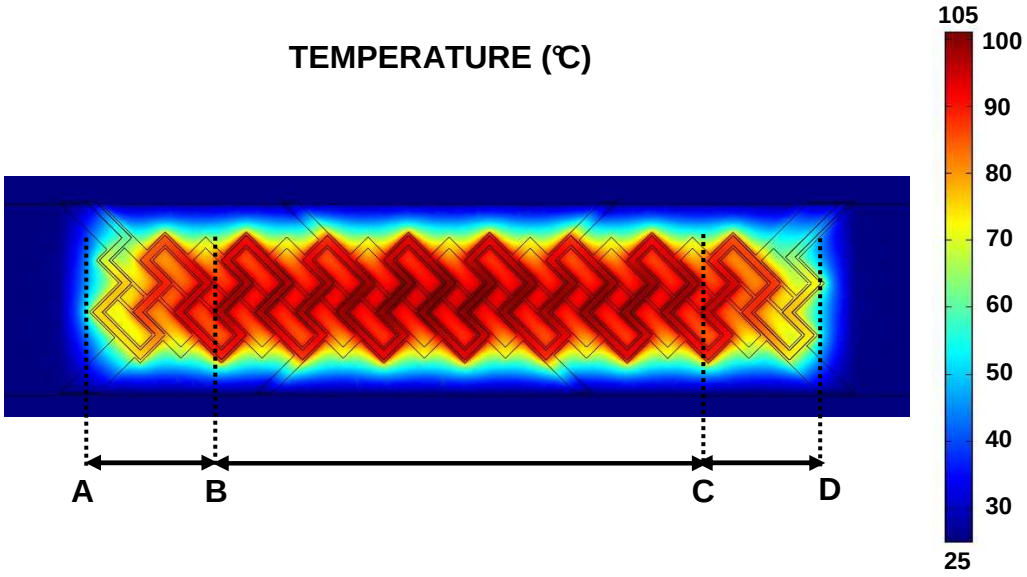

Fig. 3.36 – Example of electro-thermal simulation performed on TCD resistor.

- Number of squares for the mentioned regions was evaluated (75 for AB, 266 for BC, 75 for CD) and TCR* was calculated by assuming that nominal TCR of Platinum can be associated to region BC (being approximately at the nominal maximal temperature), while a value of TCR/2 can be associated to regions AB and BC (since their average temperature can be assumed as the half of the maximal temperature).

TCR* can be therefore calculated as:

$$TCR^{*} = \frac{SQUARE_{BC} \cdot TCR + \left(SQUARE_{AB} + SQUARE_{CD}\right) \cdot TCR/2}{SQUARE_{AB} + SQUARE_{CD} + SQUARE_{BC} + SQUARE_{PADS}} = \frac{266 \cdot 0.0032 + 75 \cdot 0.0032}{416 + 13}$$

$$= 0.002543[1/K].$$

Device resistance value at 25°C is known from measurements (310.5Ω), and through eq. (1) resistance value at 0°C can be determined, replacing TCR with TCR*:

$$R(0°C) = \frac{310.5}{1 + 0.002543 \cdot 25} = 291.9\Omega$$

Hence, resistor value that can be assumed correspondent to a temperature of 400°C can be derived from eq. (5), still replacing TCR with TCR*:

$$R(400°C) = 291.9 \cdot (1 + 0.002543 \cdot 400) = 588\Omega$$

Graph in Fig. 3.35 shows that, at fixed heater resistance of 588Ω, resistor dissipated power in helium is about five times higher with respect to nitrogen (45mW vs. 230mW): this is because heat exchange is mainly dominated by conduction, and helium thermal conductivity is more than five times higher than nitrogen (0.142 W/m·K vs. 0.026 W/m·K @ 298K).

Since Helium is the typical carrier gas used for detectors like TCDs, the previously described setup has been employed to perform resistance (or temperature) measurements as a function of dissipated power at five different volumetric flow rates (namely 0.5, 1, 2.5, 4 and 6sccm), to investigate the influence of Helium flow on device power consumption.

Results are reported in the following graph:

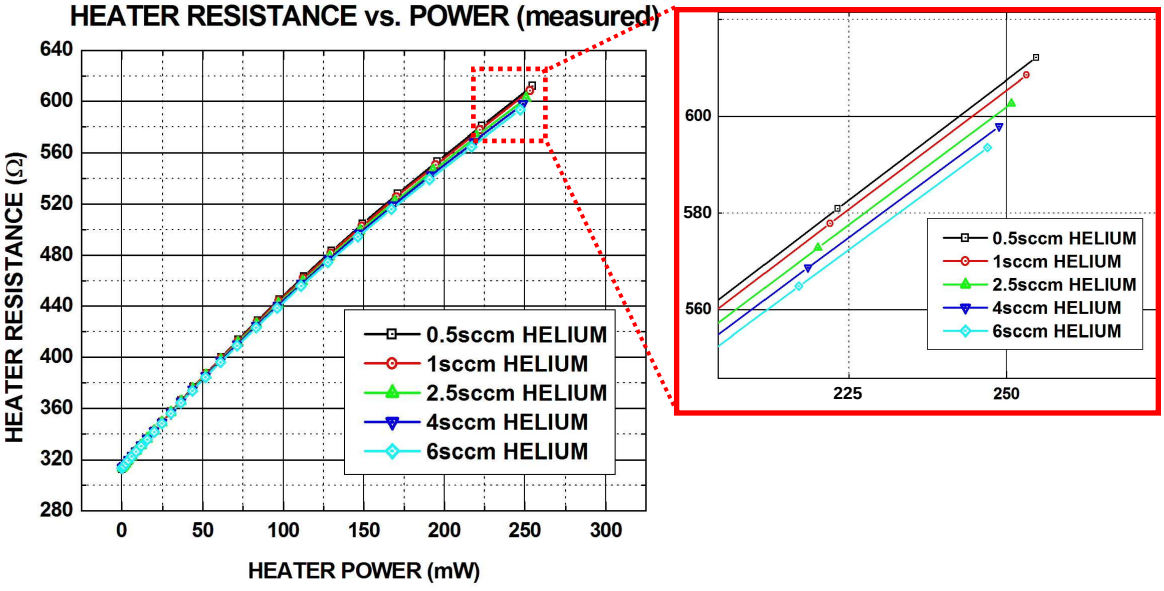

Fig. 3.37 – Measured Resistance vs. Power curves for different Helium flow rates.

which reveals that the single resistor is only slightly influenced by variations of Helium flow rate, even at values that can be considered extremely high for fast-GC applications, like 4 or 6sccm.

REFERENCES

[1] Reid V.R., Synovec R.E.: **"**High-speed gas chromatography: The importance of instrumentation optimization and the elimination of extra-column band broadening", *Talanta*, volume 76, issue 4, pp. 703 – 717 (2008).

[2] Grob R.L., Barry E.F.: "Modern practice of Gas Chromatography", 4th edition, *Published by John Wiley & Sons*, (2004).

[3] Sberveglieri G., Faglia G., Groppelli S., Nelli P., Camanzi A.: "A new technique for growing large surface area SnO_2 thin film (RGTO technique)", *Semiconductor Science and Technology*, volume 5, issue 12, pp. 1231–1233 (1990).

[4] O'Keefe V.K., Ng F.T.T., Rempel G.L.: **"**Validation of a gas chromatography thermal conductivity detection method for the determination of the water content of oxygenated solvents", *Journal of Chromatography A*, volume 1182, issue 1, pp. 113 – 118 (2008).

[5] Simon I., Arndt M.: "Thermal and gas sensing properties of a micromachined thermal conductivity sensor for the detection of hydrogen in automotive applications", *Sensors & Actuators A (Physical)*, volumes 97 – 98, pp. 104 – 108 (2002).

[6] Wanekaya A.K., Uematsu M., Breimer M., Sadik O.A.: "Multicomponent analysis of alcohol vapors using integrated gas chromatography with sensor arrays", *Sensors & Actuators B (Chemical)*, volume 110, issue 1, pp. 41 – 48 (2005).

[7] Scorzoni A., Baroncini M., Placidi P.: "On the relationship between the temperature coefficient of resistance and the thermal conductance of integrated metal resistors", *Sensors & Actuators A (Physical)*, volume 116, issue 1, pp. 137–144 (2004).

CHAPTER 4

FINITE ELEMENT METHOD: DEVELOPMENT, VALIDATION AND APPLICATIONS

4.1 – MOTIVATIONS.

In the previous chapters, a large number of micro-fabricated devices (pre-concentrators, packed separation columns, MOX sensors, capillary columns, thermal conductivity detectors) for gas chromatographic applications was presented.

The common feature for these components is represented by the fact that they are all subjected to heating processes during their operating time, by means of an electrical current flowing through a metallization.

For this reason, the capability of performing electro-thermal simulations of the micro-devices by means of a Finite Element Method (FEM) analysis, represents a powerful tool for the investigation of components behaviour at high temperatures, mainly focusing the attention on temperature distribution and power consumption increase due to heating.

Moreover, the availability of a simulation tool that provides results in good agreement with the experimental results, represents a meaningful contribution for future design optimization at design level.

In the following sections of this chapter, the development of a coupled electro-thermal model (successively implemented with a fluidic part governed by Navier – Stokes equations), its validation by comparison with experimental results obtained from ULP-MOX sensors characterization, and examples of bi-dimensional and three-dimensional simulations performed by using FEMLAB™ (a MATLAB™-based software) on the designed micro-structures are presented.

4.2 – MATHEMATICAL FORMULATION.

In this section, the equations for modelling the power dissipation of a conductive medium due to resistive heating (or Joule heating) are presented.

4.2.1 – Conductive medium equations (Electrical Model).

When handling conductive media, equation of continuity must be considered: in a stationary coordinate system, the point form of Ohm's law states that:

$$J = \sigma \cdot E + J^e \qquad (9)$$

where J is the current density, σ is the electrical conductivity, E is the electric field and J^e is an externally generated current density.

In particular, electrical conductivity σ is a temperature-dependent parameter which can be expressed in the following form:

$$\sigma(T) = \frac{1}{\rho_0 \cdot \left[1 + TCR \cdot (T - T_0)\right]} \qquad (10)$$

where ρ_0 is the electrical resistivity at the reference temperature T_0 and TCR is the well known temperature coefficient of resistivity, which describes how the electrical resistivity varies with temperature.

Starting from eq. (9), the static form of the equation of continuity results:

$$\nabla \cdot J = \nabla \cdot (\sigma \cdot E + J^e) = -\nabla \cdot \left(\sigma \cdot \nabla V - J^e\right) = 0 \qquad (11)$$

Thus, neglecting J^e, the formula that describes the electrical model is Poisson equation:

$$\nabla \cdot (\sigma \cdot \nabla V) = 0 \qquad (12)$$

whose unknown variable is represented by the electric potential V.

4.2.2 – Heat transfer equations (Thermal Model).

Heat transfer is defined as the movement of energy due to a temperature difference, and is characterized by the following three mechanisms:

- *Conduction*: it takes place when heat is transported by diffusion in a stationary medium (a solid or a fluid) due to a temperature gradient.
- *Convection*: it takes place when heat is transported by a fluid motion (heat transfer between either a hot surface and a cold moving fluid or a cold surface and a hot moving fluid).
- *Radiation*: it takes place when heat is transported via electromagnetic waves between two surfaces (A and B) with different temperatures (T_A and T_B).

Heat transfer equation includes all these mechanisms, expressed in the formulation given by Fourier's law:

$$Q = \underbrace{-\nabla \cdot (k \cdot \nabla T)}_{\text{CONDUCTION}} + \underbrace{\rho \cdot c_p \cdot u \cdot \nabla T}_{\text{CONVECTION}} + \underbrace{\varepsilon \cdot \sigma_{SB} \cdot \left(T^4 - T_A{}^4\right)}_{\text{RADIATION}} + \underbrace{\rho \cdot c_p \cdot \frac{\partial T}{\partial t}}_{\text{TRANSIENT TERM}} \qquad (13)$$

where Q is the heat source, k is the thermal conductivity, T is the temperature (unknown variable of the thermal model), ρ is the density, c_p is the heat capacity, u is velocity, ε is the emissivity, σ_{SB} is the Stefan-Boltzmann constant ($5.67 \cdot 10^{-8}$ $W/m^2 \cdot K^4$) and T_A is ambient temperature.

In case of a steady state problem, temperature does not change with time and the transient term is neglected.

4.2.3 – Electro-thermal coupling.

The target is represented by the formulation of a single equation which groups the electrical and the thermal model, thus including both the unknown variables V and T.

The capability to couple the two models comes form the consideration that, in Joule heating, temperature increase is due to the resistive heating caused by electric current: in particular, the generated resistive heat Q is proportional to the square of the electric current density magnitude J, and the coefficient of proportionality is the electric resistivity ρ, which is the reciprocal of the temperature-dependent electric conductivity σ = σ(T):

$$Q = \frac{1}{\sigma(T)} \cdot |J|^2 \qquad (14)$$

Combining eq. (9), (11) and (14), the relation between heat source Q and electric potential V can be easily disclosed:

$$Q = \frac{1}{\sigma(T)} \cdot |J|^2 = \frac{1}{\sigma(T)} \cdot |\sigma(T) \cdot E|^2 = \sigma(T) \cdot |\nabla V|^2 \qquad (15)$$

Finally, replacing the term Q in eq. 13 with the value obtained from eq. 15, the fully coupled relation is carried out:

$$\sigma(T) \cdot |\nabla V|^2 = -\nabla \cdot (k \cdot \nabla T) + \rho \cdot c_p \cdot u \cdot \nabla T + \varepsilon \cdot \sigma_{SB} \cdot \left(T^4 - T_A{}^4\right) \qquad (16)$$

and contains both the unknown variables V and T.

4.3 – ELECTRO-THERMAL MODEL VALIDATION.

The validation of the coupled electro-thermal model was carried out by comparing the simulation results with the experimental characterization performed on the previously described ULP hotplates (see chapter 3).

In particular, three different typologies were considered for the device, depending on the shape of the suspended dielectric arms (MINIMAL, EXTRA-ARMS or BRIDGE, see Fig. 4.1) and keeping constant the remaining geometrical parameters (metallizations width W = 4μm, pit width P = 400μm):

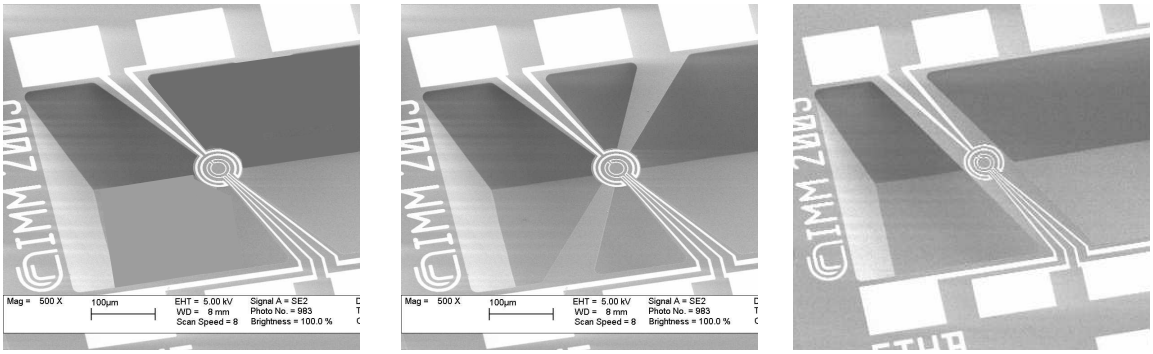

Fig. 4.1 – SEM micrographs of the considered structures: MINIMAL (left), EXTRA-ARMS (centre), BRIDGE (right).

A single chip of "Temperature Sensor configurations" (containing the three different devices, see mask layout in Fig. 4.2) was chosen from a ULP hotplates silicon wafer and electrically characterized: in parallel, with the purpose of implementing the model with no fitting parameters, all the physical, electrical, thermal and optical properties of the material thin films employed in the devices were experimentally evaluated by using appropriately designed test structures.

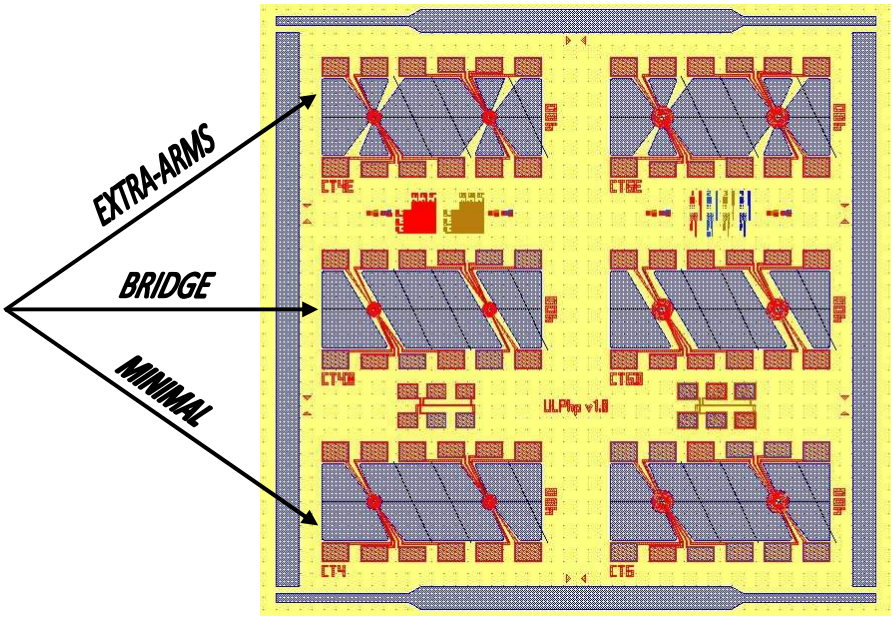

Fig. 4.2 – Mask layout of a "Temperature sensor" chip.

4.3.1 – Physical properties evaluation.

Material layers thicknesses were experimentally measured during the various steps of the technological process by using a mechanical profilometer, and results are reported in the following table:

LAYER		THICKNESS
DIELECTRIC MEMBRANE	THERMAL SiO_2	525 nm
	LPCVD Si_3N_4	290 nm
	LOW THERMAL SiO_2 (LTO)	605 nm
PLATINUM		210 nm
DEPTH OF D-RIE ETCHED SILICON		150 µm

Tab. 5 – Measured thicknesses of MOX sensor material layers.

4.3.2 – Electrical properties evaluation.

The Temperature Coefficient of Resistivity (TCR) of the metallizations was thoroughly investigated, since (as already mentioned in chapter 2) the TCR of sputtered thin film of Platinum is expected to differ from the values found in literature for bulk Platinum (0.0038 1/K).

For the evaluation of TCR, a specific platinum test structure defined on the chip (visible in Fig. 4.2 and reported also in Fig. 4.3) was used:

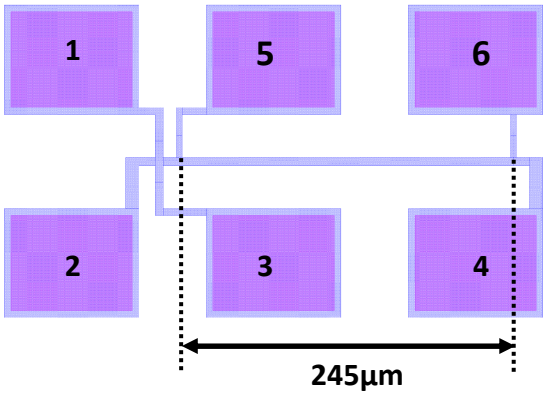

Fig. 4.3 – Test structure used for the evaluation of the TCR of Platinum metallizations.

The TCR was measured by means of a 4-point setup, through the following steps:

- first, the value of platinum square resistance at RT = 25°C was achieved by performing four-points measurements on the Van der Pauw structure identified by the pads 1, 2, 3 and 4 (a value of **R_{SQUARE}(25°C) = 0.855Ω** was measured).
- This measurement was repeated at four different temperatures (50, 100, 150, and 200°C) inside an environmental chamber (Sun Systems EC11, maximum temperature 200°C, chamber maximum temperature gradient 1°C) using a Keithley 2410 multimeter configured for 4-probe resistance measurement.
- The values of the square resistance as a function of temperature were logged (see Fig. 4.4), and the linear fit identified the relation:

$$R_{SQUARE}(T) = \underbrace{R_{SQUARE}(0°C)}_{A} + \underbrace{R_{SQUARE}(0°C)\cdot TCR \cdot T}_{B} \qquad (17)$$

Values of A and B were calculated and resulted A = 0.82951 and B = 0.00253, thus **TCR = B/A = 0.00305 (1/K)**.

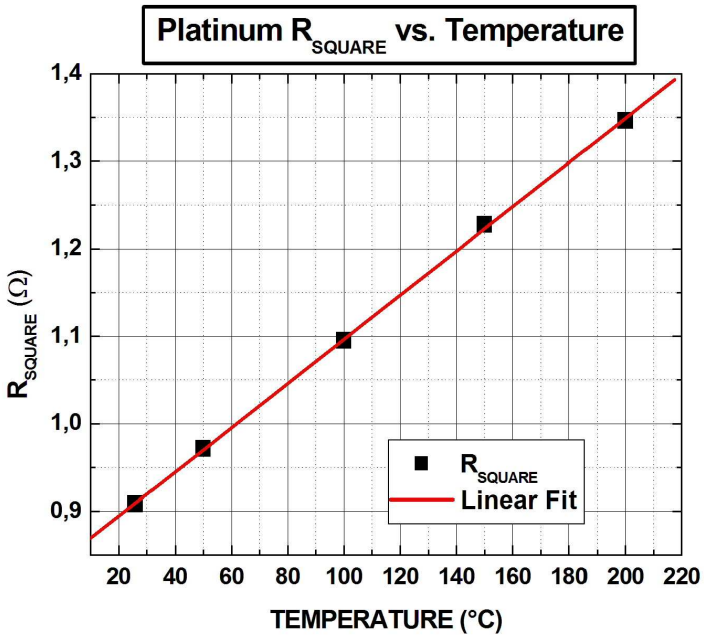

Fig. 4.4 – Values of R_{SQUARE} at different temperatures with linear fit .

The evaluation of R_{SQUARE} at RT = 25°C also allowed to measure the track width of the heater and the temperature sensor (by evaluating the resistance of the 245µm-long platinum metallization between pads 5 and 6 in the structure of Fig. 4.3) and, in addition to that, the electrical resistivity of platinum at RT = 25°C, defined as:

$$\rho(25°C) = \frac{R_{SQUARE}(25°C)}{Pt\_Thickness} = \frac{0.855}{210 \cdot 10^{-9}} = 4.07 \cdot 10^{6} [\Omega / m] \qquad (18)$$

Track widths were found to be around 10% smaller than the value resulting from the mask layout (3.6µm vs. 4µm), probably due to some non ideal characteristics of the photolithographic definition and platinum lift off process.

4.3.3 – Thermal properties evaluation.

To measure thermal conductivities of the material thin layers reported in Tab. 5, an experimental setup was prepared involving proper on-chip microstructures that use a supporting membrane on which a thin film can be deposited and characterized.

In particular, the proposed test structures consist of dielectric cantilevers whose free end can be heated by a heavily-doped poly-silicon resistor (see Fig. 4.5)

The cantilever dimensions were 200μm in width and 150μm in length, just like the structures proposed by Von Arx in [1].

In the measurements, a joule-induced heating has been applied in order to create a temperature gradient across the test sample, placed over the cantilever, while with a poly-silicon thermistor realized close to the test layer hot end, the temperature increase was measured from the resistance variation.

Both resistors are connected to bonding pads by platinum metallizations, placed over suspended dielectric arms.

The different structures (reported in Fig. 4.6) have been designed in the following way: structure (a) is the reference one, composed by a plain dielectric membrane (a stack of silicon dioxide and silicon nitride), while in the other devices a layer is added, such as sputtered platinum in (b), or removed, such as silicon nitride in (c) or the entire dielectric membrane in (d).

As proposed in [1], the thermal conductance of an added layer was determined by subtracting the overall measured conductance of the reference cantilever from the conductance of the corresponding one, while the thermal conductance of a removed layer was determined by subtracting the overall measured conductance of the corresponding cantilever from the conductance of the reference one.

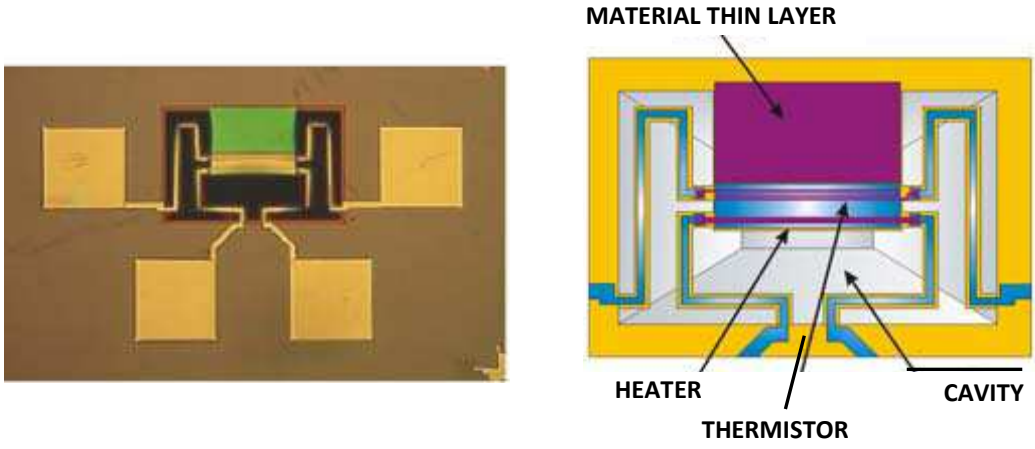

Fig. 4.5 – Optical micrograph (left) and schematic representation (right) and of the micro-machined test structure used for thermal conductivity measurements.

To eliminate the influence of heat exchange through air, the measurements were performed on bonded devices in a vacuum chamber setup, equipped with a rotary pump able to perform a vacuum level of about $2 \cdot 10^{-3}$ mbar.

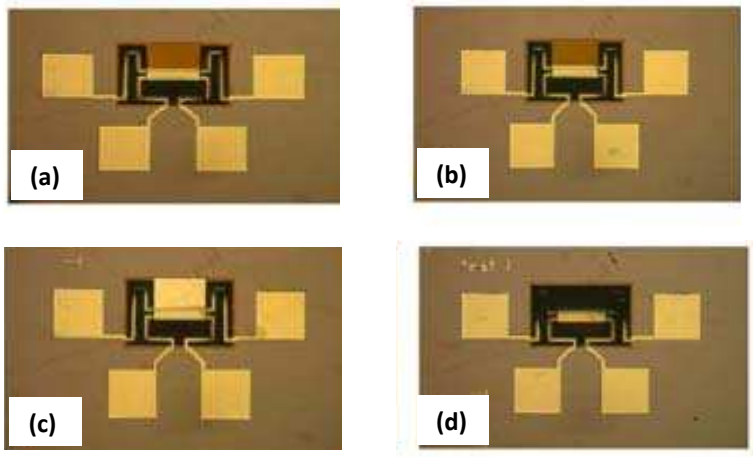

Fig. 4.6 – Optical micrographs of the test structures: reference cantilever (a), silicon dioxide (b), reference + Platinum (c) and no cantilever (d).

The operating principle of the test structure relies on the fact that, when a power P is dissipated on the poly-silicon heater, the temperature of the cantilever tip is increased of ΔT with respect to the substrate.

At the steady state, the heat flow taking place along the cantilever and the four arms towards the silicon bulk balances the produced heating power P, and consequently, the following relation holds between P and the produced temperature difference ΔT:

$$P = G_T \cdot \Delta T \qquad (19)$$

where G_T is the overall thermal conductance of the cantilever.

If the contribution of the cantilever body and of the four arms is considered as additive in the structure, the result is given by:

$$G_T = G_A + G_C \qquad (20)$$

where G_A and G_C indicate the thermal conductance pertaining to the four arms and the cantilever respectively.

The cantilever thermal conductance GC may also be written as:

$$G_C = \sum_i \frac{k_i \cdot d_i \cdot w}{L} \qquad (21)$$

in which the sum must span over all the different thin films in the cantilevers, while with k_i, d_i, w and L the respective thermal conductivities, layer thicknesses, width and length are denoted.

In the measurements, the setup represented in Fig. 4.7 has been adopted, which allowed to heat the micro-machined cantilever by imposing a current to the resistor placed over the free end of the structure (I_H).

The temperature difference ΔT produced in such way is simultaneously measured through the resistance change of the second poly-silicon meander, placed very close to the test layer hot side.

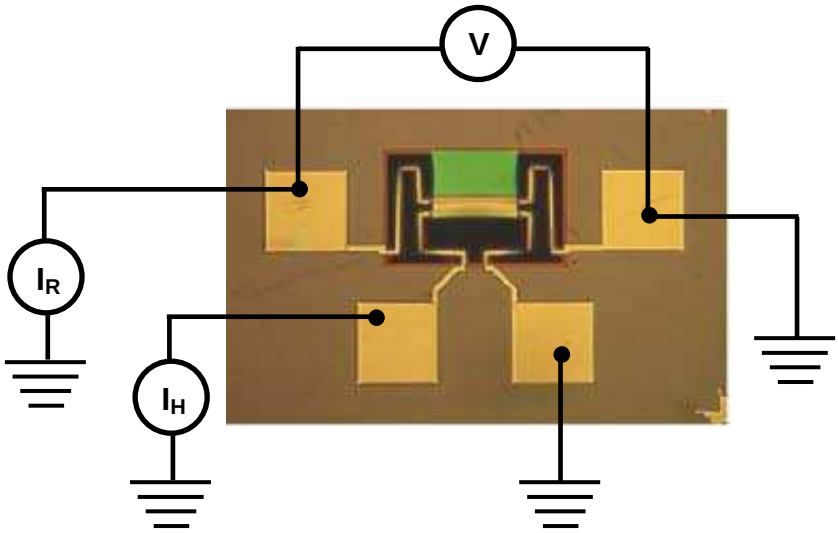

Fig. 4.7 – Electrical probe setup used in thermal conductivity measurements.

In order to minimize the measurement errors, fixed current values (0, 125, 250, 375, 500μA) were applied to the heater (I_H), while the thermistor bias current (I_R) was ramped up from (I_{TH} - ΔI_{TH}) to (I_{TH} + ΔI_{TH}), being I_{TH} a reference value around 10μA.

From the slope of the resulting V(I_{TH}) curves, an offset-compensated thermistor resistance value (R_{TH}) and, consequently, the temperature increase ΔT value were obtained.

This was performed for each I_H value in order to derive several ΔT values corresponding to increasing powers: once the temperature differences have been determined in such

way, the thermal conductance has been calculated from the known heating power applied using the expression (19), where $P = P_H = R_H \cdot I_H^2$ is heater dissipated power.
Thermal conductance values obtained applying this method to the different test structures presented in Fig. 5.6 are reported in Tab. 6.

TEST STRUCTURE	CONDUCTANCE [μW/K]
REFERENCE	**8.65**
SILICON DIOXIDE	**7.28**
REFERENCE + PLATINUM	**35.4**
NO CANTILEVER (ARMS)	**3.35**

Tab. 6 – Thermal conductance values measured on the test structures.

By knowing the thermal conductance corresponding to the reference cantilever and the test one, and reminding Eq. 21, the thermal conductivity of the single layer k_{LAYER} can be calculated as:

$$k_{LAYER} = \left| G_{LAYER} - G_{REF} \right| \cdot \frac{L}{d_{LAYER} \cdot w_{LAYER}} \qquad (22)$$

Results obtained with the proposed method on the material layers of Tab. 5 are shown in Tab. 7 (values reported at RT = 298K):

MATERIAL LAYER	CONDUCTIVITY [W/m·K]
SILICON NITRIDE	**2.6**
SILICON DIOXIDE	**1.2**
PLATINUM	**58**

Tab. 7 – Thermal conductivity values measured on the material thin layers.

4.3.4 – Optical properties evaluation.

Typical working temperatures for MOX sensors are in the [250°C ÷ 450°C] range and, especially in proximity of the upper limit, the contribution of radiation to overall heat transfer (and hence to power consumption) can not be neglected.
For this reason, optical simulations of the different layer stacks composing the ULP hotplate have been performed (in a wavelength range of [1μm ÷ 12μm]) by using the

software OPTICAL [2], aimed at obtaining the average values of emissivity ε to be used in the electro-thermal model.

Results are reported in the following table:

MATERIAL STACK	EMISSIVITY
DIELECTRIC MEMBRANE (SiO_2 + Si_3N_4 + SiO_2)	**0.1**
DIELECTRIC MEMBRANE + PLATINUM (UPSIDE)	**0.05**
DIELECTRIC MEMBRANE + PLATINUM (DOWNSIDE)	**0.177**

Tab. 8 – Average values of emissivity used in the model.

4.3.5 – 2D Simulations.

A preliminary validation of the electro-thermal model (implemented with the values of electrical, thermal and optical properties previously determined) was carried out by comparing a set of bi-dimensional simulation results with a set of experimental results obtained by measuring the chip containing the array of ULP hotplates in vacuum.

In particular, measurements were performed by inserting the TO8 case, where the chip has been wire-bonded, inside a vacuum chamber (equipped with a rotary pump able to perform a vacuum level of $2 \cdot 10^{-3}$ mbar) and adopting the same principle described in chapter 2 (section 2.4) for wafer level characterization of ULP hotplates: in this specific case, the electrical characterization system consisted of a Keithley 2410 source-meter (connected to the TO8 pads corresponding to the heater) and a Keithley 2425 source-meter (connected to the TO8 pads corresponding to the temperature sensor).

In such vacuum configuration, air contribution as heat conducting material was neglected and heat exchange resulted only from conduction through dielectric layers and metallizations, and at high temperatures (~ 400°C) also from radiation.

For this reason, the use of a 2D-model is appropriate: in fact, since the thicknesses of dielectric membrane and platinum metallizations are very small compared to the overall hotplate dimensions (three orders of magnitude), we can assume that there is no temperature gradient along the vertical direction and, according to this, any multilayer can be modelled as a single layer, characterized by an average thermal conductivity k_{av}, whose value can be obtained from the expression:

$$k_{av} = \frac{\sum_i k_i \cdot th_i}{th_{tot}} \qquad (23)$$

where k_i and th_i are the thermal conductivities and the thicknesses of the single layers and th_{tot} is the thickness of the considered multilayer.

As an example, considering the structures illustrated in Fig. 5.1, the thermal conductivity of the dielectric membrane multilayer is given by:

$$k_{memb} = \frac{k_{SiO_2} \cdot th_{SiO_2} + k_{Si_3N_4} \cdot th_{Si_3N_4} + k_{LTO} \cdot th_{LTO}}{th_{SiO_2} + th_{Si_3N_4} + th_{LTO}} = \frac{(1.2 \cdot 525 + 2.6 \cdot 290 + 1.2 \cdot 605)}{525 + 290 + 605} =$$

$$= 1.486 \left[\frac{W}{m \cdot K} \right] \qquad (24)$$

while the thermal conductivity of the multilayer formed by the dielectric membrane and the platinum metallizations is given by:

$$k_{memb+Pt} = \frac{k_{SiO_2} \cdot th_{SiO_2} + k_{Si_3N_4} \cdot th_{Si_3N_4} + k_{LTO} \cdot th_{LTO} + k_{Pt} \cdot th_{Pt}}{th_{SiO_2} + th_{Si_3N_4} + th_{LTO} + th_{Pt}} =$$

$$= \frac{(1.2 \cdot 525 + 2.6 \cdot 290 + 1.2 \cdot 605 + 58 \cdot 210)}{525 + 290 + 605 + 210} = 8.767 \left[\frac{W}{m \cdot K} \right] \qquad (25)$$

The adopted COMSOL™ multiphysics model was obtained by coupling the Conductive Media DC model (electrical part) with the General Heat Transfer model (thermal part).

As far as the electrical model is concerned, the only sub-domain involved is represented by the platinum metallizations, whose temperature-dependent electrical conductivity is:

$$\sigma(T) = \frac{\sigma(25°C)}{(1 - TCR \cdot 25)} \cdot \frac{1}{(1 + TCR \cdot T)} \qquad (26)$$

where $\sigma(25°C)$ is the reciprocal of the value reported in eq. (18) and TCR = 0.00305 (1/K) (as shown in section 4.3.2), while the electrical boundaries of the structures are all assumed as insulated except for the two terminals of the heater (one is biased with a specific voltage V_H and the other at 0V).

With regard to the thermal model, two different sub-domains have to be considered: i) the dielectric membrane multilayer and ii) the multilayer formed by the dielectric

membrane and the platinum metallizations, whose thermal conductivity values have been previously calculated with eq. (24) and (25).

The only thermal boundaries are represented by the metallizations pads defined over the silicon bulk (and not over the suspended dielectric membrane), whose temperature was fixed at RT = 298K, while for the remaining boundaries a condition of thermal insulation was imposed.

The analysis proceeded with the discretization of the simulated structures by means of a mesh formed by a large number of triangular elements, in order to evolve from a continuum condition to a discrete one (basic principle of the finite element methods).

The solution of the problem, hence, is assumed to be expressed on each finite element by a linear combination of functions (shape functions), whose coefficients are identified as the "degrees of freedom", i.e. the unknown quantities of the algebraic problem obtained with the discretization.

In this way, the mathematical solution of the continuum problem (characterized by an infinite number of degrees of freedom) is approximated with a discrete solution, introducing an error (relative tolerance) which represents the mismatch between the two solutions.

In the following picture, an example of mesh referred to the MINIMAL structure is reported (heater terminals highlighted in red, number of triangular elements = 38165, number of degrees of freedom = 152303, relative tolerance = 10^{-6}).

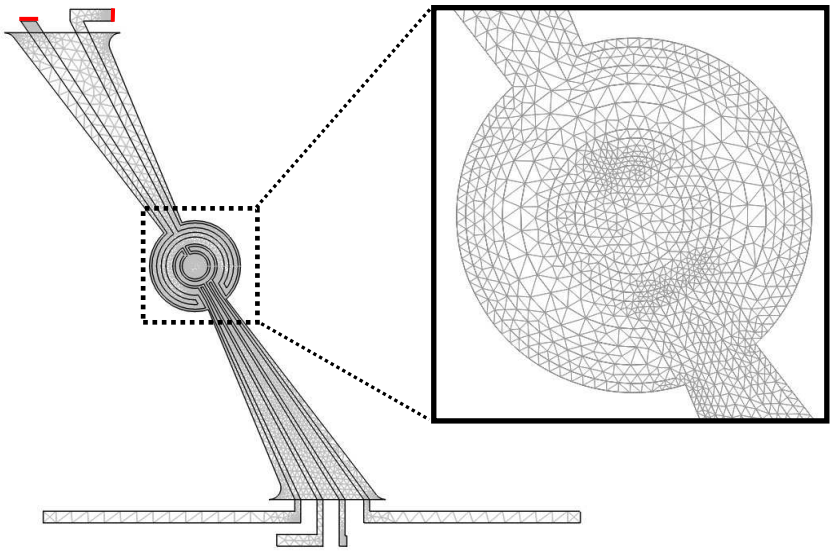

Fig. 4.8 – 2D-mesh of the MINIMAL structure and (inset) of the circular hot spot.

In Fig. 4.9, examples of simulated 2D-temperature distribution, obtained by applying the electro-thermal model to the three different structures, are presented:

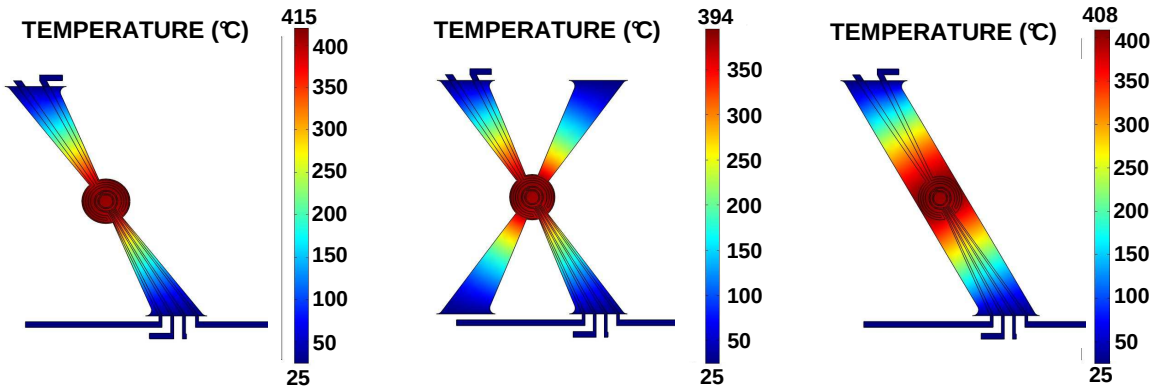

Fig. 4.9 – 2D-temperature distributions obtained on ULP structures with numerical simulation: MINIMAL (left), EXTRA-ARMS (centre), BRIDGE (right).

An excellent temperature uniformity in the central hot spot (favoured by the heater circular symmetry) can be noticed, illustrated also in Fig. 4.10 for the MINIMAL structure by the temperature distribution along the horizontal cut-line highlighted in black:

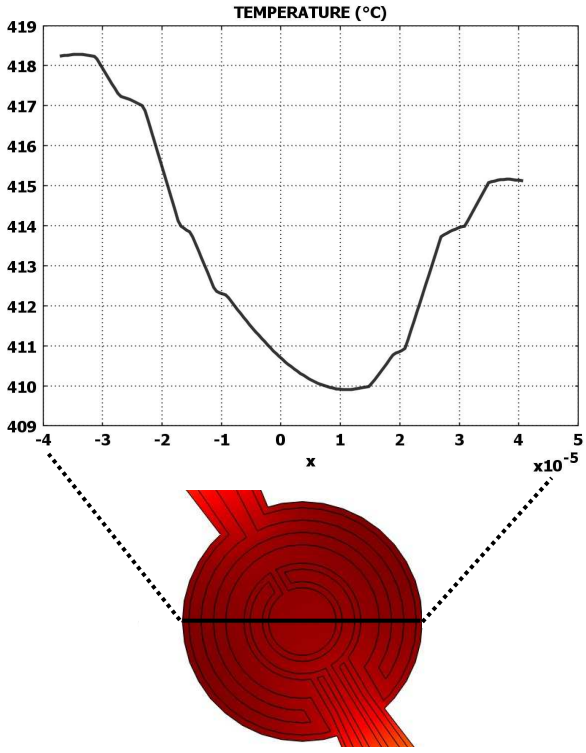

Fig. 4.10 – Temperature distribution in the circular hot-spot, along the cut-line in black.

The comparison between experimental results and simulations was performed by achieving the "Temperature vs. heater power consumption" curves: in particular, the experimental value of temperature was obtained through the measurement principle described in chapter 2 (section 2.4) by applying eq. (2), while the punctual value of temperature obtained from simulations and used for the comparison was chosen in an intermediate position over the circular hot-spot surface (counting on the excellent temperature uniformity shown in Fig. 4.10), as illustrated in the following figure:

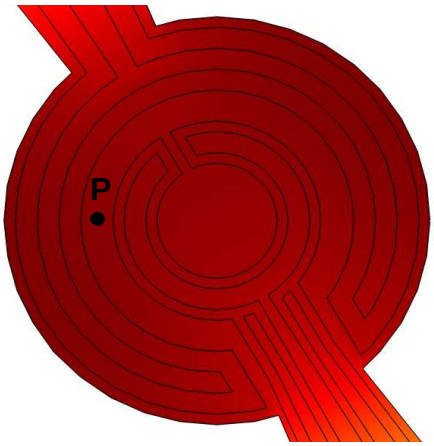

Fig. 4.11 – Point on the hot-spot area corresponding to the simulated temperature value.

The corresponding value of simulated power consumption was achieved by multiplying the bias voltage V_H (applied to one pad of the heater) with the value of electrical current I_H obtained from a boundary integration performed on the heater pads.

Fig. 4.12 shows the result of the comparison: six identical experimental and simulated heater power values (corresponding to temperatures approximately of 25, 50, 100, 200, 300 and 400°C) were considered for the three ULP hotplate structures and logged in a graph.

The analysis of the curves revealed that, as expected, bigger structures (BRIDGE and EXTRA-ARMS) are characterized by a higher power consumption, and most of all that an excellent agreement (relative error ~ 1.5%) between measured and simulated results can be carried out.

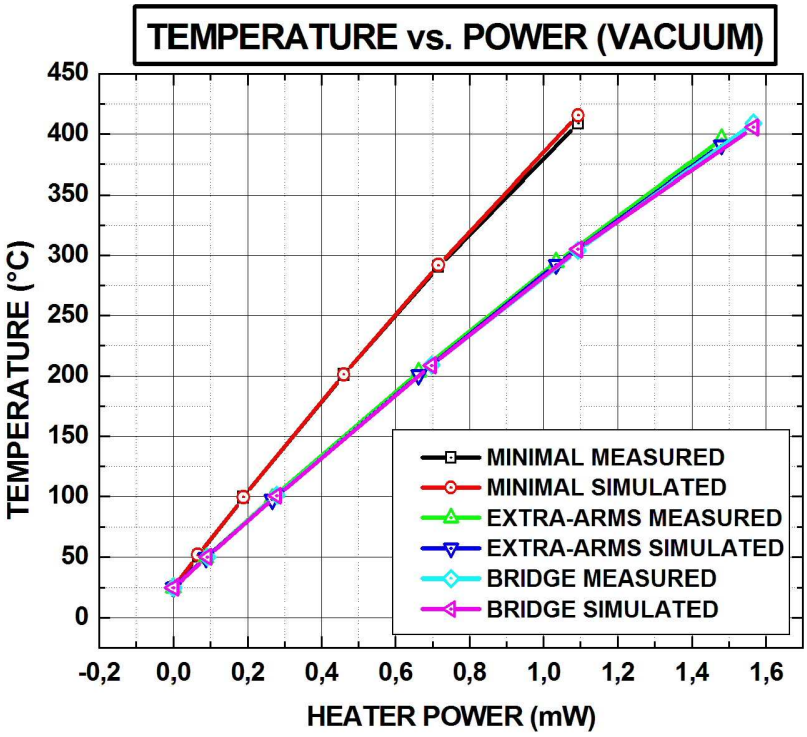

Fig. 4.12 – Temperature vs. Power curves (VACUUM): measurements vs. simulations.

4.3.6 – 3D Simulations.

The electro-thermal model validation continued by introducing the contribution of air as heat-conductive medium and performing three-dimensional simulations, whose results were compared with the experimental characterization of the three structures performed at atmospheric pressure.

An example of the simulated EXTRA-ARMS device is reported in figure 4.13, where the 500µm-thick silicon bulk (thermal conductivity = 148 W/m·K), the hotplate (obtained by the extrusion of the 2D-structure, using the real material thicknesses), the 150µm-deep pit underneath the structural membrane (filled with air), and a 4mm-diameter sphere surrounding the whole structure (also filled with air) can be disclosed.

Although three different mechanisms have to be considered for heat transfer (see eq. 13), in numerical simulations of micro-hotplates reported so far in the literature [3], the convective contribution has been completely neglected in favour of a solid-like representation of air.

This simplification is generally justified by assuming that air motion represents a second-order effect in thermal devices at the micro-scale, with respect to thermal conduction through the gas phase.

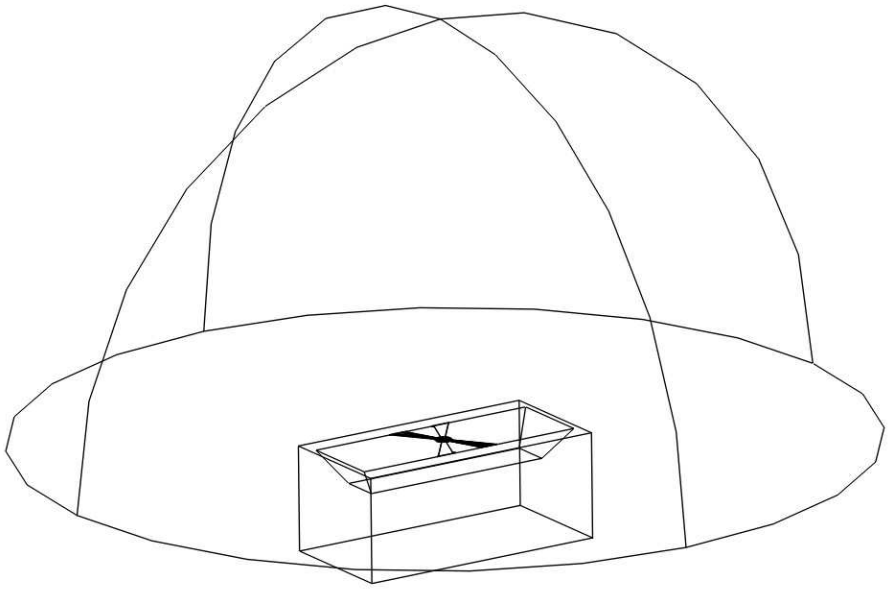

Fig. 4.13 – Simulated three-dimensional structure.

For this reason, only conduction (and, for temperatures higher than 350°C, radiation) was considered in heat balance and, as far as it concerns the expression of air thermal conductivity, the following formula [3] was employed in the model:

$$k_{AIR}(T) = 0.026 \cdot \left[1 + 3 \cdot 10^{-3} \cdot (T - T_{AMB}) - 1.285 \cdot (T - T_{AMB})^2\right] \qquad (27)$$

which takes into account its dependence from temperature.

The problem was addressed in an analogous way of the bi-dimensional simulation, with the following differences:

- the discretization was obtained by creating a three-dimensional mesh made of *tetrahedral* elements, that was thickened in correspondence of the boundary layer between the hotplate and the surrounding air.

- All the external thermal boundaries (bulk silicon + sphere) were set at RT = 298K, while for the remaining boundaries (internal) a condition of continuity was imposed.

In Fig. 4.14, the temperature distribution on the plane correspondent to metallizations surface for the EXTRA-ARM structure is presented (number of tetrahedral elements = 59068, triangular boundary elements = 10402, edge elements = 1957, vertex elements = 417, number of degrees of freedom = 87962, relative tolerance = 10^{-6}):

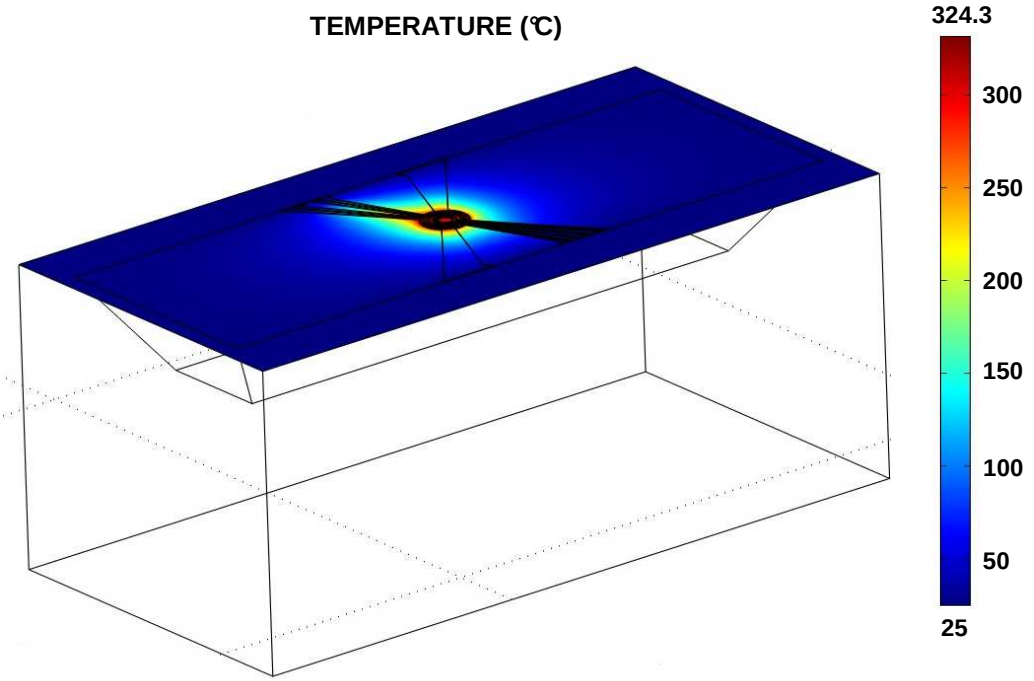

Fig. 4.14 – Temperature distribution over the surface of the simulated three-dimensional EXTRA-ARMS structure.

As in the case of the bi-dimensional simulations, temperature uniformity in the central hot spot at typical work temperatures (~400°C) was investigated, and the result is reported in fig. 4.15 for the EXTRA-ARMS structure: the horizontal cut-line highlighted in black was considered (in correspondence of the platinum metallizations surface), and a temperature gradient of 43°C was devised, from a minimum of 402°C to a maximum of 445°C.

This 10% discrepancy is fairly higher with respect to the vacuum condition (only 2%, from 410 to 418°C) due to the presence of air, which provides a further path to heat dissipation.

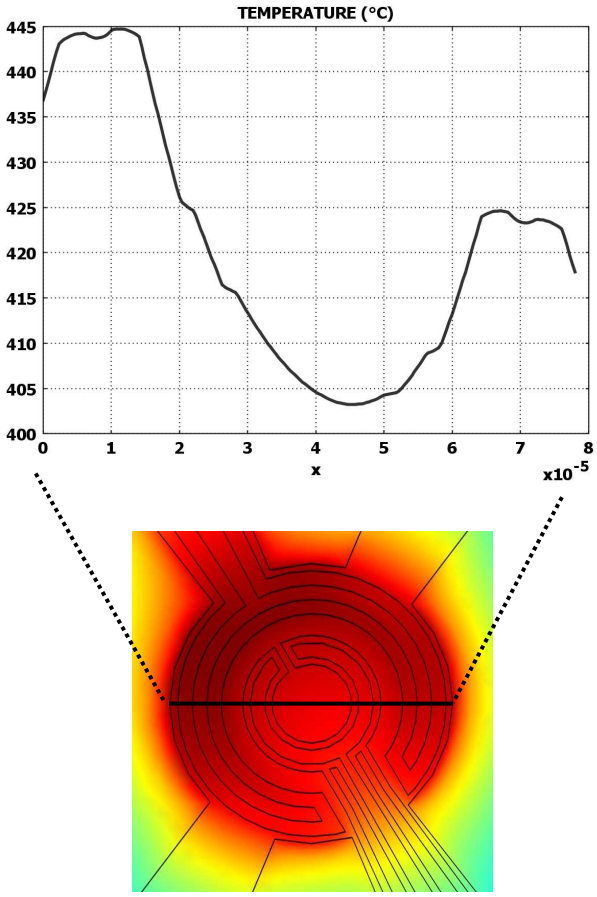

Fig. 4.15 – 3D-temperature distribution in the circular hot-spot, along the cut-line highlighted in black.

The punctual value of temperature obtained from 3D-simulations and used for the comparison was chosen in the same intermediate position over the circular hot-spot surface identified for the 2D-simulations, and the result of the comparison between experimental and simulated results is reported in the graph of figure 4.16.
The data analysis revealed that:

- the influence of air on hotplates power consumption is predominant, in fact more than 80% of power dissipation is due to heat conduction through air.

This phenomenon is mainly remarkable for the MINIMAL structure, whose power dissipation at 400°C is eight times higher in air with respect to vacuum (1.1 mW vs. 8.9 mW), while is slightly less relevant for EXTRA-ARMS (1.5mW vs. 9.5mW) and BRIDGE (1.55mW vs. 10mW) structures.

- The agreement between simulated and experimental curves is very good, in fact the relative error in proximity of 400°C is about 5%.

  The increase in relative error with respect to the vacuum condition can be explained with the uncertainty in the evaluation of thermal conductivity of air, whose expression was taken from literature, and with the fact that, in the electro-thermal model, its dependence from relative humidity was neglected.

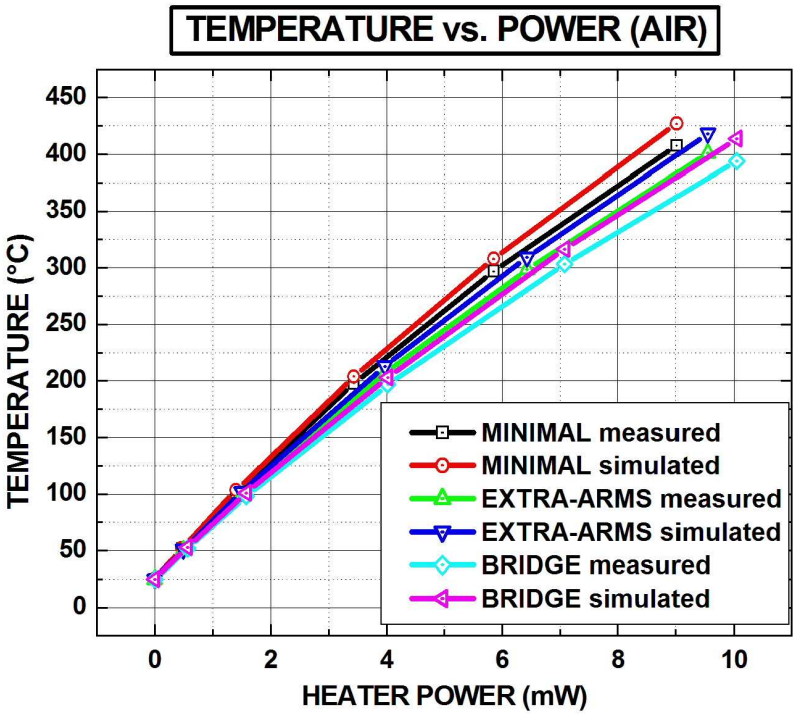

Fig. 4.16 – Temperature vs. Power curves (AIR): measurements vs. simulations.

4.4 – TRANSIENT ANALYSIS.

The results presented up to now in this chapter are all related to steady state analysis, thus the term $\rho \cdot C_P \cdot \frac{\partial T}{\partial t}$ that figures in eq. (13) was not considered when performing the simulations (ρ = material density [Kg/m^3], C_P = material heat capacity [J/Kg·K]).

On the other hand, the capability to achieve information about the response times of devices subjected to heating and/or cooling mechanisms is mandatory, especially for structures like those presented in this work, which are all characterized by an operation principle that involves very high working temperatures (typically $\geq 200°C$).

For this reason, the previously described electro-thermal model can be employed to perform time-domain transient analysis of the designed micro-devices.

A similar approach to the one described in section 4.3.5 was used to evaluate density and heat capacity of the involved multilayers, starting from the corresponding values of the single layers acquired from FEMLAB™ material database and reported in table 9: in particular, these values refer to RT = 298K and their dependence from temperature was neglected in the model.

LAYER	ρ [Kg/m^3]	C_P [J/Kg·K]
Silicon	2330	703
Platinum	21386	132.6
Silicon Nitride	3290	660
Silicon Dioxide	2650	730

Tab. 9 – Density and heat capacity values at RT = 298K for the single layers.

On the contrary, temperature-dependent ρ and C_P where considered for air, acquired in the same way from FEMLAB™ material database, and employed in the model: plots are presented in the following figure

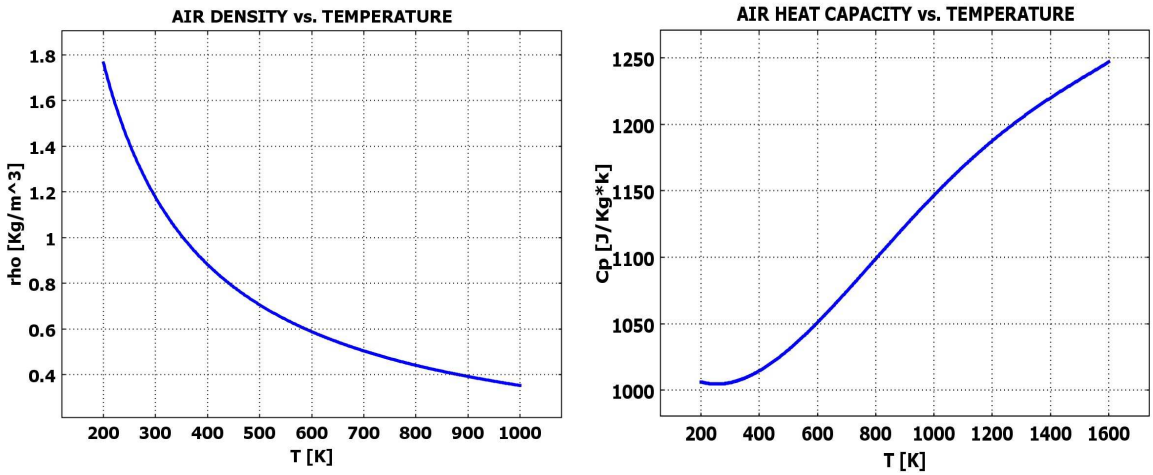

Fig. 4.17 – Air density (left) and air heat capacity (right) vs. temperature plots.

To validate the model, a comparison between experimental and simulated results obtained on the MINIMAL structure presented in chapter 3 (Fig. 3.13) was performed: in particular, a preliminary steady-state simulation of the device at 400°C was executed, and its result was stored and considered as the starting point of the subsequent cooling transient simulation, obtained by imposing a zero-voltage on the heater (mesh parameters: number of tetrahedral elements = 43415, triangular boundary elements = 8051, edge elements = 1674, vertex elements = 429, number of degrees of freedom = 66507, relative tolerance = 10^{-6}).

As already shown in Fig. 3.14, a very short thermal time constant of 1.47 ms experimentally found, while from simulations a value of 1.32ms has been achieved, as illustrated in the following figure:

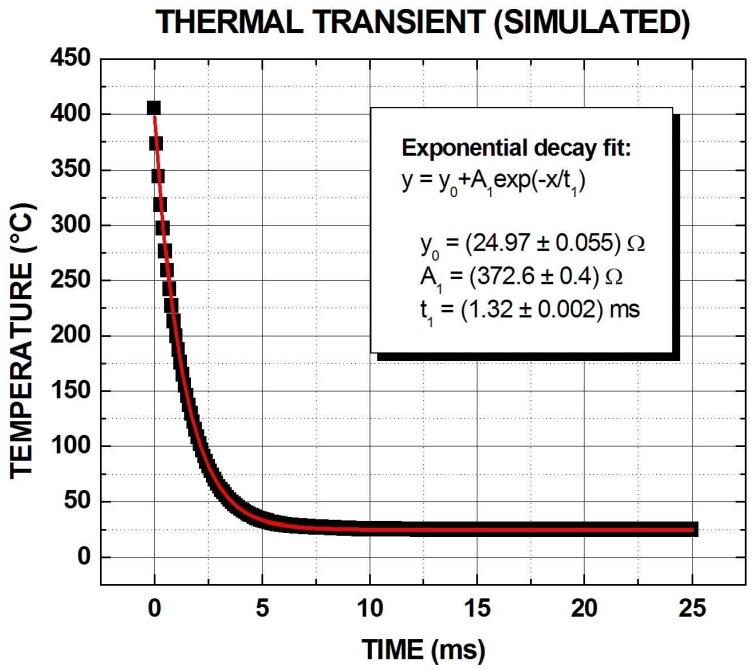

Fig. 4.18 – Simulated cooling transient for MINIMAL structure, W = 4μm, P = 250μm.

The good match disclosed from the comparison of measured and simulated thermal time constant values corroborated the validity of the proposed model also for transient analysis, and induced its exploitation for evaluating micro-fabricated TCDs thermal time constant (to investigate their response times to heating/cooling mechanisms), as described in section 4.6.1.

4.5 – FLUIDIC MODEL IMPLEMENTATION.

Basic concepts of fast-GC have been thoroughly explained in chapter 3, such as the necessity to encapsulate GC detectors within ultra-low volume chambers, in order to reduce dead volumes as much as possible

At this purpose, micro-fabricated ULP-MOX sensors and TCDs provided with an integrated micro-chamber (presented in the previous chapter) have been thoroughly simulated, to investigate their behaviour in presence of a gas flow inside the chamber; clearly, the electro-thermal model was no more suitable to the purpose, and for this reason it has been implemented with a fluid-mechanical part to study the motion of fluid flow.

Formulation of the fluidic model is based on Navier-Stokes equations (already introduced in chapter 3), whose unknown quantities are fluid velocity field (u, v, w) along x, y and z-direction and fluid pressure (p).

When studying fluid flows, it is often safe to assume that material density is constant or almost constant: for this reason, the concept of incompressible fluid flow is introduced, and *Incompressible Navier-Stokes* application is FEMLAB™ model that was chosen in addition to *Conductive Media DC* and *General Heat Transfer* to perform the electro-fluidic-thermal simulations.

4.5.1 – Thermal-fluidic coupling.

In the case of previously described electro-thermal model, the bi-directional coupling was carried out by defining a temperature-dependent electrical conductivity $\sigma(T)$ (see eq. 10, electrical-to-thermal coupling) and a voltage-dependent heat source Q(V) (see eq. 15, thermal-to-electrical coupling).

Similar relationships have to be found in order to bi-directionally couple Navier-Stokes equations and Fourier equation.

Thermal-to-fluidic coupling is quite immediate, since velocity field u (unknown quantity of Navier-Stokes problem) appears in convective term of Fourier heat equation, while fluidic-to-thermal coupling is expressed by the *Boussinesq approximation* [4].

The latter is a way to treat some simple cases of buoyant flows without having to use a compressible formulation of the Navier-Stokes equations, assuming that variations in density have no effect on the flow field except that they give rise to buoyant forces: in particular, the buoyancy term can be identified with a volumetric force F = ρ·β·g·(T-RT), where ρ = fluid density, g = 9.8[m/sec^2] = gravity acceleration, T = fluid temperature, RT = room temperature, β = fluid thermal compressibility = $-\frac{1}{\rho}\cdot\left.\frac{\partial\rho}{\partial T}\right|_{T=RT} \cong \frac{1}{RT}$.

Boussinesq approximation, hence, represents a formulation (valid only for systems of very small dimensions, as in our case) which defines a temperature-dependent volumetric force (i.e. a pressure) along the normal direction to fluid flow.

4.5.2 – Simulation results for ULP-MOX sensor.

The first structure taken into account is the one illustrated in Fig. 3.13 (the same used for the previously described transient analysis) and equipped with a rectangular pyrex micro-chamber, as presented in the following figure:

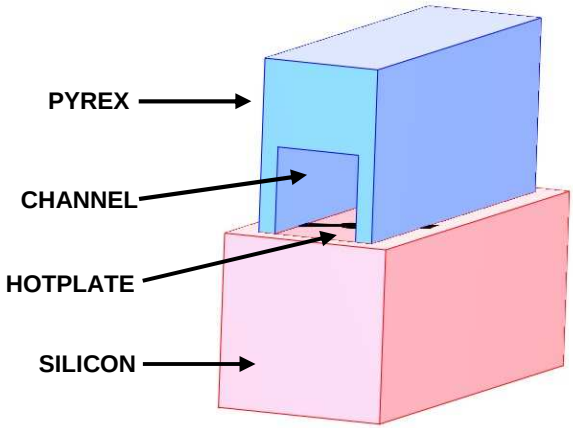

Fig. 4.19 – Simulated MINIMAL structure with integrated micro-chamber.

Height and length of pyrex chamber are 500µm and 1500µm respectively (such as the silicon chip) while its internal channel has inlet and outlet cross section of 250x250 µm^2. To investigate flow behaviour inside the chamber, i.e. to discriminate between laminar or turbulent, Reynolds number has to be evaluated: the latter is defined as

$$\mathrm{Re} = \frac{\rho \cdot u \cdot L}{\mu} \qquad (28)$$

being ρ fluid density, u fluid average velocity at the inlet, L channel internal dimension and μ fluid dynamic viscosity.
In particular, it is generally agreed that:

- for Re ≤ 2000, a fluid must be treated as laminar (stationary, moving parallel to the channel direction as a bi-dimensional flow)
- for 2000 < Re < 10000, a fluid is in a transition regime (it has the tendency to lose its stationary behaviour, forming small undulations)
- for Re ≥ 10000, a fluid must be treated as turbulent (characterized by a three-dimensional, non stationary and chaotic flow).

Since the considered fluid is air, the condition of non laminar flow is reached when $\frac{\rho \cdot u \cdot L}{\mu} > 2000 \Rightarrow \frac{1.23 \cdot u \cdot 250 \cdot 10^{-6}}{1.79 \cdot 10^{-5}} > 2000 \Rightarrow u > \frac{2000 \cdot 1.79 \cdot 10^{-5}}{1.23 \cdot 250 \cdot 10^{-6}} \Rightarrow$ **u > 116 [m/sec]**, which is an unrealistic working operation: air flow inside pyrex micro-chamber must be therefore considered as laminar.
In order to investigate flow influence on ULP hotplate, and in particular on power dissipation, five different working conditions were studied: I) a reference case represented by absence of flux and considering only conductive contribution to heat transfer, II) an analogous case, but taking into account also natural convection, III) a laminar air flux with volumetric flow rate of 0.5sccm (typical of fast-GC), IV) a volumetric flow rate of 2sccm and finally V) an extremely high volumetric flow rate of 10sccm.
As far as coupled model conditions are concerned, electrical and thermal features for these simulations are the same already employed in the electro-thermal model, except for the boundary related to pyrex chamber outlet, where the condition of *convective flux* was imposed, while the fluidic part is structured such that the only subdomains involved are the regions where flow is present (channel and pit underneath membrane) where a vertical buoyancy force (F = ρ·β·g·(T-RT), see previous section) was considered, and

boundary conditions are everywhere set as *no slip*, except for channel inlet where a flow velocity vin = Q/Ain was imposed (Q[cm^3/min] = volumetric flow rate, Ain[m^2] = channel cross section) and for channel outlet, set at ambient pressure.

Different temperature values as a function of heater power consumption have been obtained from 3-D simulations and logged in the following graph, to compare the different working conditions (mesh parameters: number of tetrahedral elements = 43415, triangular boundary elements = 8051, edge elements = 1674, vertex elements = 429, number of degrees of freedom = 179557, relative tolerance = 10^{-6}):

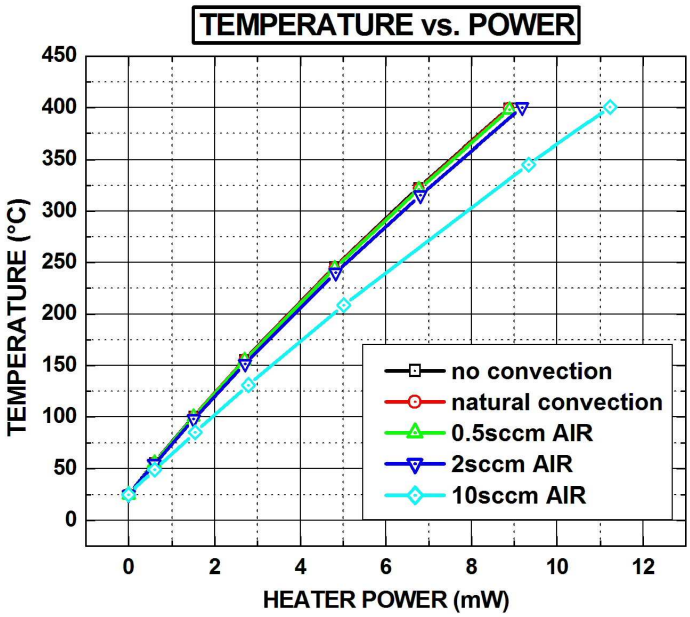

Fig. 4.20 – Simulated "Temperature vs. Power" curves for different air flow rates.

Results analysis confirmed the general assumption to neglect natural convection effects on power consumption (dominated by conduction, in absence of flux) and showed the increasing contribution of air fluxes on dissipated power (minimal for flow rate = 0.5sccm, appreciable for flow rate = 2sccm, remarkable for flow rate = 10sccm).

Next figure shows air flow inside the micro-chamber in case of natural convection (streamlines characterized by two main counter rotating vortices) and in case of volumetric flow rate = 0.5sccm (typical streamlines of a laminar fluid).

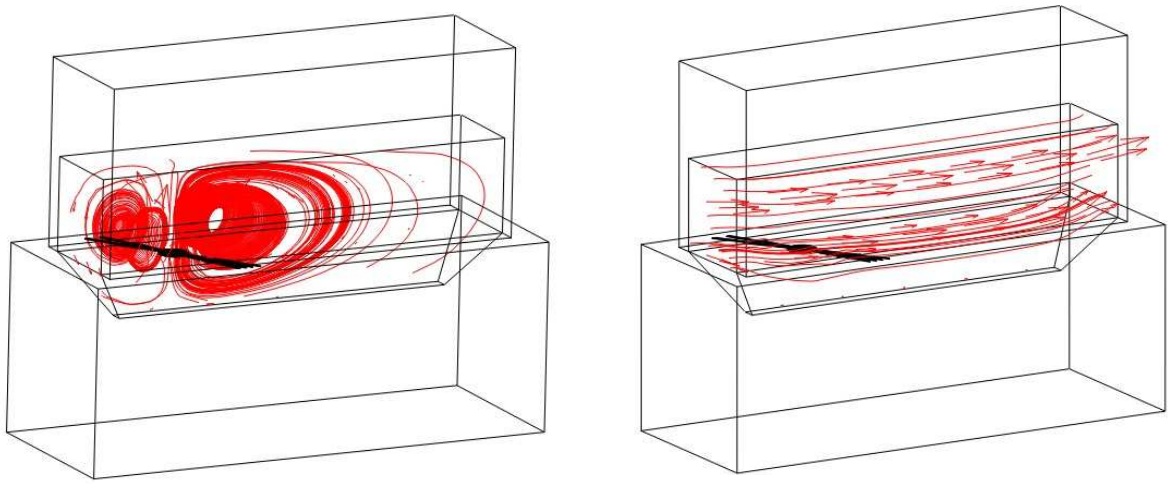

Fig. 4.21 – Streamlines inside the micro-chamber: natural convection (left) and volumetric flow rate = 0.5sccm (right) .

To have a comparison between simulations and experimental results, a second structure has been taken into account, formed by two symmetrical meandered platinum resistors suspended over a dielectric membrane (as illustrated in Fig. 4.22-a); the chip containing an array of three devices was subsequently enclosed with the pyrex micro-chamber, as shown in Fig. 4.22-b.

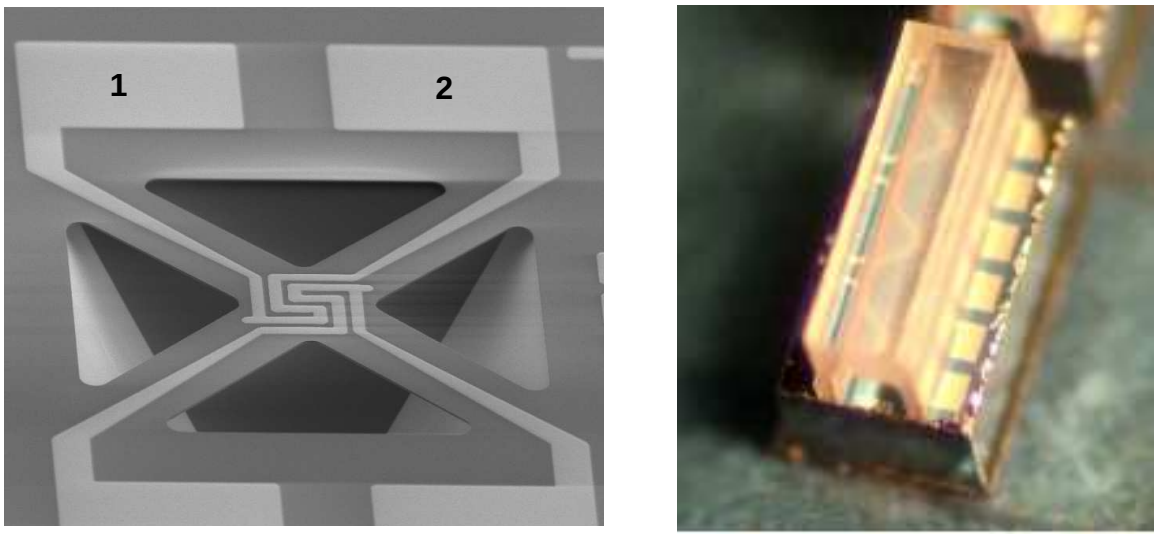

(a) *(b)*

Fig. 4.22 – SEM micrograph of the measured and simulated structure (a) and chip enclosure with pyrex micro-chamber (b).

Two 15cm-long fused silica capillaries, with an internal diameter of 100µm, have been glued along their edges at the extremities of the groove, forming gas flow inlet and outlet: in particular, different gas flow rates (obtained by regulating a proper relief valve) were considered during electrical measurements, performed by connecting heater pads (labelled with 1 and 2 in Fig. 4.22-a) to a 2410 Keithley source-meter.

All the measurements have been done through a current sweep (from 0.2mA to 12.6mA, with a step of 0.4mA) on the device and measuring the corresponding voltage drop, resistance value (linked to temperature) and dissipated power.

Unfortunately, the absence of an integrated platinum temperature sensor in the structure did not allow a precise measurement of device temperature, but only its estimation through heater resistance (on the basis of the same principle described in chapter 3 when the concept of *equivalent TCR* was introduced).

Experimental results were reported on the following graph for the same air volumetric flow rates (no flux, 0.5sccm, 2sccm, 10sccm) previously introduced and all the measurements confirmed that, at fixed power, heater resistance (and temperature, by consequence) decreased for increasing air flow, due to an increasing contribution of convection.

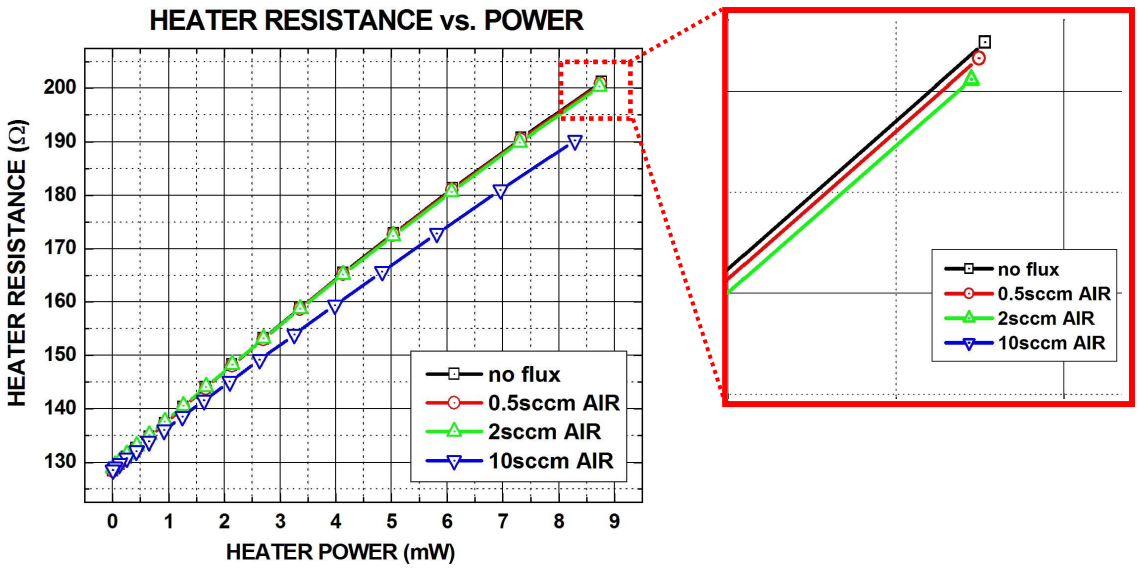

Fig. 4.23 – Measured Temperature vs. Power curves for different air flow rates.

An analogous trend was found in simulation results, as shown in the following figure:

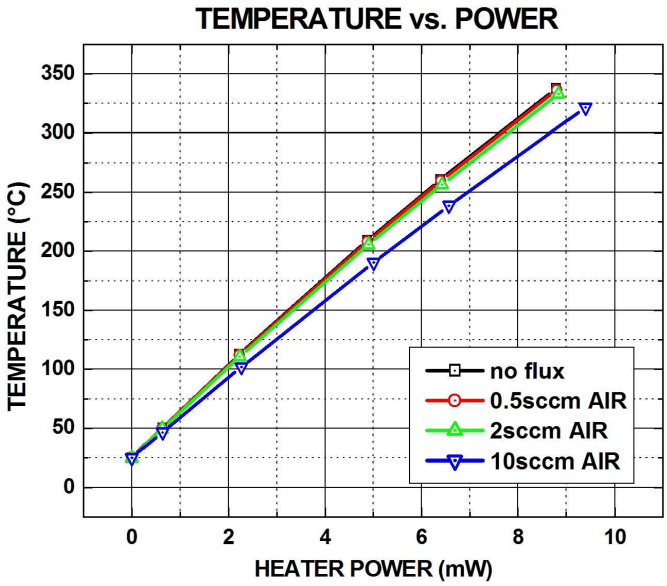

Fig. 4.24 – Simulated Temperature vs. Power curves for different air flow rates.

Next figure show the impact of air flow on the temperature field in correspondence of a normal plane to structure surface: the three different air volumetric flow rates of 0.5, 2 and 10sccm where considered

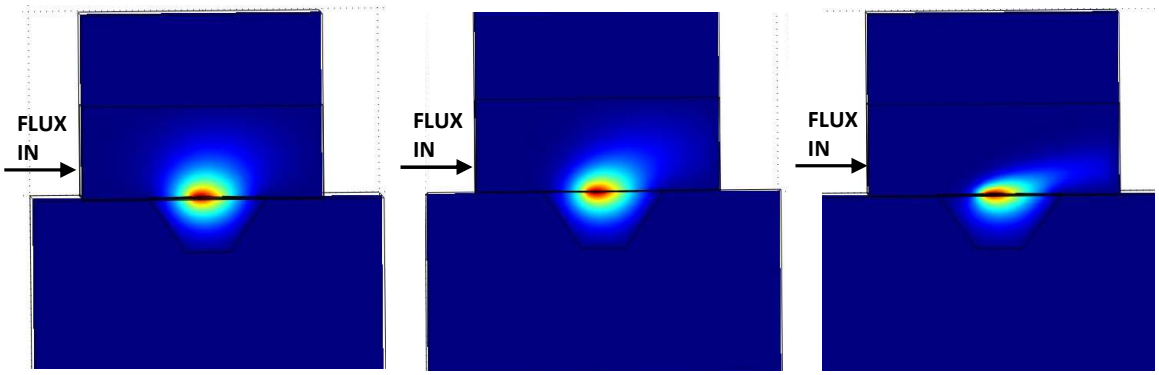

Fig. 4.25 – Simulated temperature distribution over a normal plane to device surface: air volumetric flow rate = 0.5sccm (left), 2sccm (centre) and 10sccm (right).

It can be easily disclosed that temperature field is highly modified by increasing flow rate, evolving from a condition of quasi-symmetry (0.5sccm) to a very unbalanced one (10sccm).

4.6 – SIMULATION RESULTS FOR TCD.

As in case of the structure presented in Fig. 4.22, the micro-fabricated TCD described in chapter 3 is not equipped with an integrated temperature sensor, and for this reason, unless using the approximated model of equivalent TCR, the capability to perform simulations by means of a validated method represents a powerful tool for evaluating TCD characteristics, especially power consumption as a function of temperature (since TCD working temperature is similar to MOX sensor, about 400°C).

For the sake of simplicity, and to reduce computational effort, only one of the four resistors forming the Wheatstone bridge configuration of TCD was considered in simulations (see Fig. 3.25-b).

As already mentioned in chapter 3, process flow for micro-TCD fabrication is similar to the one exploited for MOX sensor, but material layer thicknesses and depth of etch pit underneath dielectric membrane are fairly different, as reported in the following table:

LAYER		THICKNESS
DIELECTRIC MEMBRANE	THERMAL SiO_2	250 nm
	LPCVD Si_3N_4	130 nm
	LOW THERMAL SiO_2 (LTO)	500 nm
PLATINUM		250 nm
DEPTH OF D-RIE ETCHED SILICON		60 µm

Tab. 10 – Measured thicknesses of TCD material layers.

Also electrical properties of platinum have been measured, with procedures similar to those adopted for MOX sensors and described in section 4.3.2, and results have been as follows:

SQUARE RESISTANCE @ 298K	0.75 [Ω]
TCR	0.0033 [1/K]
RESISTIVITY @298K	$3 \cdot 10^6$ [Ω/m]

Tab. 11 – Measured electrical properties of TCD platinum.

These values have been employed in the three-dimensional fluidic-electro-thermal model to estimate static power consumption of the single resistor as a function of temperature, considering two different carrier gases (air and helium) at a volumetric flow rate of 0.5sccm: by this purpose, temperature-dependent helium thermal conductivity, heat capacity and density were considered, acquiring the corresponding relationships from FEMLAB™ material database.

Performed simulations were characterized by a noticeable computational effort, given the major complexity of TCD structure with respect to MOX sensor: discretization mesh was in fact formed by a number of tetrahedral elements = 76448, triangular boundary elements = 16198, edge elements = 3926, vertex elements = 918, number of degrees of freedom = 350007.

Simulations results are presented in figure 4.26: reported temperature values are the maximum punctual values provided by simulations in correspondence of specific dissipated powers.

Results point out that, at fixed temperature, resistor power consumption for helium carrier gas is about five times higher with respect to air carrier gas: this fact confirms experimental results already shown in chapter 3 (section 3.5.3, Fig. 3.35, air replaced by nitrogen, which is practically identical).

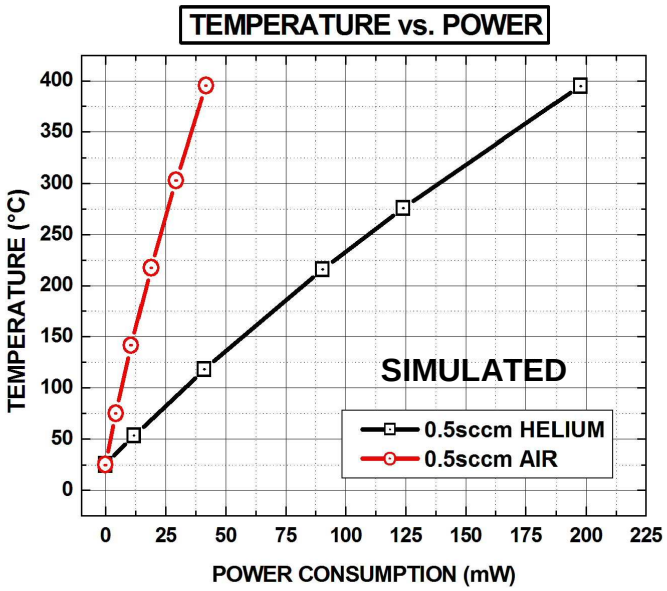

Fig. 4.26 – Simulated Temperature vs. Power curves at 0.5sccm flow rates: AIR (red line) and HELIUM (black line).

In particular, single resistor power consumption in air and in helium at 400°C is 42mW and 200mW respectively: such values are quite similar to those reported in figure 3.35 and obtained through the introduction of equivalent TCR-based model for the single resistor.

For this reason, it is reasonable to assume that dissipated power by the entire TCD device (Wheatstone bridge formed by four resistors) in air and in helium at 400°C is about 170mW and 800mW respectively.

As far as temperature distribution over resistor surface is concerned, next figure shows simulation result in helium for power consumption = 200mW, and also temperature variations along the horizontal black dotted mid-line.

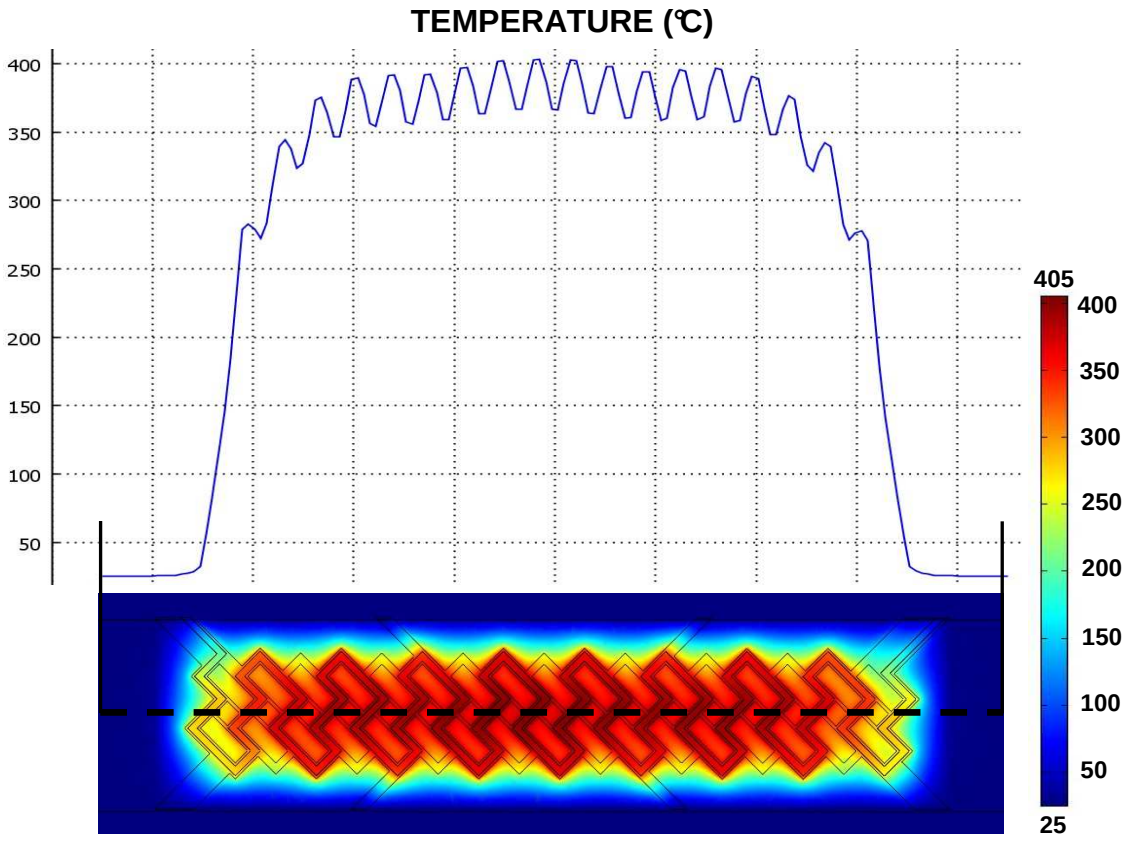

Fig. 4.27 – Simulated temperature distribution over resistor surface and along a horizontal mid-line (carrier = Helium, power consumption = 200mW).

Even if in the case of TCD the constraint of temperature uniformity is not as important as it was for MOX sensors (because of the necessity to maintain the whole sensitive hot

spot at the same temperature), a large device region characterized by a quite uniform temperature distribution can be disclosed (a similar condition was illustrated in Fig. 3.36).

4.6.1 – TCD resistor transient analysis.

In section 4.4, the transient analysis of a specific ULP-MOX sensor configuration was performed through electro-thermal simulations, and a cooling transient thermal time constant of 1.32 ms was evaluated (very close to the value of 1.47ms obtained from experimental measurements).

Analogous simulations have been performed on the single resistor of the Wheatstone bridge-configured TCD presented in chapter 3 (Fig. 3.25-b), in presence of helium as gas carrier (on the contrary of air, considered for ULP transient analysis) inside the micro-chamber.

Density and heat capacity values of the material layers involved are the same presented in Tab. 9 for the ULP-MOX sensor, while density and heat capacity values for helium introduced in the transient model have been taken, as usual, from FEMLAB™ material database and were found to be virtually constant in temperature ranges of interest [25 ÷ 400°C]: ρ_{HELIUM} = 0.2[Kg/m^3] and Cp_{HELIUM} = 5197[J/Kg·K].

As in the case of the ULP-MOX sensor analysis, a preliminary steady-state simulation of the device at 400°C was executed, the achieved result was stored and considered as the starting point of the subsequent cooling transient simulation, obtained by imposing a zero-voltage on the resistor pads (mesh parameters: number of tetrahedral elements = 79959, triangular boundary elements = 17271, edge elements = 4361, vertex elements = 918, number of degrees of freedom = 117399, relative tolerance = 10^{-6}).

Simulation result for the TCD resistor is presented in Fig. 4.28, where an extremely low thermal time constant value of only 0.16ms is reported: the remarkable difference with the theoretical value found for ULP-MOX sensor (1.32ms) is explained by considering the formula of thermal time constant τ for as general structure:

$$\tau = \frac{C_P \cdot m}{\lambda \cdot S} \qquad (29)$$

where C_P is the heat capacity, m is the mass, λ is the global coefficient of heat exchange (equal to thermal conductivity per length unit) and S is the heat-dissipating surface.

Given the geometrical dimensions of the problem, the materials accountable for heat dissipation are basically air in the case of ULP-MOX analysis and helium in the case of TCD-resistor analysis, so the thermal time constants will be proportional to $\frac{C_{PAir} \cdot m_{Air}}{\lambda_{Air} \cdot S_{ULP}}$ and $\frac{C_{PHelium} \cdot m_{Helium}}{\lambda_{Helium} \cdot S_{TCD}}$ respectively.

Being $S_{TCD} \approx 1.5 * S_{ULP}$, $C_{PHelium} \approx 5 * C_{Pair}$, $\lambda_{Air} \approx 5 * \lambda_{Helium}$ (since air thermal conductivity is approximately five times higher than helium thermal conductivity), the $\tau_{Device\_Air}/\tau_{Device\_Helium}$ ratio will be proportional to $1.5*(m_{Air}/m_{Helium})$or, in other terms, to $1.5*(\rho_{Air}/\rho_{Helium})$, where ρ is the density.

Since ρ_{Air} (1.205[Kg/m^3] at RT) is about six times higher than ρ_{Helium} (0.2[Kg/m^3] at RT), as a direct consequence the thermal time constant of the ULP-MOX in air will be about 9 times higher than the one of the TCD resistor in helium, and simulations matched quite well with this assumption (τ_{Device_Air} = 1.32ms, τ_{Device_Helium} = 0.16ms).

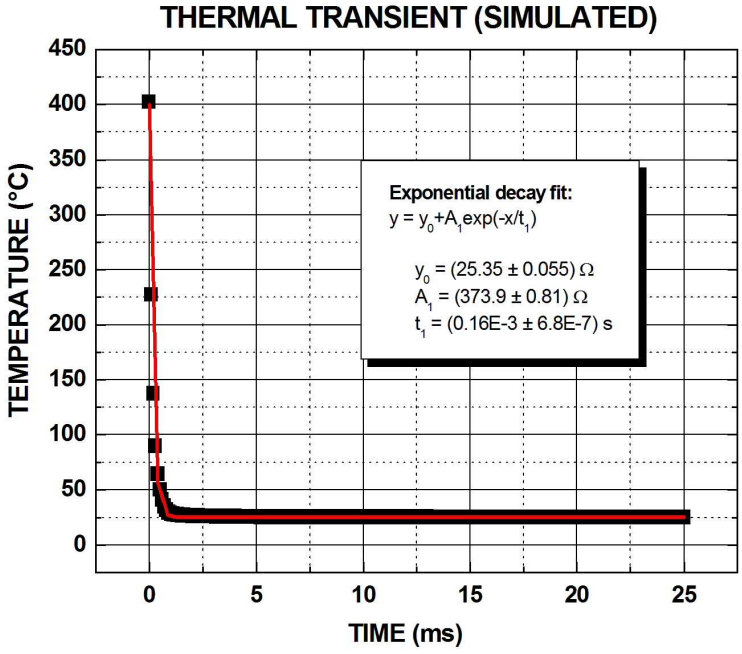

Fig. 4.28 – Simulated cooling transient for the TCD resistor.

REFERENCES

[1] Von Arx M., Paul O., Baltes H.: "Process-Dependent Thin-Film Thermal Conductivities for Thermal CMOS MEMS", *Journal of Microelectromechanical Systems*, volume 9, issue 1, pp. 136 – 145 (*2000*).

[2] Centurioni E.: "Generalized matrix method for calculation of internal light energy flux in mixed coherent and incoherent multilayers", Applied Optics, Volume 44, issue 35, pp. 7532 – 7539 (2005).

[3] Graf M., Jurischka R., Barrettino D., Hierlemann A.: "3D nonlinear modeling of microhotplates in CMOS technology for use as metal-oxide-based gas sensors", *Journal of Micromechanics and Microengeneering*, volume 15, issue 1, pp. 190–200 (2005).

[4] Gray D.D., Giorgini A.: "Validity of Boussinesq Approximation for liquid and gases", *International Journal of Heat and Mass Transfer*, volume 19, issue 5, pp. 545 – 551 (1976).

CHAPTER 5

CONCLUSIONS

Design parameters, process flows, electro-thermal-fluidic simulations and experimental characterizations of Micro-Electro-Mechanical-Systems (MEMS) suited for gas-chromatographic (GC) applications have been presented and thoroughly described in this thesis, whose topic belongs to the research activities the Institute for Microelectronics and Microsystems (IMM)-Bologna is involved since several years, i.e. the development of micro-systems for chemical analysis, based on silicon micro-machining techniques and able to perform analysis of complex gaseous mixtures, especially in the field of environmental monitoring.

The issue of air quality, in fact, is subjected to a rapidly increasing interest, mainly for its consequences on human healthcare and safety, and in this scenario the gas-chromatographic techniques can be easily adapted to the separation and analysis of certain potentially harmful compounds mixed with the air that we breathe.

In this regard, as reported in chapter 2, attention has been focused on the development of micro-fabricated devices to be employed in a mini-GC system, developed at IMM Bologna, for the analysis of aromatic Volatile Organic Compounds (VOC) like Benzene, Toluene, Ethyl-benzene and Xylene (BTEX), i.e. chemical compounds which can significantly affect environment and human health because of their demonstrated carcinogenicity (benzene) or toxicity (toluene, xylene) even at parts per billion (ppb) concentrations.

The silicon micro-machined devices the main building blocks of a GC system for BTEX detection are made up of have been presented, specifically a pre-concentration unit filled with an innovative stationary phase (cavitands), two different typologies of double spiral-shaped packed separation columns (50cm-long and 100cm-long) and a very sensitive Metal OXide (MOX) gas sensor based on a chemo-resistive detection principle.

This represents a first significant aspect of the developed research activity, i.e. the innovative combining, in a gas-chromatographic architecture, of silicon micro-fluidic devices (pre-concentrator and separation column) with metal oxide-based sensors.

Design layouts of the single micro-devices have been described, together with the process flows employed for their fabrication and the principal results of electrical and functional characterization; successively, the packaged mini-GC system has been presented, providing schematics of the electrical and fluidic interconnections between the single blocks, and details on the operating sequence.

Finally, the most significant results achieved through its laboratory functional characterization have been reported, highlighting the excellent response to the compounds of interest even at sub-ppb concentrations.

Not requiring any auxiliary cylinder (neither carrier gas nor calibration sources), the developed mini-GC system is intrinsically portable, easy to deploy and suitable for in-field use. In this regard, the mini-GC system performances have been tested in-field analysis carried out in a station of the Bologna (ARPA) air monitoring network. The responses towards benzene have been compared with those provided by a commercial GC system, showing a very good agreement.

Aiming at decreasing the times of analysis, at overcoming the possible limitations of the micro-devices presented in chapter 2 (specifically targeted to BTEX analysis and not suitable to address other compounds of interest) and at improving their performances (decreasing power consumption, dimensions and costs) even further, the development of more advanced prototypes of micro-fabricated devices specifically suited for FAST-GC have been presented in chapter 3, together with the technological processes for their fabrication and the solution for electric and fluidic packaging.

The Ultra-Low-Power (ULP)-MOX sensor was designed in order to optimize the MOX sensor employed in the previously described mini-GC system, ensuring a decrease of power consumption at working temperature and a significant reduction of geometrical dimensions, suitable for its further integration in a more complex micro-fluidic MEMS.

In particular, the experimentally demonstrated very high sensitivity of ULP-MOX sensors to VOCs, coupled with the extremely low power consumption, makes the developed

ULP-MOX sensor the most performing metal oxide sensor reported up to now in literature.

The capillary separation column (designed in two different configurations, one with channels presenting a 100µm-diameter circular cross-section and the other with channels presenting a 30x300µm^2 rectangular cross-section) was designed to satisfy the geometrical (column length, channel diameter) and physical (gas volumetric flow-rate, time of analysis) constraints imposed by implementing a FAST-GC technique.

Preliminary test results proved that the developed silicon capillary columns are capable of performances comparable to those of the best fused silica capillary columns, while presenting a lower and more compact size that results in several advantages, such as a more effective control of the operating temperature.

The Thermal Conductivity Detector (TCD) was designed in order to allow the analysis of a wider range of compounds with respect to MOX sensors, due to TCD “universality” (on the basis of its detection principle) and capability of responding to all the components of a gas sample.

The procedure for TCD and ULP-MOX encapsulation in a ultra-low-volume pyrex micro-chamber (to reduce dead volumes as much as possible, according to FAST-GC requirements) was described step by step, together with the experimental characterization performed on the two detectors aiming at investigating their reaction to different gases (nitrogen and helium) entering the micro-chamber.

Finally, in chapter 4, the development and the validation of a coupled electro-thermal Finite Element Model (successively implemented with the micro-fluidic part) suited for both steady-state and transient analysis of the micro-devices has been described, including the theoretical and mathematical formulations.

Measurement procedures carried out for a precise evaluation of the geometrical, electrical, thermal and optical properties of the material layers involved in the fabrication of the different devices have been thoroughly described, together with the model validation campaign, performed by comparing the simulations results with the experimental results obtained from the electro-thermal characterization of three different ULP test structures.

As already mentioned, the model was subsequently implemented with a fluidic part governed by Navier-Stokes equations, to investigate devices behaviour in presence of a gas flowing with certain volumetric flow rates and to compare simulations results with the experimental ones reported in chapter 3.

As far as the future perspectives are concerned, and the possible development of the research activity described in this thesis, the attention is doubtless focused on the topic of FAST-GC. On the lines of the described mini-GC system, in fact, the medium-long term target is the design and the fabrication of a totally micro-fabricated GC-system suited for FAST-GC applications, whose interconnections between blocks are formed by fused silica capillaries characterized by a micro-metric diameter.

The capillary columns described in this thesis are the first prototypes of the separation block of the system, just like the ULP-MOX and the micro-TCD are the first prototypes of the detection block. As far as the injection block is concerned, the possibility to develop a totally micro-machined silicon injector has been thoroughly investigated and the layout design of an innovative micro-fabricated injection system to be employed in the future micro-GC system is ongoing.